**The Vancouver Geotechnical Society**
**A Local Section of**

**The Canadian Geotechnical Society**

**La Société canadienne de géotechnique**

# 29th Symposium of the Vancouver Geotechnical Society

# Geotechnical Engineering in Infrastructure

## Friday, September 15, 2023

**Pinnacle Hotel Vancouver Harbourfront**
**1133 West Hastings Street, Vancouver, B.C.**

| | |
|---|---|
| 07:00 - 08:00 | **Registration** |
| 08:00 - 08:05 | **Opening Remarks** |
| 08:05 - 08:30 | Juan-Carlos Carvajal - *Seismic Embankment-Abutment-Structure Interaction of Integral Abutment Bridges.* |
| 08:35 - 09:00 | Karim Karimzadegan - *Geotechnical Design Challenges for Temporary Excavation Support at the Arbutus Station and Double Crossover for the Broadway Subway Project in Vancouver, BC* |
| 09:05 - 09:30 | David J. Tara - *What We Know About High-Strain Dynamic Testing Steel Pipe Piles with Concrete Plugs* |
| 09:30 - 10:00 | **Coffee Break** |
| 10:00 - 10:25 | Marc Bosse - *Geotechnical evidence for the 11 kYa glacial Lake Fraser outburst flood between Abbotsford and Pitt Meadows* |
| 10:30 - 11:30 | **Keynote Lecture by Thaleia Travasarou** - *Geotechnical Best Practices for Risk-Informed Decision Making in Earthquake Infrastructure Design* |
| 11:30 - 13:00 | **Lunch** |
| 13:00 - 13:25 | Omar Rodríguez Barragán - *Top-Down Excavation System, An Integral Solution for Challenging Deep Excavation Projects With Complex Surroundings and Difficult Geotechnical Conditions* |
| 13:30 - 14:30 | **Keynote Lecture by Brian L.J. Mylleville** - *Repair of the Sumas River Dike Breach: A Case History* |
| 14:30 - 14:40 | 2023 VGS Award |
| 14:40 - 15:05 | Aran Thurairajah - *New Iona Island Wastewater Treatment Plant and Foundation Approach* |
| 15:05 - 15:35 | **Coffee Break** |
| 15:35 - 16:00 | Lalinda Weerasekara - *Limitations in Existing Methods for Analyzing MSE Walls Reinforced with Steel Strips* |
| 16:05 - 16:30 | Viet (Victor) Tran - *3D Seismic Numerical Modeling of Infrastructure on Liquefiable Soils - Soil-Structure Interaction and Soil-Cement Grid Modeling* |
| 16:30 - 16:45 | **Closing Remarks** |
| 16:45 - 18:00 | **Social Hour** |

# Geotechnical Design Challenges for Temporary Excavation Support at the Arbutus Station and Double Crossover for the Broadway Subway Project in Vancouver, BC

Karim Karimzadegan, M.A.Sc., P.Eng.
Principal Engineer[1].

Takahiro (Hiro) Shozen, M.A.Sc., P. Eng.
Senior Geotechnical Engineer[1].

Haroon Bux, P. Eng.
Geotechnical Engineer[1].

Robert Ng, P. Eng.
Senior Geotechnical Engineer[1].

**ABSTRACT** The Broadway Subway Project in Vancouver, BC is a 5.7 km extension of the Skytrain Millennium Line and will have six stations located along a route extending from the VCC-Clark Station to the intersection of Broadway and Arbutus Street. This paper will focus on geotechnical design challenges for temporary excavation support at the Arbutus Station and Double Crossover site which forms the western-most station with a footprint that extends the length of two city blocks. Excavation depths up to 20 m are required and the final design consists of four different shoring systems to accommodate the various design constraints which include non-encroachment areas. Excavation support is to be provided to adjacent buildings, utilities, a traffic deck, and Metro Vancouver's Capilano No. 4 and No. 5 water mains. The shoring system will also accommodate the tail track tunnels and an approximately 14.5 m wide by 21 m long open area to allow for removal of the tunnel boring machines using a large crane that will be seated immediately adjacent to the crest of the excavation. A collaborative effort and iterative design process between all members of the project team was required to complete this complex shoring design.

## Introduction

The Broadway Subway Project is located in Vancouver, BC and is an extension of the existing Skytrain Millennium Line that is part of the local rapid transit system. The route will extend from the VCC-Clark Station to the intersection of Broadway and Arbutus Street and include six new station locations (Fig. 1). This paper focuses on the geotechnical design challenges for temporary excavation support at the Arbutus Station and Double Crossover site which forms the western-most station. The footprint of this station extends the length of two city blocks and is bounded by Cypress Street to the east, Arbutus Street to the west, and private properties to the north and south of Broadway as shown in Fig. 2. The Arbutus Station building occupies the western portion of this project site between Arbutus Street and Maple Street. The Headhouse providing access from ground surface to the station level is located at the west end of the structure along the east side of Arbutus Street (Fig. 2). The Double Crossover, which facilitates trains to switch tracks, occupies the eastern portion of the project site from Maple Street to Cypress Street.

Excavation depths of up to approximately 20 m are required with vertical excavation slopes supporting adjacent buildings and infrastructure. The buildings located adjacent to the north and south sides of Broadway vary from at-grade, single level commercial buildings to multilevel residential and commercial buildings with basement levels. Many existing underground utilities that include storm, sanitary, water, telecommunications, gas, and electrical lines are located below the road and sidewalk areas of Broadway. Where practicable, relocation of existing above and below grade utilities would be carried out to facilitate the excavation and construction works. Significant existing underground infrastructure that require support includes two Metro Vancouver large diameter water mains called Capilano Main No.4 (CMN4) and No.5 (CMN5) and a large concrete BC Hydro duct bank. Design and implementation of excavation shoring is not permitted to disrupt these utilities and infrastructure. Furthermore, permission for excavation shoring elements to encroach into adjacent properties varies across the project site with minimum required offset distances to reduce potential conflicts and damage.

[1] Horizon Engineering Inc. (A RAM Company), North Vancouver, BC.

**Fig. 1.** Broadway Subway Project and new station locations.

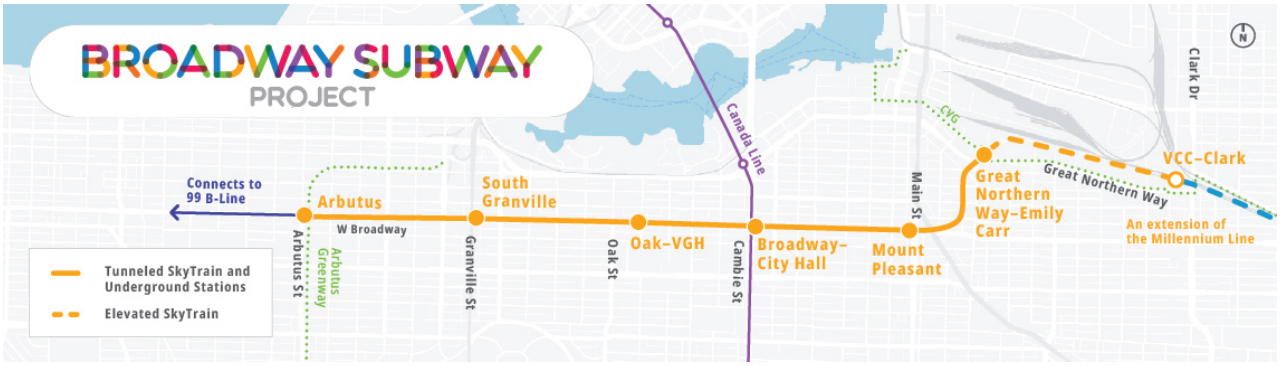


**Fig. 2.** Arbutus Station and Double Crossover Plan.


# Subsurface Conditions

## Surficial and Bedrock Geology

Based on published surficial geology information from the Geological Survey of Canada (Armstrong 1979), the site is underlain by Vashon Drift and Capilano Sediments. These surficial geology deposits generally consist of glacial drift that include lodgement till, lenses and interbeds of glaciofluvial sand to gravel, and lenses and interbeds of glaciolacustrine laminated stony silt. Bedrock is estimated to be at depth of 10 m or less below the ground surface. Subsurface investigations were carried out to characterize the local geology and groundwater conditions (Golder 2019a, Golder 2019b, and EXP 2021). An interpreted east-west geological section along the project site is shown in Fig. 3.

The general soil stratigraphy at the project site consists of fill to depths of about 0.5 to 2.8 m and underlain by surficial soil types typically comprising moist silty clay, clayey to organic silt, and clayey sand and silty sand soil types. These surficial soil types were generally present to depths of about 2.5 to 4.5 m; however, this soil stratum was encountered to a depth of about 6 m at the eastern end of the project site which coincides with a buried creek channel at Cypress Street. The fill and surficial soil are underlain by a stoney / stoneless silt stratum that generally consisted of moist to wet, non-plastic to low plastic silt, clay, and sandy silt soil types to depths ranging from approximately 9 to 12 m but with variable thickness across the site. The consistency / compactness of the stoney / stoneless silt stratum varied from very stiff to hard / dense to very dense. Glacial deposits underlie the fill, surficial soil, and silt stratum.

The glacial deposits are subdivided into Glacial Drift and underlain by Glacial Till which in turn is underlain by Bedrock. Glacial Drift generally consists of dry to moist, silt, sand, clay, and gravel soil types that are present to depths of about 10 to 13 m and with stiff to hard / compact to very dense consistency / compactness. Glacial Till generally consists of moist to dry, clay, silt, sand to gravelly soil types that include cobbles, boulders, and occasional cemented soil fragments. The Glacial Till was found to have consistency / compactness of hard / very dense and present to depths of about 18 to 20 m. Bedrock within the depths of interest generally consisted of extremely weak to weak sandstone with interlayered mudstone and siltstone that are extremely weak to very weak. The sandstone may include comparatively small siltstone clasts and

**Fig. 3.** Geological section along Broadway Street at Arbutus Station and Double Crossover site.

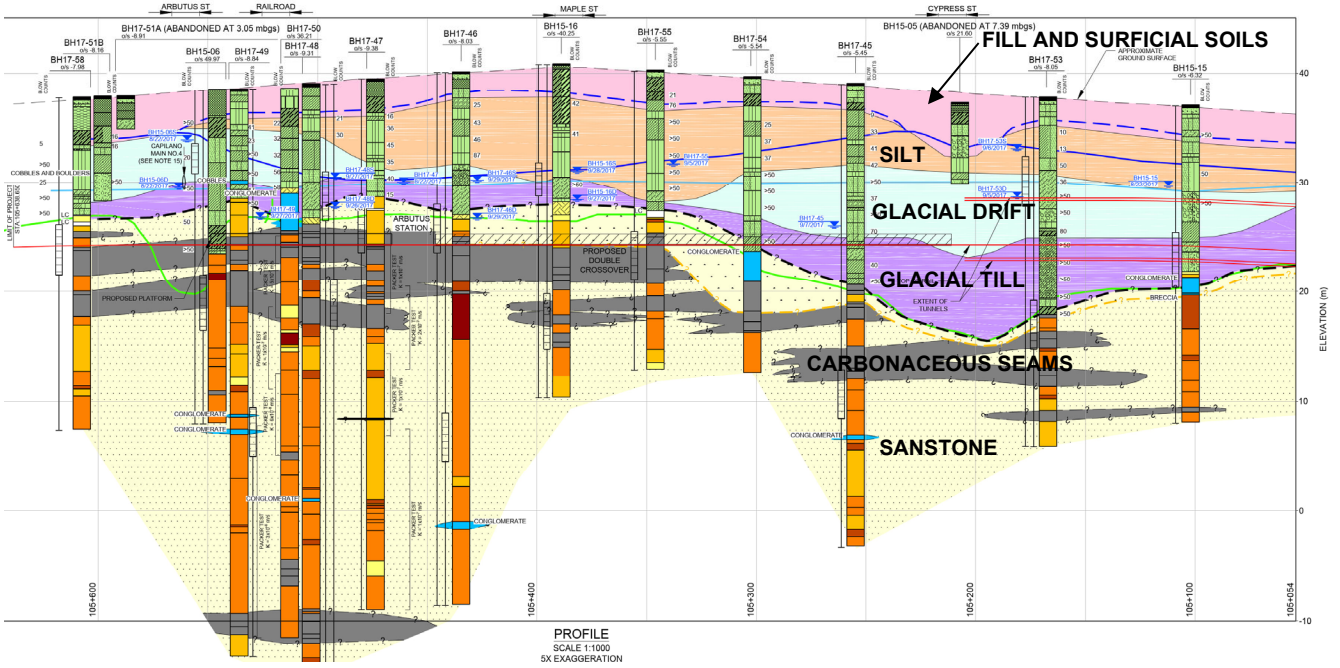


carbonaceous fragments in addition to having laminations, sealed joints, gouge infill, and brecciated zones. Conglomerate may also be present at discrete portions of the bedrock. The uniaxial compressive strength of the bedrock is estimated to range from about 0.25 to 5.0 MPa.

## Groundwater

Perched groundwater may be encountered in the fill and surficial soil types and where the excavation cuts into granular backfill of utility trenches and surrounding buildings. The groundwater table at areas located in the vicinity of Arbutus Street was interpreted to vary from approximately 3.5 to 4 m below site grades and generally correlated with the top of the glacial drift. From about Arbutus Street to Maple Street, the groundwater table was interpreted to be at approximately 9 m below site grades and generally correlated with the top of the glacial till. From about Maple Street to Cypress Street, the groundwater table was interpreted to gradually rise to shallower depths of about 4 to 5 m below site grades. Preferential groundwater flow may be encountered in zones with greater hydraulic conductivity such as sand seams. Groundwater may also be expected from open fractures, joints, and other discontinuities in the bedrock. It is expected that groundwater levels and seepage rates would fluctuate seasonally. No artesian groundwater conditions were encountered at the test holes advanced in the general vicinity of the project site.

Design excavation depths are expected to terminate in bedrock with an exception at the eastern approximate 100 m of the excavation footprint where glacial deposits are expected and bedrock is at greater depths.

# Design Challenges

The geotechnical design challenges for excavation shoring at the project site can be divided into 6 zones as conceptually shown on Fig 4. Each zone has site-specific design considerations and constraints that the shoring strategy is required to address. The shoring system for each of these zones is also required to be optimized with respect to design and construction to provide cost-effective solutions in addition to preferentially utilizing materials that have been secured for other components of the overall Broadway Subway project. Design of the shoring systems are also expected to manage ground deformations to tolerable limits as determined by structural assessments for the adjacent buildings and underground infrastructure.

In conjunction with the excavation shoring, pairs of piles will be installed along the north and south sides of Broadway as support columns for the traffic decks that will provide public access over the construction site. These traffic piles are considered free standing from the shoring system; however, where the shoring system consists of secant piles or braced soldier piles, the traffic deck will be supported on these piles that are part of the shoring system. Furthermore, components of the shoring system, such as tie-back anchors and shotcrete infill panels, will be required to accommodate the locations of the traffic piles.

Any shoring elements, such as solider piles, foundation piles for the traffic deck, shotcrete walls, and tie-back anchors, that will permanently remain in the ground will be required to be demolished and backfilled or fully grouted to

**Fig. 4.** Design challenge zones for Arbutus Station and Double Crossover

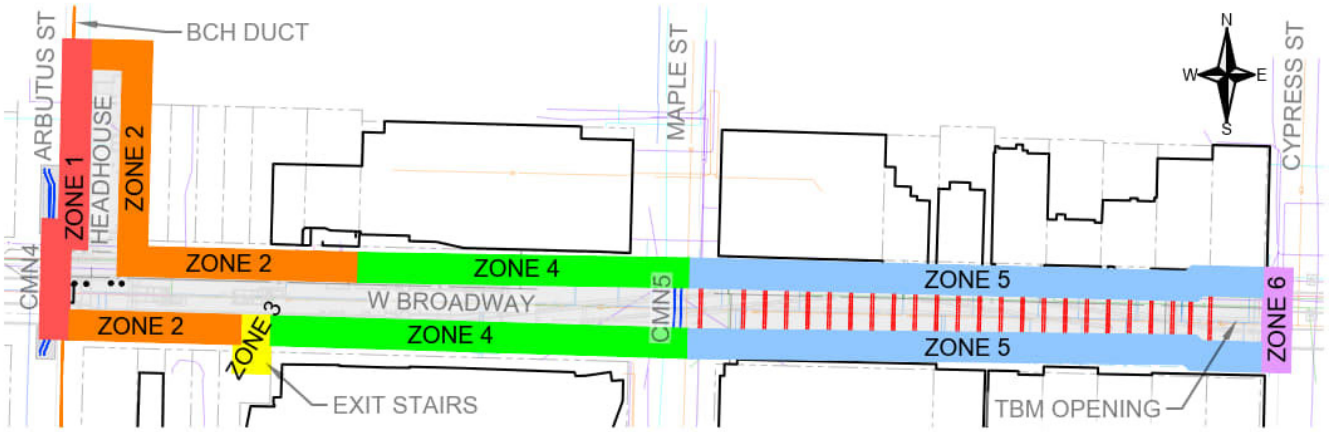


a minimum depth of 1.5 m as specified and approved by the City of Vancouver (City of Vancouver 2019). Therefore, design solutions need to be practicable with respect to methods and materials.

Zone 1 is located along the west excavation face beside Arbutus Street and will be required to support the CMN4 and a concrete BC Hydro duct bank in addition to accommodating openings through the shoring face where tail track tunnels will be created. Encroachment of shoring elements, such as tie-back anchors, are permitted into adjacent areas; however, these anchors are required to have prescribed offsets from the CMN4 to ensure damage is avoided.

CMN4 is located along and under Arbutus Street at depths of about 2.0 to 5.5 m at locations adjacent to the west excavation face. Assessments of the CMN4 were carried out as part of the project and determined to require an approximately 50 m long segment of the pipe to be relocated to address potential risk associated with station excavation and the tail track tunnel works (BSCGP 2023a). The relocated segment CMN4 will be located approximately east of the existing pipe and at higher elevations. Connection of this new pipe segment to the existing CMN4 pipe will occur in caged areas located west of the Headhouse and outside of the southwest corner of the excavation footprint.

The BC Hydro duct bank contains various conduits and is aligned approximately parallel with Arbutus Street. The northern approximate 50 m of this duct bank is situated about 1 m or less from the back of the west excavation face and thus would be supported by the excavation shoring. However, the west excavation face has a jog in the footprint that moves the shoring face about 4.7 m to the west which results in the duct bank to be located in front of the shoring face for a length of about 26 m before intersecting the south excavation face. Relocation of this duct bank is not permitted; therefore, the duct bank needs to be suspended above the construction area.

The tail track tunnels will result in two openings through the west excavation face at areas adjacent to the southwest corner of the project site. The bottom of these tunnel opening will be at elevations slightly above the excavation base. Each tunnel opening will be about 6 m wide by 6 m high with about 6.5 m of separation between the two tunnels. These tunnels extend westward from Arbutus Station and are intended to facilitate the future terminus box. Use of steel reinforcing, such as welded wire mesh, in the shoring face or metallic tie-back anchors at these tunnel openings are to be avoided due to potential conflict with or damage to tunnel excavation methods. Furthermore, cementitious shotcrete with a compressive strength of greater than 35 MPa should also be avoided.

Zone 2 is located along the north and east excavation faces at the Headhouse, and the western approximate 63 m and 55 m of the north and south excavation faces along Broadway, respectively. The excavation shoring system will need to support adjacent buildings with no deep basement levels and typical underground utilities. The north and east excavation faces at the Headhouse are also required to support a maximum 15 kPa vertical surcharge pressure from machinery/vehicles placed within approximately 7 m behind the excavation face. Encroachment of shoring elements, such as tie-back anchors, are permitted into adjacent properties.

Zone 3 is an approximately 10 m deep excavation area located behind the south excavation face where exit stairs are to be constructed. The footprint of this excavation area is less than 6 m wide by 9 m long and is connected to the station excavation via an approximately 4 m wide by 5 m long access way. Widening this excavation footprint is not desirable since the public walkway in this area would be further restricted during construction.

Zone 4 is located along the north and south excavation faces of Broadway and generally extending approximately 95 m and 120 m west of Maple Street, respectively. The excavation shoring system will need to support adjacent buildings with basement levels and typical underground utilities. The excavation footprint in this zone jogs closer to the neighbouring properties to the north and south; thus, reducing the distance between the shoring face and adjacent buildings in comparison with Zone 2. At Maple Street, CMN5 is aligned approximately north-south and intersects the excavation footprint. CMN5 is to be suspended across the open excavation using pipe cradles at abutment girders located at each side of the excavation in addition to hangers evenly spaced and hung from a girder bridge (BSCGP 2023b). The excavation shoring at CMN5 will need to be stepped into the slope to accommodate the structural components for supporting the pipe.

Zone 5 is located along the north and south excavation faces of Broadway between Maple Street and Cypress Street. The excavation shoring system will need to support adjacent buildings with basement levels and typical underground utilities. Encroachment of shoring elements into neighbouring properties is not permitted. At the east side of the Maple Street and Broadway intersection, an unobstructed opening across the excavation footprint from the excavation bottom to ground surface is required. This opening extends about 19.5 m north-south across Broadway and about 11 m east-west along Broadway. A second opening located beside the east excavation face at Cypress Street will be required to facilitate removal of the tunnel boring machines. This second opening extends about 21 m north-south across Broadway and about 14.5 m east-west along Broadway.

Zone 6 is the east excavation face at Cypress Street. This excavation shoring system will need to support the traffic in addition to four 3 m by 3 m crane outrigger pads that exert an estimated 150 kPa surcharge pressure at each pad. The western set of outrigger pads may be setback 1.5 m from the excavation face. Below the outrigger pads, the tunnel boring machines will penetrate the shoring face to enter the excavation area. Each tunnel is about 6 m diameter with a separation of about 4 m between the tunnels. Design consideration include lateral stresses associated with the tunnel boring machine during penetration through the shoring face. Similar to Zone 1, use of steel reinforcing and metallic anchors are not permitted at the tunnel openings due to potential damage to the tunnel boring machines. Furthermore, the shotcrete strength is limited to 35 MPa or less.

# Design Solutions

The design solutions developed for the excavation shoring zone as previously described required an iterative process with design team members and stakeholders. The design strategies needed to be flexible to adapt to updated information as verification of subsurface conditions was carried out. Moreover, changes to the design details would be required to address other considerations including construction sequencing, surcharge loads, available materials, and updated excavation geometries. The 4 general types of shoring system used in the design solutions consisted of:

- tensioned tie-back anchors and reinforced shotcrete infill panels,
- pipe piles with tensioned tie-back anchors and reinforced shotcrete infill panels,
- braced soldier piles with spiles and shotcrete infill panels, and
- secant piles with reinforced shotcrete waler and steel waler, tensioned with tie-back anchors.

Tie-back anchors are required to be recessed into the shoring face to facilitate the building construction. A summary of the design solutions applied to each of the zones are discussed as follows.

## Zone 1

Due to the presence of the CMN4 pipe and hydro duct bank at depths above approximately 5 m, the design solution at the north portion of the west excavation face consisted of 150 mm diameter, Schedule 80, pipe piles installed with a 1.2 metre-on-centre spacing with 200 mm thick, reinforced shotcrete infill panels and tensioned tie-back anchors at depths below 3.5 m as shown in Fig. 5. The pipe piles function as a cantilevered retaining wall and are approximately 9 m long with the lower half of the pipe length secured to the excavation face by the tie-back anchors. Anchor lengths varied from about 4 to 14.5 m and are tensioned to provide lateral resistance to earth pressures and the pipe piles. At the southern portion of the west excavation face, an upper benched geometry was incorporated into the shoring geometry to facilitate the relocated segment of CMN4 and allow the pipe pile lengths to be shortened to about 5.5 m as shown in Fig. 6.

Where the BC Hydro duct bank is located in front of the shoring face, a series of hangers would be attached to the exterior of the pipe piles and include an arm that extends out to and above the duct bank. From these overhead hangers, the duct bank would be suspended above the excavation area. Where the excavation face jogs in the area beside the tail track tunnel opening, additional pipe piles extending below the excavation bottom would be installed to provide additional support to the duct bank.

**Fig. 5.** Shoring solution at north portion of west excavation in Zone 1

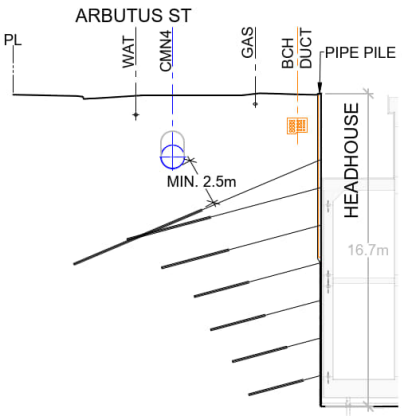


**Fig. 6.** Shoring solution at south portion of west excavation in Zone 1

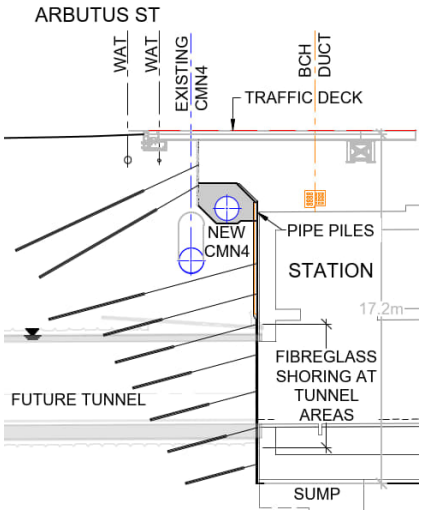


At the tail track tunnel openings, the design solution utilized 35 MPa shotcrete with fibre rebar mat as reinforcement and fibreglass anchors for tie-backs. These materials were confirmed to be compatible with the tunnelling works. At elevations above the tunnel openings, pipe piles with tensioned tie-back anchors and reinforced shotcrete infill panels were use in the design solution as shown in Fig. 7. To address an area where a pipe pile could not be located, additional 15M horizontal reinforcing steel bars were included in the shoring face design to span across adjacent pipe piles.

## Zone 2

Tensioned tie-back anchors and reinforced shotcrete panels were utilized for the design solution as shown in Fig. 8. Anchor lengths varied from about 3 to 13 metres using #7 to #9 anchor bars installed with 1.8 m horizontal spacing. This design accounted for the surcharge pressure from machinery/vehicles placed behind the excavation face.

## Zone 3

The design solution consisted of pipe piles with walers to form a frame and included struts to laterally brace the tunnel entrance area as conceptually shown in Fig. 9. Reinforced shotcrete infill panels would be included between the pipe piles. This design solution provided the open space to construct the stairs and did not require a larger excavation footprint. Furthermore, this “top-down” design solution addressed a constructability constraint in which a drill rig could not operate in this excavation footprint to install tie-back anchors.

## Zone 4

Due to the closer proximity of the excavation face to the neighbouring buildings, lateral support of the upper portion of the excavation face utilized pipe piles with tensioned tie-back anchors at depth. The upper rows of anchors require installation with steep dip angles to avoid the adjacent basement foundation walls as shown in Fig. 10. Pipe piles varied up to 11 m long and in some locations required 250 mm diameter, Schedule 80 pipes to manage design loads and deformations.

At the CMN5 support abutment locations, a bench was advanced to depths of 5 m with the balance of the excavation face advanced to design depths for the building structure. At areas immediately adjacent to this bench, pipe piles with tie-back anchors and shotcrete infill panels would be used for the excavation support. The bench cut extended about 2 m into the slope and about 3.5 m wide at the excavation face. The side walls of this bench cut are laterally supported by pipe piles and 15M horizontal steel bars in the shotcrete panels. Pipe piles also bound the edges of this bench in elevation as shown in Fig. 11.

## Zone 5

Braced soldier piles with spiles and shotcrete infill panels are utilized for the design solution since there is no permission for encroachment into neighbouring properties. Struts extending from the north to south excavation faces are connected to walers and provide lateral support to the soldier piles as shown in Fig. 12. For the opening located beside Maple Street, additional walers and struts were required in the shoring elements forming the edges of this open area. For the opening beside Cypress Street, the larger open area and ground conditions required additional double walers and multiple struts to create a frame as conceptually shown in Fig. 13.

## Zone 6

The design solution consisted of 900 mm diameter secant piles with reinforced shotcrete waler and tensioned tie-back anchors. Reinforcements installed at secondary secant piles that do not intersect the tunnel opening will consist of H-beams. Secant piles located above the tunnel footprints

**Fig. 7.** Elevation view of shoring solution at tail track tunnel openings in Zone 1

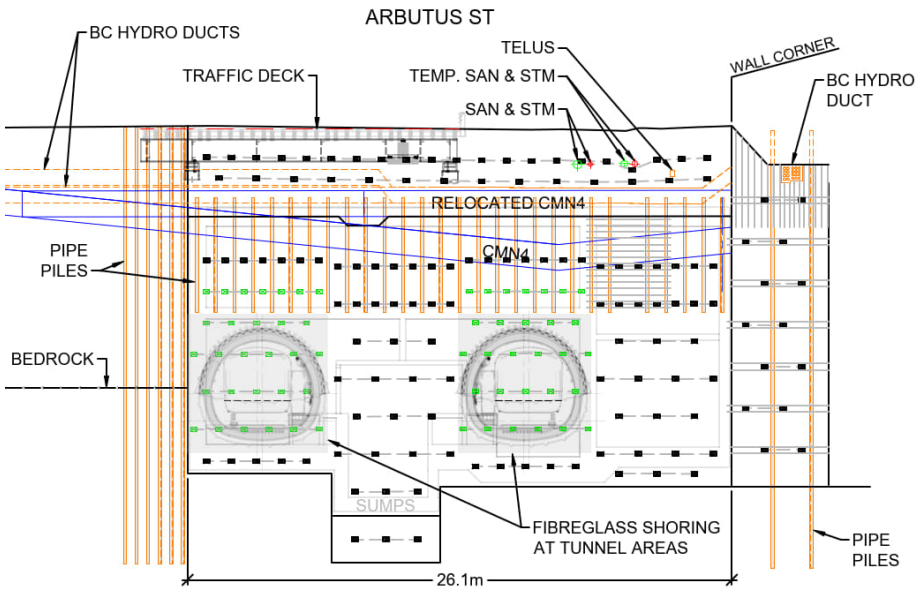


**Fig. 8.** Zone 2 shoring solution using tie-back anchors and reinforced shotcrete

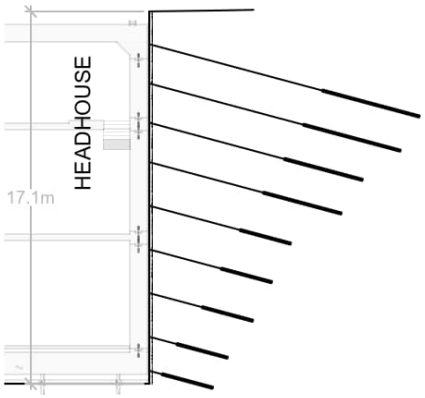


**Fig. 9.** Conceptual design solution for Zone 3

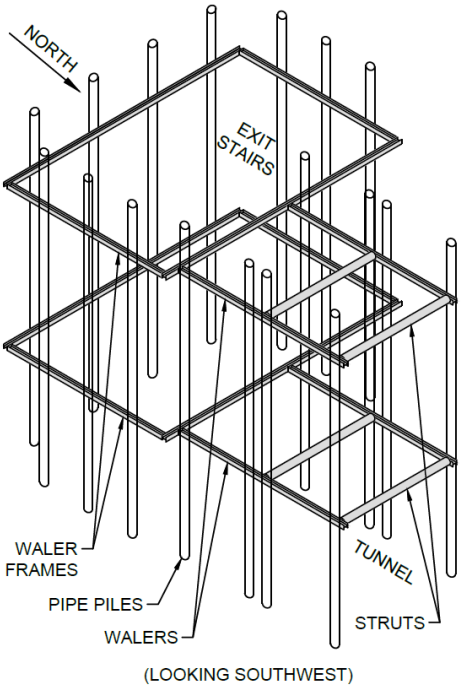


are designed to be installed as a hybrid primary and secondary pile. For these hybrid secant piles, a steel cage would be suspended at elevations in the pile that are above the top of tunnel micropile canopy. The balance of the pile at lower elevations would not have reinforcing steel and would function as primary piles. Concrete used in the piles that intersect the tunnel openings would have a maximum strength of 10 MPa to allow the tunnel boring machine to penetrate the shoring face. The design of this shoring face requires careful planning to avoid conflict with the tunnel components. In addition to low strength concrete, fibreglass tie-back anchors would be used at the tunnel openings.

Details for this shoring solution are complicated and require compatibility with the shoring system in Zone 5 used to provide the open area that will facilitate removal of the tunnel boring machines. Furthermore, surcharge loads from crane outrigger pads and adjacent traffic are included in the design details. An elevation view of this design solution is shown in Fig. 14.

## Instrumentation and Monitoring

As part of the construction risk management for this project, pre-construction surveys of buildings and existing infrastructure were carried out. Instrumentation and survey

**Fig. 10.** Typical pipe pile and tie-back anchor shoring solution in Zone 4

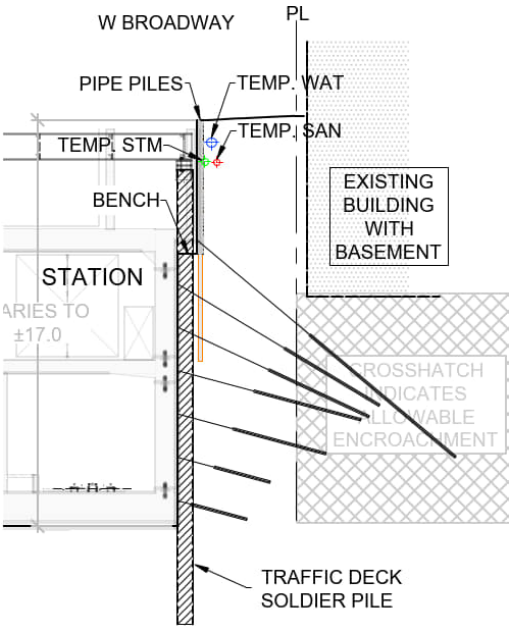


**Fig. 11.** Elevation view of shoring solution for CMN5 abutment area in Zone 4

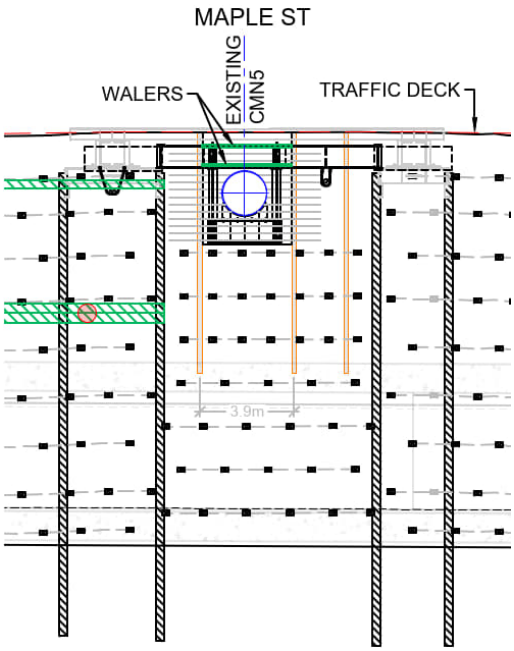


monitoring for buildings, the CMN4 and CMN5 pipes, and excavation faces are included in the design. For CMN4, the instrumentation and monitoring will include settlement monitoring gauges along the length of pipe that may be impacted by the tail track tunnels and station construction works and visual inspections during excavation. For CMN5, the instrumentation and monitoring will include settlement monitoring gauges at either end of the in-ground portion of the pipe, survey targets and nano sensor tilt meters on the exposed portion of the pipe, strain gauges on the girder bridge components, and visual inspections during excavation. The instrumentation and monitoring for the excavation shoring will include optical survey targets on buildings and excavation faces, inclinometers, strain gauges on select struts, nano sensor tilt metres, and InSAR satellite surveys. Measured movements would be compared with defined threshold values that trigger specific reviews to be carried out and responses to avert unacceptable risk conditions for excavation slope stability or damage to infrastructure, utilities, and buildings.

**Fig. 12.** Typical braced soldier shoring solution in Zone 5

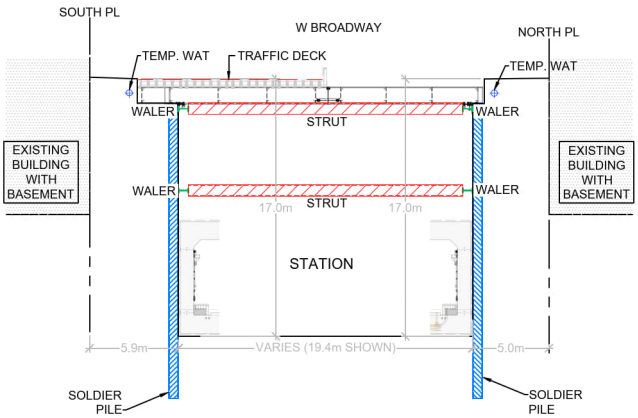


**Fig. 13.** Conceptual shoring solution using walers and struts at Cypress Street opening in Zone 5

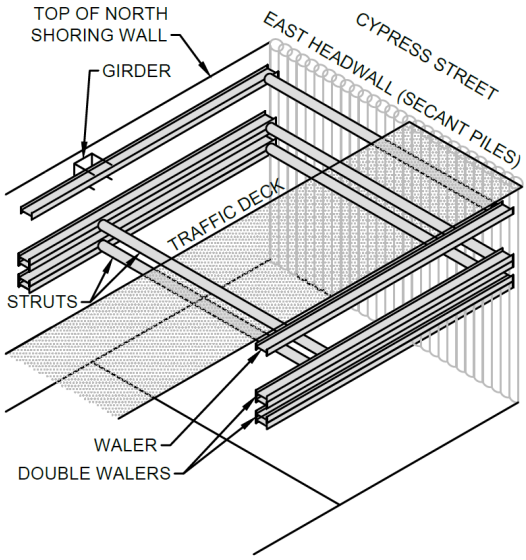


## Conclusions

The geotechnical design challenges encountered at the Arbutus Station and Double Crossover project site required an iterative design process to develop practicable solutions

**Fig. 14.** Elevation view of shoring solution at Cypress Street in Zone 6

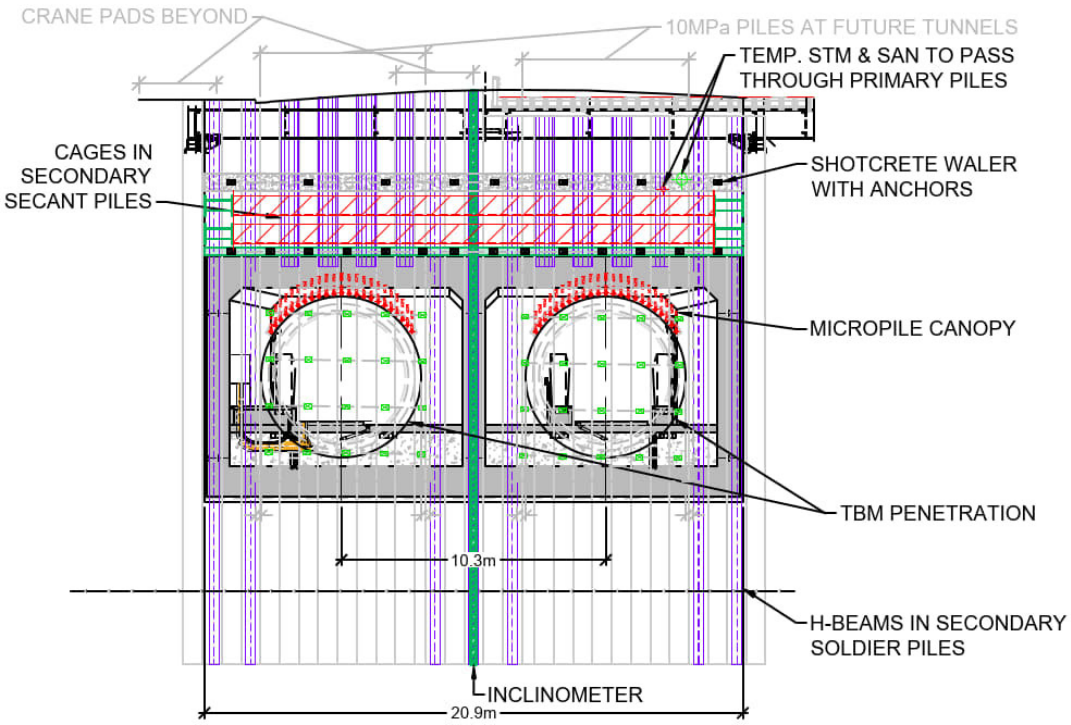


for the temporary excavation supports. Collaborative effort and communication between design team members were important to avoid conflicting details where different designs and purposes interface. The different complexities in the design solutions for this project reflect the range of constraints that govern practicable design options. Where there are less design constraints, a comparatively more straightforward design solution can be used. Conversely, increased number of design constraints resulted in more complicated design solutions. Another important factor that assists with managing the design challenges is additional verification of subsurface soil and groundwater conditions, locations of underground utilities, and locations of adjacent underground structures, such as basement foundation walls. By accurately determining these constraints, the design solution can be more optimal in addition to having better risk management associated with potential impacts to these utilities and structures.

The authors would like to thank the project owner, the Province of B.C., as well as the Broadway Subway Constructors General Partnership, and other stakeholders for their support for this paper.

## References

Armstrong, J.E., Hicock, S.R. 1979. Geological Survey of Canada, "A" Series Map 1486A.1 sheet.

BSCGP 2023a. CRIAR Report – Capilano Main No.4 Water Pipeline. BSP-BSCGP-DES-RPT-00021.

BSCGP 2023b. CRIAR Report – Capilano Main No.5 Water Pipeline. BSP-BSCGP-DES-RPT-00022.

BSCGP 2023c. CRIAR Report – Arbutus Station and Double Crossover. BSP-BSCGP-DES-RPT-00023.

City of Vancouver 2019. Construction Specifications, First Edition.

EXP 2021. Geotechnical Design Report for Capilano No. 4. BSP-BSCGP-GEO-RPT-00024 RB.

Golder 2019a. Geotechnical Data Report. Broadway Subway Project. 1419105-050-R-Rev1.

Golder 2019b. Geotechnical Characterization Report. Broadway Subway Project. 1419105-056-R-Rev0.

# What We Know About High-Strain Dynamic Testing of Steel Pipe Piles with Concrete Plugs

David J. Tara, M.Sc.A., P.Eng.
Geotechnical Engineer, Thurber Engineering Ltd., Vancouver, BC.

Tareq Dajani, M.Eng., P. Eng.
Geotechnical Engineer

**ABSTRACT** Open toe steel pipe piles in granular soils often fail to plug during impact driving. This can result in excessively long piles to achieve the designer's termination criteria and corresponding required geotechnical resistance. Plugging of piles can be induced using either an internal diaphragm plate or a concrete plug of limited length. This paper will review the results of simulations and actual high-strain dynamic testing (HSDT) completed on piles with a concrete plug along with a discussion on the challenges related to signal matching. The paper provides general, yet preliminary, guidance on dynamic testing and signal matching of steel pipe piles with concrete plugs.

## Introduction

Driven steel pipe piles, widely used as bridge foundation support in the transportation and energy sectors, often require a minimum embedment for lateral resistance due to high seismic demands and for scour protection. Where the foundation soils are particularly dense or cobbles and boulders are present above the desired pile toe elevation, there is a risk of encountering early refusal or sustaining pile damage during impact driving. To control these risks, piles may be initially advanced by drilling to some minimum embedment, followed by impact driving to the specified termination criterion. This installation sequence may require a significant amount of additional pipe if the piles core. To increase the pile toe resistance, steel pipe piles are sometimes modified during installation by placement of concrete over a limited length of the interior of the pile to create a plug. This paper will review some of the challenges related to this approach, in particular the interpretation of high-strain dynamic testing (HSDT) results and provide a suggested approach to testing and signal matching.

## Effect of plug on pile impedance and behaviour

Typically, HSDT is conducted on hollow steel pipe piles (i.e., no concrete plug) with a closed or open toe, or on fully-concreted pipe piles. In both cases, the pile impedance is known, or can be defined relatively easily, and is often constant. Construction of a concrete plug introduces a significant impedance contrast along the pile which is reflected in the HSDT force (F) and impedance times velocity (Zv) signals, and upwave [U↑ = (F – Zv)/2]. The impedance contrast along the concreted section can be substantially larger than that of the steel pipe section depending on the pile diameter. As noted in CFEM 2006 and Fellenius (2023), impedance contrasts of 2 or more have the potential to result in driving difficulties.

The construction of a concrete plug also introduces uncertainties related to the pile properties (i.e., composite modulus, density, etc.) and behaviour (i.e., bond versus slippage condition at the concrete/steel interface) of the concreted section of the pile. Separating the effects of the impedance change introduced by the concrete plug and the behaviour of the concrete plug, from the resistance of the soil surrounding the pile with any degree of confidence is difficult. This can also be further complicated by the relative location of the concrete plug along the pile and the relative length of the concrete plug.

## Simulation of the dynamic response of open toe pipe pile with and without concrete plug

To demonstrate the effect of a significant impedance contrast on the dynamic response of a pile, simulations were conducted using the software AllWave-PDP by Allnamics of The Netherlands which uses the Method of Characteristics. A 610 mm x 12.7 mm open toe pipe pile with an embedment of 30 m was selected. The shaft resistance was assumed to increase linearly with depth from zero at ground surface to a maximum of 60 kPa at the toe. For the base case condition (i.e., pipe pile with no concrete plug), a toe resistance of 30 MPa (i.e.,

$q_c$ = 30 MPa) was applied only to the steel section of the pile toe, which represents coring behaviour. Shaft and toe damping were assumed to be proportional to the modelled shaft and toe resistances and soil quakes were 2.5 mm. Fig. 1 shows the resulting F and Zv traces versus time and Fig. 2 shows the corresponding plot of U↑ versus time. Note that the pile is shown schematically in the bottom left of the figures and the toe of the pile is indicated by the vertical dashed line.

**Fig. 1.** F and Zv versus time for unplugged pile simulation (base case).

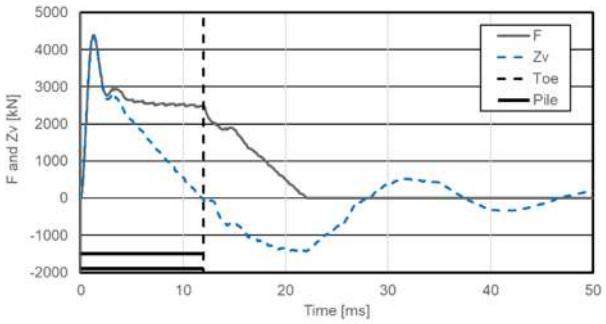


**Fig. 2.** Upwave U↑ versus time for unplugged pile simulation (base case).

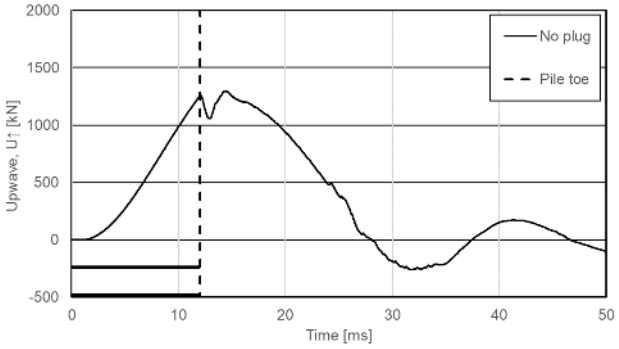


To visualize the effect of a concrete plug, we considered two lengths of plugs (i.e., 6 m and 12 m), both constructed 1.5 m from the pile toe. For both cases, the dynamic response of the pile was modelled in two stages. In the first stage shown in Fig. 3 (Scenario #1), the shaft and end bearing resistances were modelled in the same manner as the base case. The pile wall thickness was doubled within the 6 m concrete plug section to reflect the impedance change. The pile and concrete plug are shown schematically in the lower left of the figure. The green dashed vertical line represents the limits (top and bottom) of the concrete plug and the black dashed line the location of the pile toe. This stage represents the pile response during the first few blows of a dynamic loading test conducted after the concrete has set and is essentially considered to be a coring condition.

**Fig. 3.** Simulation of the base case scenario (open toe pile with no concrete plug) and Scenario #1 (increased pile wall thickness along 6 m concrete plug section)

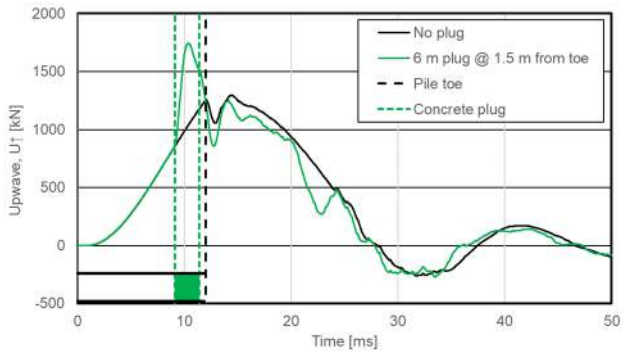


In the second stage shown in Fig. 4 (Scenario #2), the shaft resistance was modelled in the same manner as the base case and the pile wall thickness was doubled within the concrete plug section similar to the first stage. The end bearing was modelled as a closed toe condition and was assigned a value of 6 MPa which represents the equivalent of a soft soil plug condition (i.e., $q_{b10}$ = 0.2$q_c$ = 6 MPa) (Fleming et al., 2009).

**Fig. 4.** Simulation of the base case scenario (open toe pile with no concrete plug) and Scenario #2 (increased pile wall thickness along 6 m concrete plug section and an end bearing resistance corresponding to a soft plugged pile)

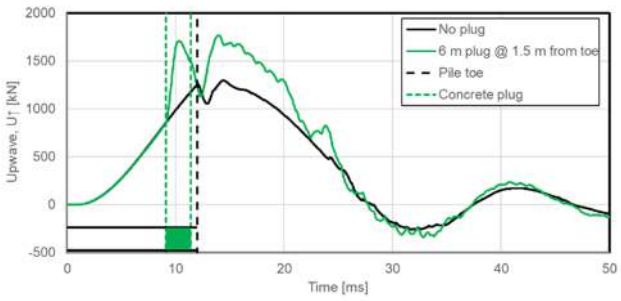


In the second case, everything was modelled the same except the length of the plug which was doubled. Fig. 5 shows the upwaves for the base case (no plug), Scenario #3 which is an early blow (coring condition similar to Scenario #1) and Scenario #4 which is a later blow when a soft soil plug starts to develop.

**Fig. 5.** Simulation of the base case scenario (open toe pile with no concrete plug), Scenario #3 (increased pile wall thickness along 12 m concrete plug section and coring condition) and Scenario #4 (soft soil plug condition)

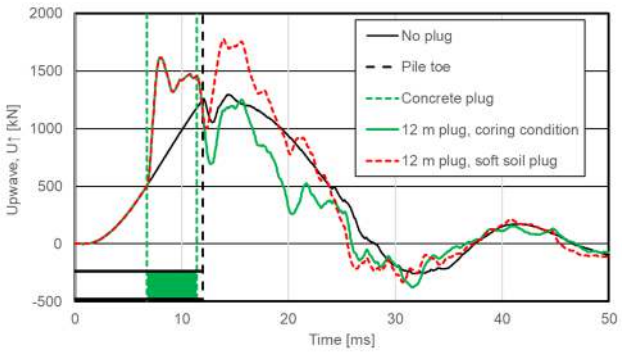


By inspection, the concrete plug overwhelms the dynamic response of the pile. Further, the measured response becomes more complex during the transition from the coring condition (initial blows) to later blows. The reality in the field is that it is rare to find a uniform soil deposit as was used in this example and even more rare to find a concrete plug that performs as assumed in the model herein (i.e., equivalent to an increase in pile wall thickness).

## Recent case histories

In 2022 and 2023 the authors were involved with HSDT and signal matching on several projects that included the use of concrete plugs. On one project, piles were subjected to HSDT before and after placement of the concrete plugs.

At this site, the subsurface stratigraphy consisted of compact to dense granular fill over coarse-grained alluvial deposits underlain by sand with some silt and a trace to some gravel. The foundations comprised 914 mm x 19.1 mm steel pipe piles that were drilled in through the coarse-grained deposits and then advanced by impact driving using a Junttan HHK12 hydraulic hammer with a 12,000 kg ram. The piles were advanced to 45 m to 50 m embedment without attaining the desired termination criterion. In hopes of inducing plugging and in turn increasing the penetration resistance, concrete plugs were added to some of the piles.

Using the available drilling equipment which had a limited reach compared to the pile embedments, the concrete plugs were only installed to about 26 m below the pile head. This resulted in concrete plugs that were constructed relatively high in the piles. Nonetheless, upon redrive, the penetration resistance increased from about 20 blows per 250 mm before placement of the concrete plug to refusal using the same hammer that was operated at the maximum energy setting of about 160 kJ. In comparison, piles without concrete plugs only saw the penetration resistance increase to 30 blows per 250 mm on redrive.

Prior to signal matching, the successive measured upwave signals were plotted from the testing completed before and after placement of the concrete plug. This process of comparing multiple signals is referred to as signal stacking and is the preferred “old school” approach to analysing low strain integrity test results in Europe (Bielefeld et al., 2022). With signal stacking, multiple measured signals are plotted to evaluate and compare the quality of the measured signals. In the case of sonic integrity testing (SIT) and HSDT, signal stacking can be used to evaluate the performance of individual piles or groups of piles and to identify outliers as similar sized piles of similar length installed in the same soil strata should show the same reflections. This method can then be used to identify signals or piles that differ from the group. Where this method is most powerful is when it comes to assessing the integrity of an anomalous pile. The two-phase process starts with signal matching conducted on the average signal assuming a sound or uniform pile to estimate the soil resistance distribution. With the calculated soil resistance distribution, signal matching is then conducted on the signal for the anomalous pile and the pile model is changed until a good match is obtained. The outcome of this two-phase process is an estimate of the pile impedance with depth. According to Bielefeld et al., the advantage of this approach is that “smaller anomalies can be detected than in the traditional qualitative interpretation method”. While this overall approach has gained widespread acceptance in Europe for users of the low strain integrity testing method, these concepts have not really caught on with practitioners in the HSDT domain.

Fig. 6 represents the stacking of the upwave signals of blow numbers BN 4 to BN 14 from the testing completed on the non-concreted pile. By inspection, the upwave signals are relatively consistent from blow to blow, particularly before the pile toe at 2L/c or about 39 ms.

Fig. 7 represents the stacking of the upwave signals of select blow numbers between BN 51 and BN 96, from the testing completed after the placement of the concrete plug. The plug measured 17.7 m in length and was constructed about 24 m above the pile toe. Similar to Fig. 6, the upwave signals are relatively consistent from blow to blow.

**Fig. 6.** Select stacked upwaves for DLT conducted on Pile PN12 without concrete plug

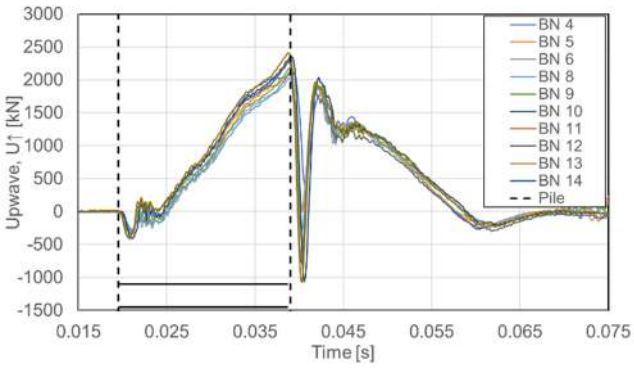


**Fig. 7.** Select stacked upwaves for DLT conducted on Pile PN12 with concrete plug

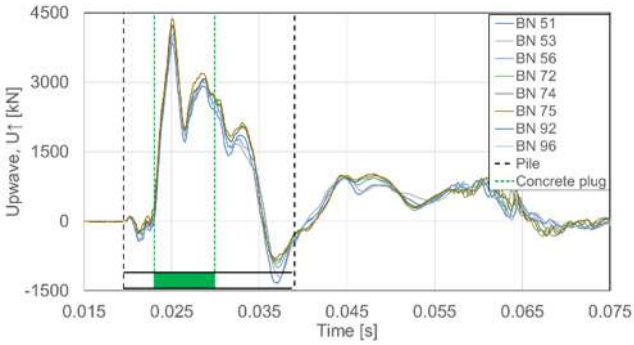


Fig. 8 provides a direct comparison of the upwave signals from the testing completed before (BN 14) and after the placement of the concrete plug (BN 74). The comparison clearly demonstrates the effect of the concrete plug on the dynamic response of the pile. Further, the dynamic response of the pile below the concrete plug location is also markedly affected between 0.03 and 0.04 seconds (see figure). This represents the section of the pile between the concrete plug and the pile toe.

Signal matching was initially attempted by analysing the HSDT results of the pile with the concrete plug. The analysis was time consuming, the matches relatively poor and the results were questionable given the uncertainty in separating the effects of the impedance contrast from the soil resistance. The analysis was further complicated by the excessive length and relatively shallow location of the concrete plug.

To reduce the uncertainties in signal matching, the authors proceeded with an alternative analysis where the shaft resistance parameters (i.e., yield and damping) were assessed from the HSDT completed before placement of the concrete plug as is done with SIT in Europe. Fig. 9 shows the signal matching results of blow BN14 that was completed using the software IMPACT (Randolph, 2008). The figure includes plots of force and impedance times velocity, upwave, displacement and work versus time and the accompanying match. Also shown is the shaft resistance distribution, a plot of pile head displacement versus work and a summary of the estimated resistances, etc.

**Fig. 8.** Comparison of select upwaves for DLTs conducted on Pile PN12 with and without concrete plug

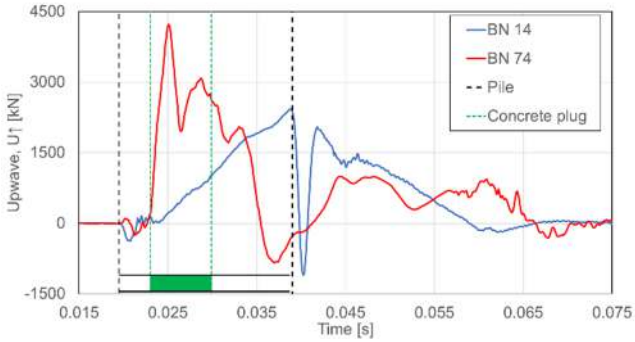


The match quality was reasonably good, with a mobilized shaft resistance of 2.6 MN and a toe resistance of 2.6 MN.

Signal matching was subsequently completed on the HSDT results collected after the installation of the concrete plug. Blow BN74 was selected to complete the analysis using IMPACT. Using the shaft resistance derived from the former analysis, the only parameters that were varied were the pile impedance along the concrete plug section and the pile toe resistance. The concrete plug was modelled as a series of seven lumped masses of 2.5 m in length. The lumped masses were initially set equal to the actual mass of concrete over the 2.5 m length but were reduced in the top three masses until a reasonable match was obtained. The end bearing was modelled as a closed toe condition.

The analysis was completed with relatively little effort to obtain a good match quality. Fig. 10 shows the signal matching results of Blow BN74. The analysis indicated a mobilized shaft resistance of 2.6 MN and toe resistance of 3.9 MN, representing an increase in resistance of about 1.3 MN.

Using the same two stage approach, an independent analysis was completed using the software AllWave DLT by Allnamics. Relatively little effort was required to complete the analysis, with very similar results obtained. In AllWave-DLT, the concrete plug section of the pile was modelled as a solid concrete section.

**Fig. 9.** Signal matching results for blow BN14, without concrete plug

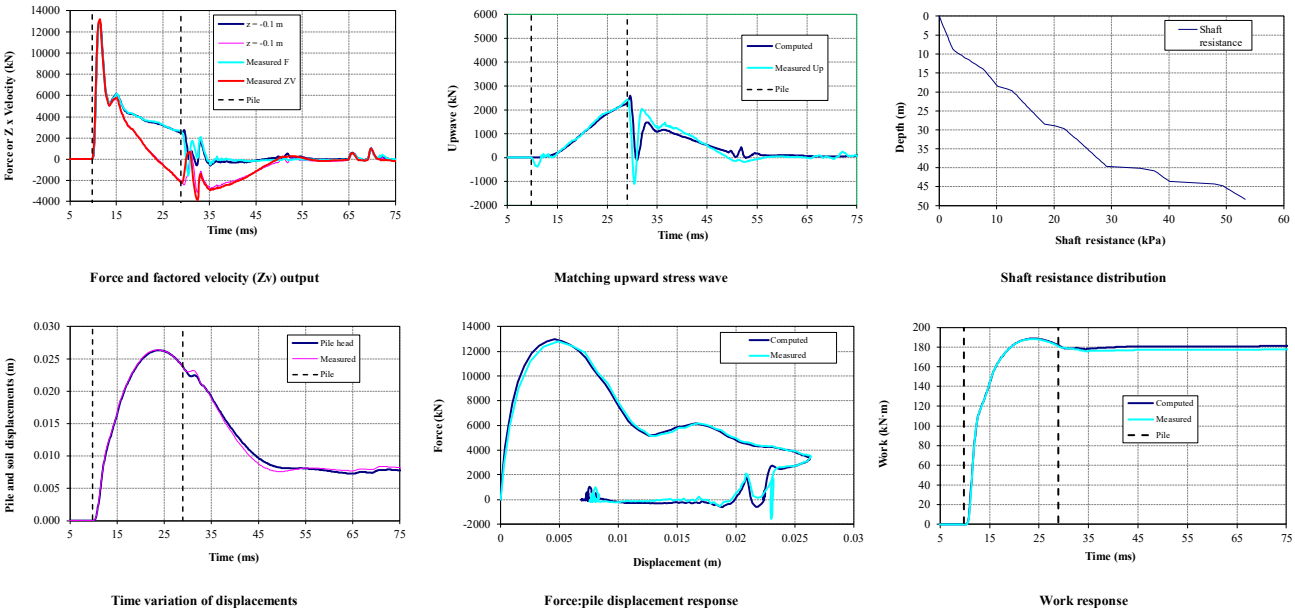


**Signal Matching Output**

| Case No. | Pile Embed. m | Shaft Capacity kN | Base Capacity kN | Total Capacity kN | Maximum Energy kJ | Maximum Disp. mm | Permanent Set/Blow mm | Maximum Pile Stress MPa | Minimum Pile Stress MPa |
|---|---|---|---|---|---|---|---|---|---|
| 1 | 48.6 | 2601 | 2624 | 5225 | 189 | 26.1 | 7.4 | 243 | -13 |

**Fig. 10.** Signal matching results for blow BN74, with concrete plug

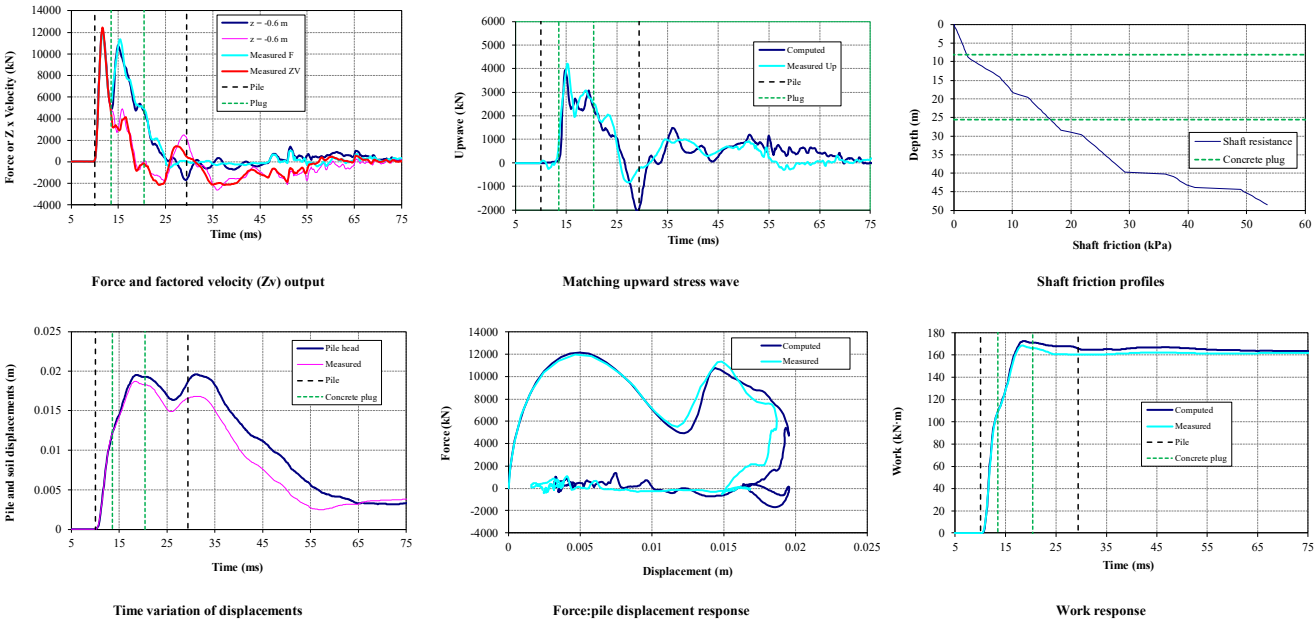


**Signal Matching Output**

| Case No. | Pile Embed. m | Shaft Capacity kN | Base Capacity kN | Total Capacity kN | Maximum Energy kJ | Maximum Disp. mm | Permanent Set/Blow mm | Maximum Pile Stress MPa | Minimum Pile Stress MPa |
|---|---|---|---|---|---|---|---|---|---|
| 1 | 48.8 | 2632 | 3937 | 6569 | 173 | 19.6 | 3.3 | 323 | -62 |

## Summary

Open toe, driven steel pipe piles may be modified with a concrete plug to increase toe resistance. However, signal matching of such piles must consider increased uncertainty that is introduced by the impedance contrast along the pile section. Based on the authors' recent experience, the reliability of signal matching of piles with concrete plugs can be improved by testing the same pile prior to concreting or an adjacent open toe pile of similar dimensions and installed using the same procedure. In this manner, the shaft resistance distribution can be established by signal matching of the open toe pile. Then, the analysis of the plugged pile can focus on matching the effects of the pile impedance change and the increase in toe resistance.

The authors' proposed two stage approach to signal matching was completed using IMPACT and AllWave-DLT software programs, with relatively consistent results obtained. However, additional testing is required to confirm the applicability and limitations of this approach. Further, a detailed testing program on future projects that include static loading test(s) or possibly rapid load testing would provide an opportunity to validate the assumptions. Such a testing program could also be used to assess whether the use of a concrete plug is required.

The following are the authors' preliminary guidance for sizing of concrete plugs and dynamic testing and signal matching of such piles.

- Ideally, the concrete plug should be constructed as close as practicable to the toe to avoid additional reflections before 2L/c in HSDT. The concrete plug should be constructed within a few diameters of the toe. Sometimes, however, this criterion may not be achievable for constructability reasons.
- The length of the concrete plug should be as short as possible.
- The concrete plug dimensions and construction details must be properly documented to eliminate additional uncertainty, particularly regarding plug length and debonding.
- Signal stacking provides insight on the behaviour of the concrete plug with successive blows and the overall signal quality.
- Pile drivability simulations must include the concrete plug to determine termination criterion.

## References


Bielefeld, M., van Delft, M. and Bakker, J. 2022. The rebirth of traditional SIT interpretation methods to incorporate engineering judgement in present day data analysis. *In* Proceedings of the 11th International Stress Wave Theory and Testing Methods for Deep Foundations Conference, September 20-23, 2022, Rotterdam, The Netherlands, 7 pages.

Canadian Geotechnical Society, 2006. Canadian Foundation Engineering Manual, 4th Ed., 488 pages.

Fellenius, B., 2023. Basics of Foundation Design, Electronic Edition, 548 pages.

Fleming, K., Weltman, A., Randolph, M. and Elson, K. 2009. Piling Engineering, 3rd Edition, Taylor and Francis, 398 pages.

Randolph, M.F., 2008. IMPACT dynamic analysis of pile driving, 51 pages.

# Geotechnical Evidence for the 11 kYa glacial Lake Fraser outburst flood between Abbotsford and Pitt Meadows, B.C.

Marc C. Bossé, M.Sc., P.Eng.
Thurber Engineering Ltd., Vancouver, BC.

**ABSTRACT** A glacier dammed lake in central British Columbia catastrophically failed about 11,000 years ago. Clague et al. (2021) presents evidence for the outburst flood using landforms and sediments with the focus upstream of Hope, B.C. This paper presents evidence for the flood between Abbotsford and Pitt Meadows. Carbon dates presented in the USGS Geomorphic Map of Western Whatcom County (2021) are used to assess the elevation range of the flood and identify possible flood features. The focus of this paper is a reinterpretation of the consolidation tests and CPT calibrations performed for the Golden Ears Bridge project. An unusual feature of the consolidation tests was a relatively constant over-consolidated difference with depth (i.e., OCD, $s'_p - s'$). The outburst flood provides a mechanism by which many meters of material could be scoured, and the OCD provides a crude means of reconstructing a possible pre-flood surface.

## Introduction

Direct evidence for a large glacial outburst flood on the Fraser River has increased over the past twenty years. Blais-Stevens et al. (2003) presented evidence for two such floods based on pollen and minerology analysis of two anomalous silty-clay beds collected from the seafloor of Saanich Inlet. Clague et al. (2021) evaluated flood landforms and sediments consistent with an outburst flood upstream of Hope, B.C. and drew attention to two flood scoured surfaces at Fort Langley, B.C. and Lynden, WA which have been long known of, but not previously attributed to a particular flood event. The flood was estimated to have occurred about 11,000 years ago (11 kYa) based on radiocarbon dating in Blais-Stevens et al. (2003) and 11.1 ± 0.6 kYa based on $^{10}$Be dating of relict boulders in Clague et al. (2021).

Kovanen et al. (2020) published an updated geomorphic map and interpretation of Whatcom County which is south of the Canadian border in Washington State wherein is located the Lynden scoured surface. The geomorphic map included radiocarbon dating of samples located near, and higher and lower than the Lynden scoured surface (see Figure 1). Three samples collected at Pangborn Lake to the north of the scoured surface (bog, El. +41 m) were dated to between 12.4 kYa and 11.1 kYa. One sample collected at Nolte Road to the south of the scoured surface (peat, El. +21 m) was dated to between 11.1 kYa to 10.5 kYa. In $^{14}$C years the gap between the sites is 390- to 800-years.

The elevation and interpreted age of Pangborn Lake indicates that the bog predates the flood and that the flood level could not have been higher than about El. +41 m. Otherwise, the bog deposits would have been washed out by the flood. The elevation and interpreted age of the Nolte Road site indicates that the peat deposit post-dates the flood. This would be expected as there would have been at least 10 m to 20 m of water flowing over a pre-flood bog at Nolte Road, scouring it out. The potential height of water at Nolte Road is based on the elevation of the top of the ridges within the Lynden scoured area (El. +30 m) and Pangborn Lake (El. +41 m). For comparison, the minimum estimated flood depth at Ruby Creek (within the Fraser Canyon, about 12 km west of Hope) was greater than 30 m with a minimum upper flood level of El. +57 m in Clague et al. (2021); at Hope the estimated minimum flood depth was 51 m (El. +91 m).

In this paper, we identify potential flood features between Abbotsford and Pitt Meadows, B.C., and reinterpret the consolidation tests and CPT calibrations performed for the Golden Ears Bridge (GEB) project. An unusual feature of the consolidation tests and subsequent CPT calibrations was a relatively constant over-consolidated difference (i.e., OCD, $s'_p - s'$) with depth. This was noticed by third-party reviewers who pressed for a geomorphological explanation which was not forthcoming except to refer back to the consolidation tests which showed the OCD was real. The glacial outburst flood provides a mechanism by which many meters of material would be eroded, creating the observed OCD pattern.

## Abbotsford Channel

Kovanen et al.'s (2020) interpretation is that westward flow of the proto-Fraser River past Mission, B.C. was prevented until the final disintegration of the Sumas glacier and that flow was established no later than 10,000 $^{14}$C years ago (roughly 11.7 kYa to

11.3 kYa). This would mean that the modern Fraser River alignment was less than 1,000 years old, perhaps only a few hundred years old, when the outburst flood occurred.

The change in the alignment of the Fraser River was to the east of Sumas Mountain as the intervening terrain in Abbotsford and Langley is generally higher than El. +60 m. However, there is a channel in Abbotsford that would have provided an interconnection between the two alignments during the flood (see Figure 2 and Figure 3).

The elevation profile of the channel suggests that it was a late glacial outwash channel flowing to the south (see Figure 4). It can be inferred that water would be present in the channel during the flood as it is upstream of Lynden and lower than the tops of the scour ridges (i.e., El. +27 m compared to El. +30 m).

The direction of flow in the channel would depend on the relative water levels of the Proto and Modern Fraser River alignments. The author's bias is towards northwards flow during the initial stages of the flood, trending towards slack water because of the relative width of the alignments at Sumas Mountain (i.e., ~4 km, modern vs. ~6 km, proto) and obstructions in the valley which would favour the Proto-Fraser alignment (e.g., Agassiz blocking ridge, Mt. Shannon, Chilliwack Mountain).

**Fig. 2.** Proto and Modern Fraser River with inferred connecting channel (bottom left) and significant valley hills and ridges in red (Google Earth).

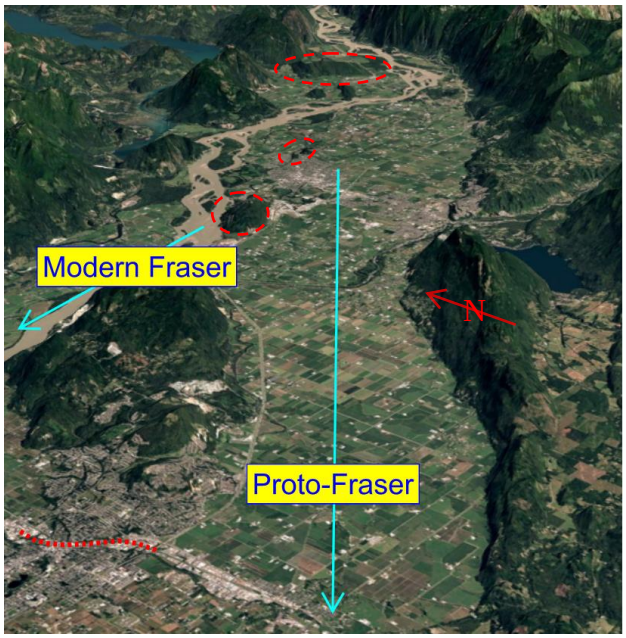


**Fig. 1.** Lynden scoured surface with location of radiocarbon samples from Kovanen et al. (2020).

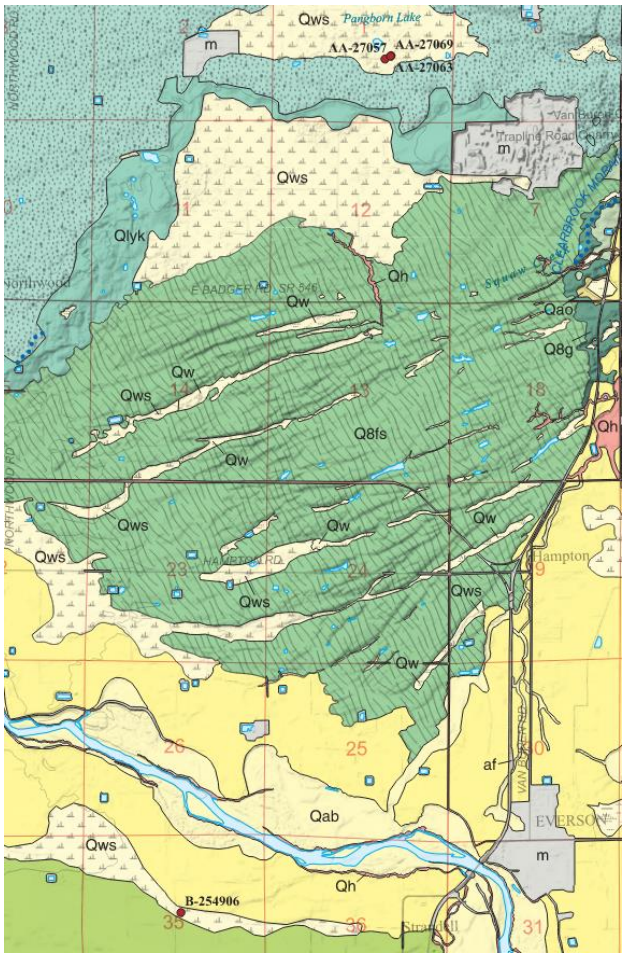


**Fig. 3.** LiDAR topographic map, 20 m contours with blue shading below El. +40 m, invert in red.

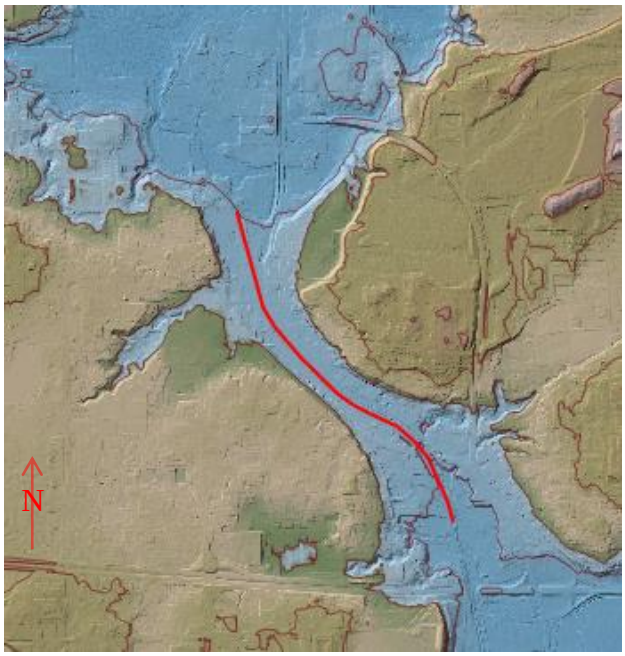

**Fig. 4.** Elevation profile along red line in Figure 3 with Sta. 0 at north end.

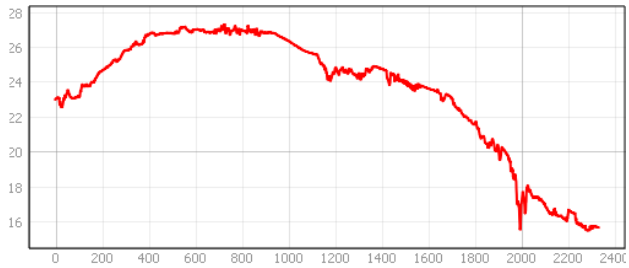


## Golde Ears Bridge

Golden Ears Bridge was constructed between 2006 and 2009 to provide a crossing of the Fraser River between Highway 1 at Surrey-Coquitlam and Highway 11 at Mission-Abbotsford, which are about 50 km apart. The alignment crosses the entire width of the modern Fraser River alignment, from upland terrain in Surrey, well above the flood at El. +60 m, to lowland terrain to the north of Maple Ridge (i.e., road at El. +2 m, ridge at El. +30 m). The extent of the mainline works is shown in Figure 5.

The Fort Langley scoured surface can be seen towards the bottom right of Figure 5. The top of the streamline ridges are at about El. +15 m. The high ground at the north end of the scoured surface is at about El. +30 m and was the site of an old gravel pit which was characterised as a Gilbert-type foreset with northwest dipping beds and being about 13,000 years old (Clague et al. 2021).

**Fig. 5.** Approximate extents of Golden Ears Bridge mainline on LiDAR topographic map (contours: red at 10 m, black at 5 m, blue shading used below El. +9 m.)

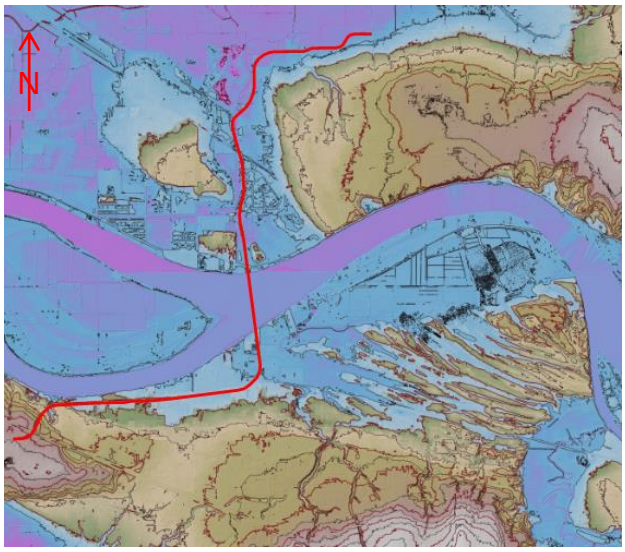


## Site Investigation

The design phase site investigation for the Golden Ears Bridge project comprised 91 CPTs (cone penetration test), 19 SCPTs (seismic cone penetration test), 76 augers holes, 54 mud rotary holes, and eight ODEX holes.

At eight locations along the alignment, deep mud rotary holes were advanced near the CPT or SCPT and many vane shear tests performed, and many piston tube samples collected for consolidation testing. The goal was to establish reliable correlation parameters for shear strength and over-consolidation which could be applied to nearby CPTs and reduce the number of mud rotary holes required. This was an important consideration as the heavily tested mud rotary holes would often take a week to complete whereas a deep CPT could often be done in a day or two.

The piston tubes used for sampling were typically standard 3” (76 mm) tubes, or standard 3.5” (89 mm) tubes if the sample was obtained below about 19 m. At BH06-43 on the north bank of the river, flush ended, thin wall tubes with a 5° cutting angle were used.

## Consolidation Testing

The consolidation testing program was developed using Ladd & DeGroot (2003) as a refence. Samples were prepared by cutting the piston tube into 100 mm to 150 mm lengths using a hand portable bandsaw. A hole was drilled along the edge of the tube and a guitar string used to saw along the perimeter of the sample. The sample was then pushed out by hand (or the sample extruder if not possible by hand) and cut into the consolidation ring.

Standard lever arm machines were used with a modified loading procedure. Two load increments were placed each day, usually 8 to 10 hours apart. The load increment was x1 below the inferred pre-consolidation pressure and x2 above it (e.g., 100 kPa to 150 kPa not 200 kPa). This was done to improve the characterisation of the e-log s curve in the vicinity of the pre-consolidation pressure.

About half of the samples (25 of 52) had less than 2% strain when re-loaded to their in-situ effective stress, 20 samples were between 2% and 4% and 7 samples were between 4% and 7%.

## Calibration with CPT Data

The $N_{qt}$ correlation parameters were selected on a project-wide basis using a bounding approach. The goal being to have most of the interpreted pre-consolidation pressures fall between the two bounding lines (see Figure 7). Low deviations were reviewed and generally occurred in shallow, young,

organic-rich deposits where the consolidation test had more than 4% strain at the in-situ effective stress indicating sample disturbance which would be expected to lower the interpreted pre-consolidation pressure. High deviations were less of a concern as it would result in a conservative interpretation of OCD. The $N_{qt}$ values selected were 3.4 and 4.0.

Figure 6 and Figure 7 show an OCD pattern that was consistently observed throughout the Golden Ears Project. Namely, a relatively stable magnitude of over-consolidation with depth. The magnitude of OCD varied by segment and from hole to hole, roughly as follows:

**Fig. 6.** OCD from CPT and consolidation tests (from GEB Factual Report, BH06-62 / SCPT06-62, Trow).

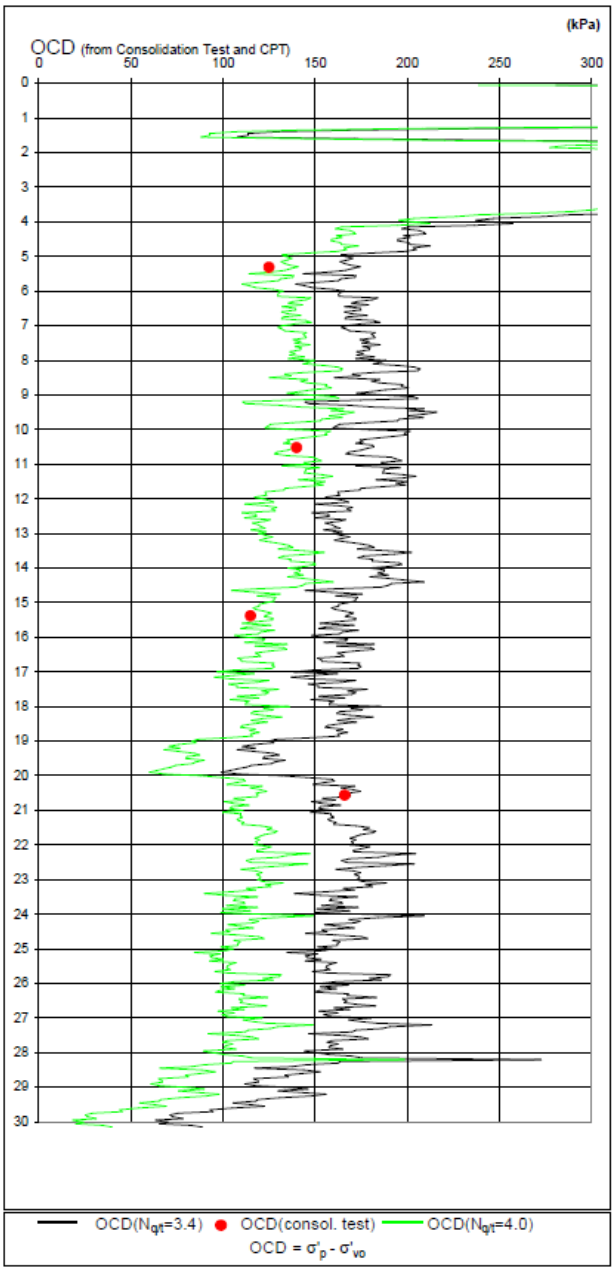


- South West – 50 kPa to 100 kPa, increasing trend moving towards Fraser River
- South Approach – 100 kPa to 200 kPa
- North Approach – 200 kPa to 300 kPa
- North of CPR – 200 kPa to < 50 kPa, decreasing trend moving to north and east

**Fig. 7.** Interpreted OCD from CPT04-50, $N_{qt}$ of 3.4 (blue) and 4.0 (green).

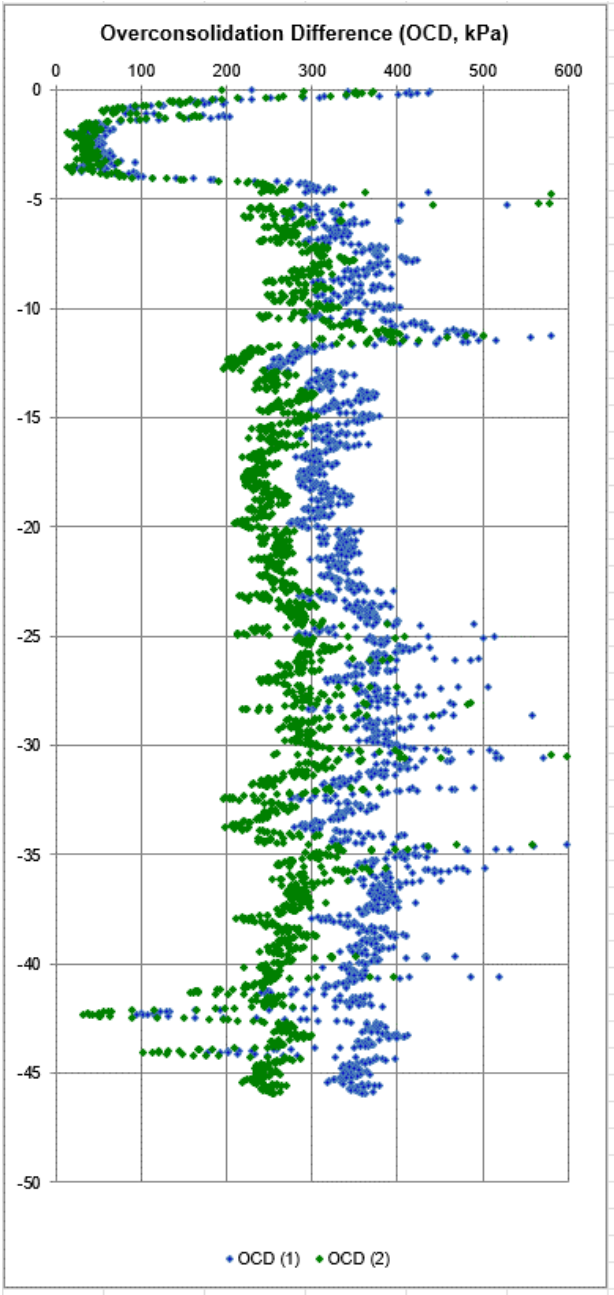


## Significance of OCD Pattern

The typical OCD profile observed in the Fraser River Delta and the Serpentine and Nicomekl lowlands is an over-consolidated crust at the surface which

trends towards normally consolidated conditions with depth (i.e., OCD = 0 kPa). The over-consolidated crust is formed by aging and desiccation and does not extend much below the long-term average groundwater level. A deltaic environment also favours normally consolidated conditions as new soil is being deposited.

Buried over-consolidated crusts can be found on the margins of the Serpentine and Nicomekl lowlands and are evidence of the valley topography when the relative sea level was about 25 m to 12 m lower than it is today between 13 kYa and 8 kYa (James et al. 2009, and William & Roberts 1989). The normally consolidated deposits overlying the crust having been deposited during marine transgression as sea level rose.

Constant over-consolidation with depth is interpreted as the erosion of overlying material which results in the magnitude of over-consolidation observed. For example

[1] 100 kPa OCD = 5.5 m of erosion at $\gamma$ = 18 kN/m$^3$
[2] 100 kPa OCD = 12.5 m of erosion at $\gamma$' = 8 kN/m$^3$

A similar situation occurs when a preload is removed. This is illustrated in Figure 8 which shows the interpreted OCD for two CPTs completed as part of the Highway 91/17 Upgrade Project in Delta, B.C. CPT20-72 was located within the footprint of a sand stockpile used for construction of Highway 91 in the 1980s. CPT20-98 was located outside of the sand stockpile. Both CPTs show a crust (i.e., higher near surface OCD), but the deeper OCD pattern of CPT20-72 suggests the removal of more than 6 m of fill, which was the old stockpile

**Fig. 8.** Comparison of OCD of two CPTs.

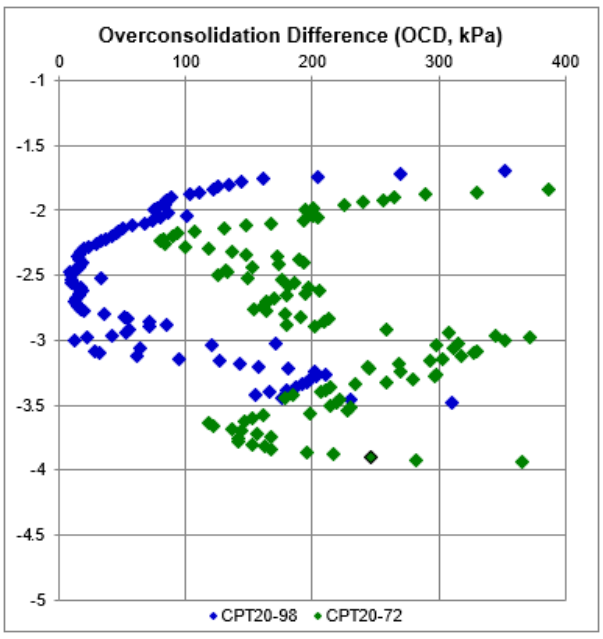


## Golden Ears Bridge Interpretation

The unusual OCD patterns observed along the Golden Ears Bridge alignment are interpreted to be the result of massive erosion caused by the glacial Lake Fraser outburst flood. When the flood occurred roughly 11,000 years ago the active front of the delta was likely a short distance downstream of Golden Ears Bridge with what is now Pitt Lake being a fjord and much of Pitt Meadows being the sea (Clague et al. 1983). The outburst flood likely played a significant role in filling this basin which allowed the delta to start expanding west of New Westminster 10,000 years ago.

Figure 9 provides an annotated LiDAR map identifying significant topographic features in the vicinity of Golden Ears Bridge. Sea level at the time of the flood was roughly 25 ± 10 m lower than at present (James et al. 2009). This would imply a flood height of more than 40 m based on the difference between the 11 kYa sea level and the tops of the scour ridges.

Figure 10 provides an annotated LiDAR map with the inferred erosion along the Golden Ears Bridge alignment. For simplicity, the magnitude of erosion was calculated using a unit weight of 18 kN/m$^3$. The actual depth of erosion could be much greater than is implied in Figure 10. This is because the depth to the high OCD deposits are variable along the alignment, from 25 m to 35 m deep at the river banks to about 5 m deep far away from the river. Thus, the total magnitude of erosion could vary from 35 m to 40 m at the river banks to slightly more than the amount indicated in Figure 10.

There is evidence that flood induced erosion occurred along the south bank for at least 6 km downstream of the bridge. Consolidation tests performed by Trow (now exp) in 2009 as part of TetraTech's (then EBA) design work for South Fraser Perimeter Road identified over-consolidated marine clay-silts at a site where 8.5 m of mineral fill had been placed almost 20 years earlier. The 6 consolidation tests at that location had a lower-bound OCD of about 75 kPa, or 130 kPa if the weight of the fill accounted for. This implies about 7 m of erosion occurred using a unit weight of 18 kN/m$^3$.

The marine clay-silt at the downstream site was highly compressible (i.e., 1.2 < Cc < 2.7, LL < w%) with a well-defined break in the consolidation curve which provided a high degree of confidence in the estimation of pre-consolidation pressure. Figure 11 illustrates the characteristic shape of the e-log s curve for this series of tests. The sharp break is interpreted as evidence of structure arising from marine deposition and subsequent replacement of saline pore water with fresh water. The consolidation tests at GEB did not exhibit such sharp breaks in the e-log $\sigma$ curve which suggests a more brackish depositional environment.

**Fig. 9.** Annotated LiDAR map identifying significant topographic features in the vicinity of GEB.

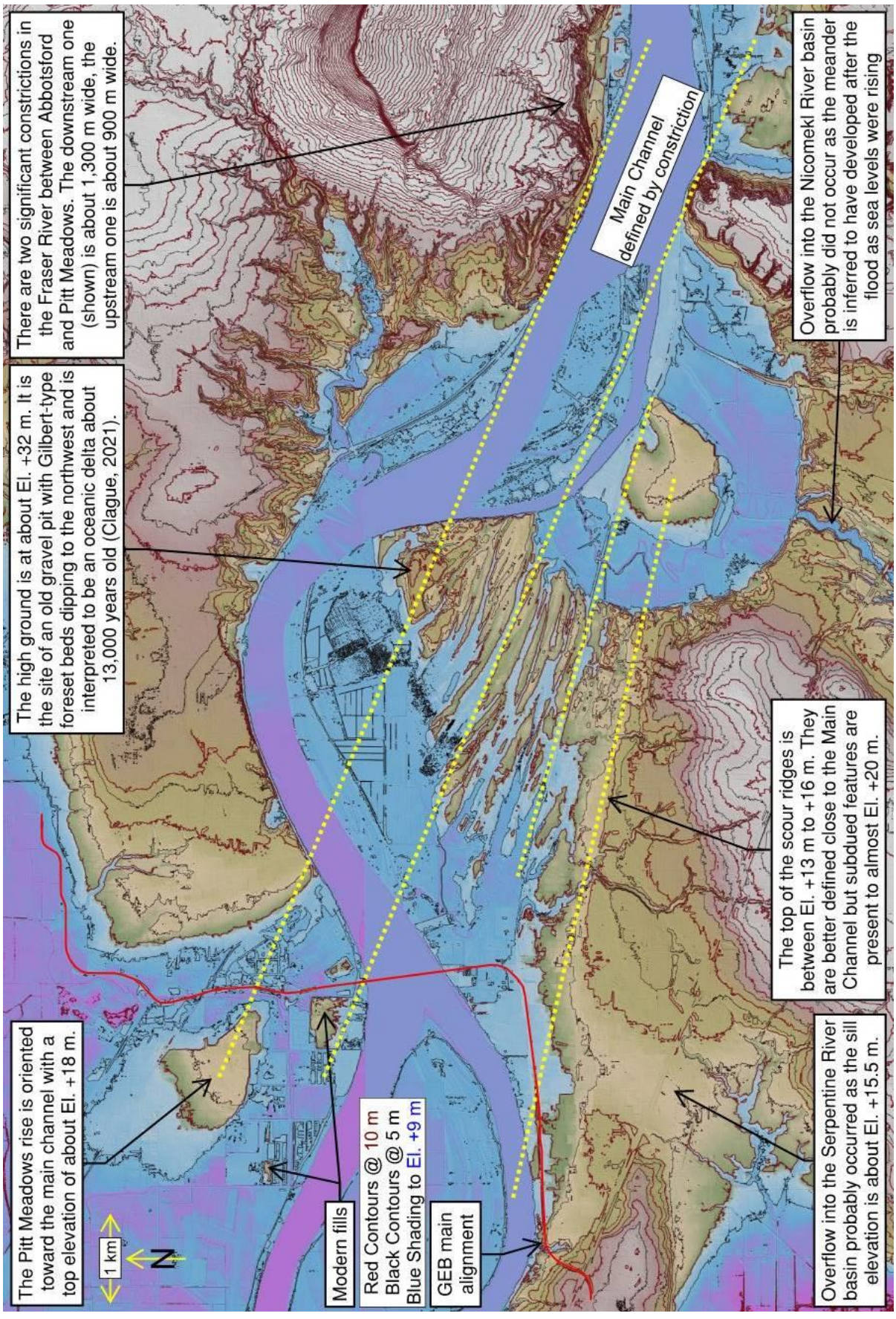

**Fig. 10.** Annotated LiDAR map with inferred erosion along GEB alignment.

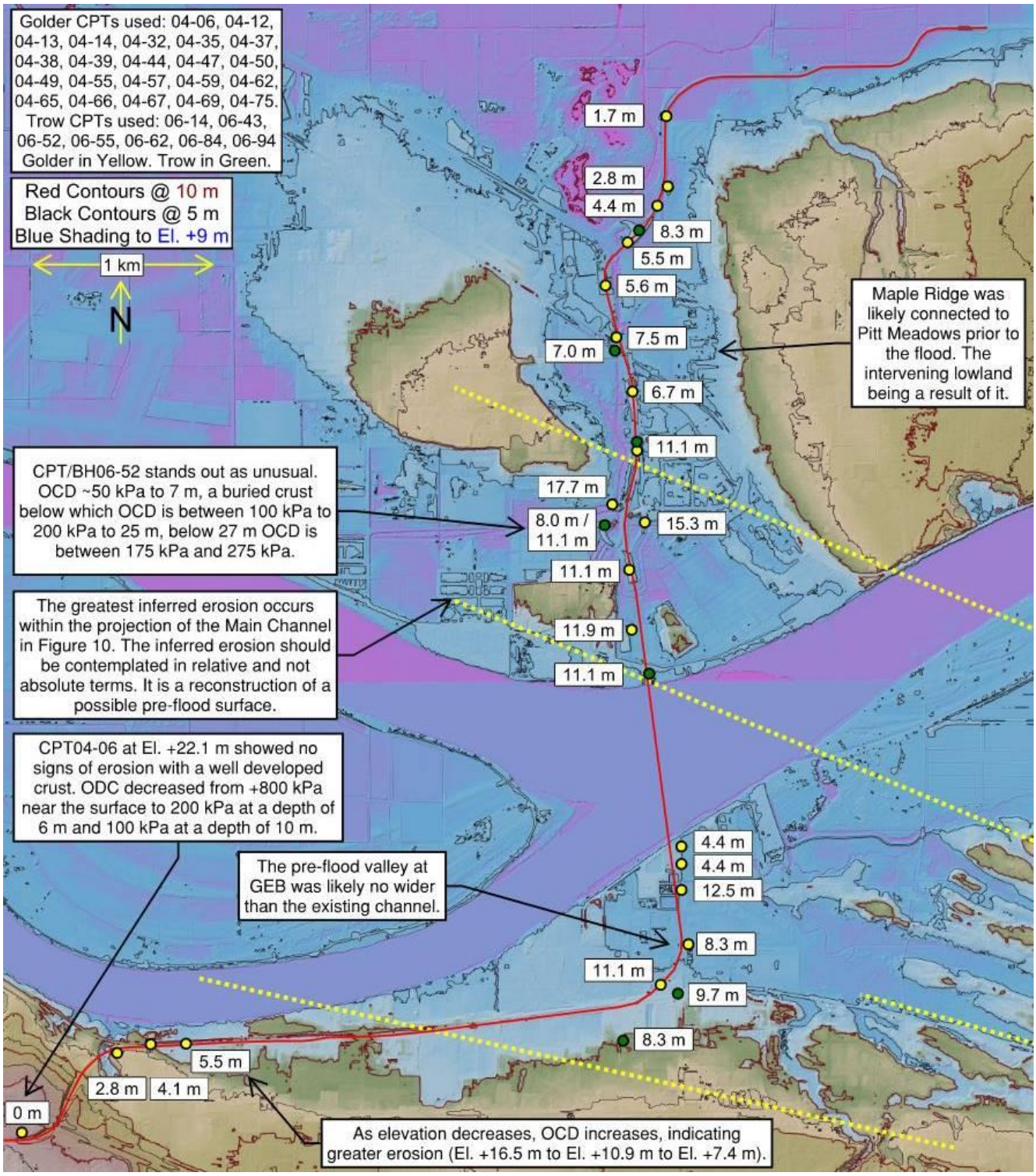

**Fig. 11.** Consolidation test at site 6 km downstream of Golden Ears Bridge (near 173rd Street, Surrey).

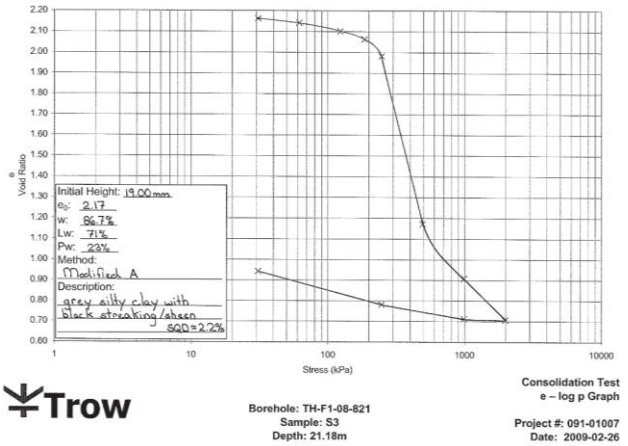


## Final Thoughts

Manifestations of the glacial outburst flood are likely present throughout much of the Fraser Valley. However, they may not be recognised as such because an outburst flood is not part of the common narrative that resides within the minds of most local geo-practitioners. The same can be said for the relative rise in sea level between 11 kYa and 5 kYa. Raising awareness of the dynamism at the end of the glaciation and its relevance for geotechnical interpretation is important.

As a thought experiment, the change in sea level over the past 15,000 years should have left a detectable imprint on the interpreted OCD with depth. However, that imprint is not apparent in any of the CPTs reviewed except for CPT04-42, and it is far deeper than it should be. It may be that the though experiment is too simple in that it ignores the possibility of unusual groundwater regimes at the end of the ice age and that the entire thickness of clay-silts are consolidating as they are being raised above sea level.

The OCD pattern typical of Golden Ears Bridge should eventually disappear moving downstream to the west. With enough CPTs and consolidation tests it may be possible to determine the limits of erosion, downstream of which would have been a depositional environment

## Acknowledgements

We thank Brent Case of the BC Ministry of Transportation and Infrastructure, Ujjal Chakraborty and Armando Abello of exp Services Inc. for the factual information from the GEB project, and Chris Longley and Patrick Korner of TetraTech for CPT data from the South Fraser Perimeter Road Project. Particular thanks are given to the late Graeme Macleod (1930-2020) for involving the author in the GEB project at the start of the investigation for detailed design, and the many consolidation tests that followed.

LiDAR topographic maps were prepared by the author using information obtained from the BC LiDAR Data Portal.

2-sigma age range for $^{14}C$ dates determined using CALIB 8.1.0 program.

## References

Blais-Stevens, A., Clague, J.J., Mathewes, R.W., Hebda, R.J., Bornhold, B.D. 2003, Record of a large, Late Pleistocene outburst floods preserved in Saanich Inlet sediments, Vancouver Island, Canada, *Quaternary Science Reviews*, 22:2003, 2327-2334

Clague, J.J., 2021, Evidence for Fraser River Megafloods, Ice Age Floods Institute Puget Lobe, YouTube, https://www.youtube.com/watch?v=uO87BoTuKHw

Clague, J.J., Luternauer, J.L., Hebda, R.J. 1983, Sedimentary environments and postglacial history of the Fraser Delta and lower Fraser Valley, British Columbia, *Canadian Journal of Earth Science*, 20: 1314-1326

Clague, J.J., Roberts, N.J., Miller, B., Menounos, B., Goehring, B. 2021. A huge flood in the Fraser River valley, British Columbia, near the Pleistocene Termination, *Geomorphology*, 347:107473

Golder Associates (now WSP) September 2004, *Report on Geotechnical Investigations for The Golden Ears Bridge Project (2 Vol.)*

Hebda, R.J., 1977, *The Paleoecology of a raised bog and associated deltaic sediments of the Fraser River delta*, University of British Columbia, Ph.D. Thesis

Ladd, C.C. and DeGroot, D.J. 2003, Recommended Practice for Soft Ground Site Characterization: Arthur Casagrande Lecture (revised May 2004), *12th Panamerican Conference on Soil Mechanics and Geotechnical Engineering*, Cambridge, MA, USA

Kovanen, D.J., Haugerud, R.A., Easterbrook. D.J. 2020. *Geomorphic Map of Western Whatcom County, Washington (Version 1.1, November 2021)*, U.S. Geological Survey Scientific Investigations Map and Pamphlet

Thomas, J., Gowan, E.J., Hutchinson, I., Clague, J.J., Varrie, J.V., Conway, K.W. 2009, Sea-level change and paleogeographic reconstruction, southern Vancouver Island, British Columbia, Canada, *Quaternary Science Reviews*, 28:2009, 1200-1216

Trow Associates Inc. (now exp Services Inc.) June 2007, *Golden Ears Bridge Factual Report (Rev.6)*

William, H.F.L. and Roberts, M.C. 1989, Holocene sea-level change and delta growth: Fraser River delta, British Columbia, *Canadian Journal of Earth Science*, 26: 1657-1666

# Top-Down excavation system, an integral solution for challenging deep excavation projects with complex surroundings and difficult geotechnical conditions.

Omar Rodriguez, M.Sc.
Design Engineer, Soletanche Bachy Canada, Vancouver, BC.

Alexandre Beauvilain, M.Sc.
Vice President, Soletanche Bachy Canada, Vancouver, BC.

**ABSTRACT** Edification projects in Vancouver are each time more complex and challenging. A clear example is the construction of high rises in relatively small surfaces that require a considerable amount of basement levels, reaching substantial excavation depths. In addition, these projects may have sensitive surroundings such as tunnels from the metro system and buildings with a significant number of basement levels. To make these types of projects a reality, this article presents an integral solution where the earth retention system is accomplished by means of a diaphragm wall. Whereas the excavation is achieved by implementing the Top-Down system, so that the basement slabs are the elements that react against the lateral earth pressure, eliminating the need for any other type of additional shoring or anchoring. Moreover, the deep foundation consists of large diameter circular or rectangular piles supported in the competent material. The article highlights the analysis and design of diaphragm walls, referencing the validation against data obtained from inclinometer measurements. It also discusses the construction aspects of this solution and suggests its feasibility for Metro Vancouver. Furthermore, it presents a selection of relevant case studies where the Top-Down excavation system has been successful.

## Basic Principles

### Definition

The Top-Down excavation system is a solution that successfully integrates the earth retention, deep foundation, and excavation works.

This approach incorporates a watertight definitive structural element as the earth retention system, i.e., a diaphragm wall, also known as D-Wall. Eliminating the need for an additional basement wall constructed in front of the temporary earth retention works. Furthermore, the basement slabs are the elements that react against the lateral earth pressure, eliminating the need for additional shoring or anchoring. Whereas the deep foundation elements are leveraged to embed vertical beams that will support the basement slabs. Once the final excavation level is reached, the deep foundation and the entire basement for underground parking have been built. In addition, it may be possible to simultaneously build a portion of the superstructure.

### Applicability

Challenging deep excavation projects with complex surroundings and difficult geotechnical conditions are becoming the norm. Large cities continue to expand, and property is becoming scarce. To maximize land use, high-rise buildings are preferred. These require deep foundations and tend towards increasingly deeper basements. Experience with this specialized technique has shown an average of 6 basement levels. However, there have been projects with 8, 10, 12, and up to 16 basement levels for underground parking where the Top-Down excavation system proved to be an efficient and effective solution.

Some of the most common challenges that designers and contractors face in such projects are:

- Complex footprint geometry and limited surface
- Deep and sensitive neighbouring structures
- Nearby utilities, e.g., electrical, and gas
- Tunnels from the metro or sewer systems
- High water table
- Soft soils, e.g., expansive clay and organic soil

## Analysis and design

### Earth retention

One of the most common earth retaining structures used for the Top-Down excavation system is the diaphragm wall or D-Wall, Chadeisson (1961). This is a watertight and definitive cast-in-place reinforced concrete structure, built with very strict verticality, and drilling mud control. Meeting the design criteria specified by EN1997-1 (2004) and EN1998-5 (2004).

The site-specific geotechnical and piezometric conditions are considered within a D-Wall's corresponding soil-structure interaction analysis. This analysis is performed using the Reaction Modulus method or Finite Element method. In practice, Soletanche Bachy performs soil-structure interaction analysis using their proprietary software PARIS®. This tool can analyze a D-Wall's stress and

deformation state throughout its multiple construction stages. In addition, it supports pseudo-static analysis based on the Mononobe-Okabe method, interpreted by Seed and Whitman (1970). The software represents soil-structure interaction using the elastoplastic behaviour of the soils, captured by the horizontal reaction modulus as illustrated in Fig. 1 and further discussed by Schmitt (1995).

**Fig. 1.** Stress and deformation behaviour considered in the analysis model for the Reaction Modulus method.

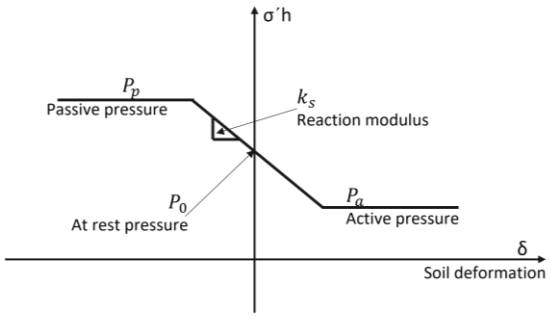


The software performs plane strain analysis, as depicted in Fig. 2. A major advantage is that the software can provide output for each construction stage. It provides active and passive earth pressures, as discussed by Dodel et al. (2002). In addition, it outputs horizontal deformation, as well as shear force and bending moment diagrams, as shown in Fig. 3. This is essential information to guarantee a tailor-made and economical structural design for the D-Wall, without overestimating these magnitudes.

**Fig. 2.** Reaction modulus analysis model in Soletanche Bachy's proprietary software PARIS®.

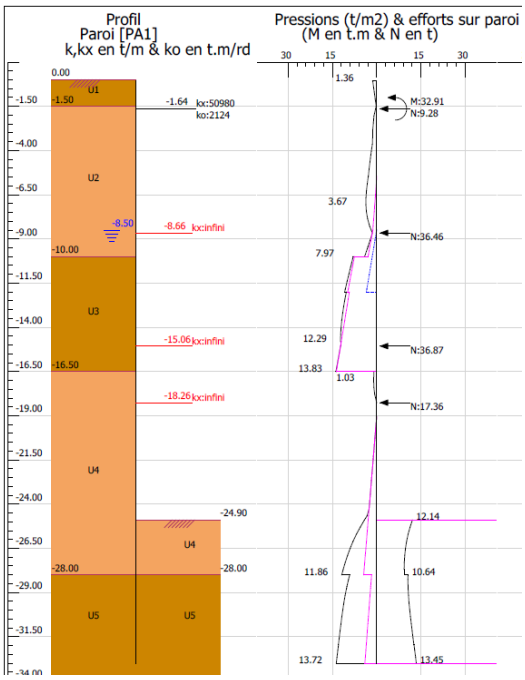


On the other hand, there are projects where difficult geotechnical conditions may require analysis models using the finite element method which can capture complex soil behaviour, and where it is possible to introduce dynamic analysis through constitutive soil models under cyclic loading. For instance, Fig. 4 shows the deformation contours and mesh of a Top-Down excavation analysis model performed in the finite element software Plaxis 2D.

**Fig. 3.** Envelopes of horizontal deformation, shear force, and bending moment diagrams, PARIS® output.

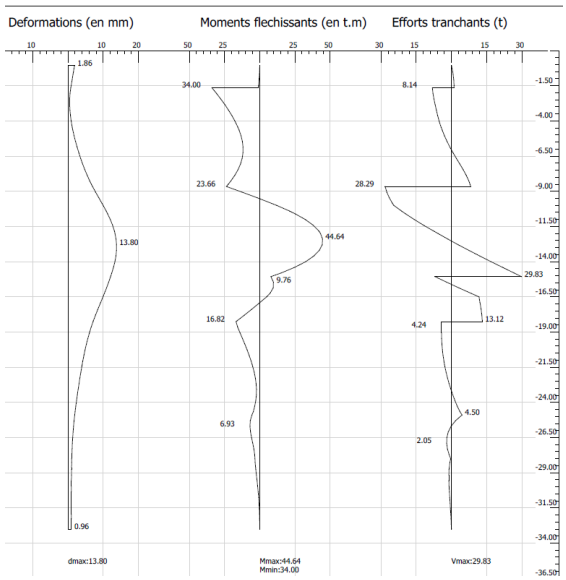


**Fig. 4.** Deformation contours of a Top-Down excavation, from a finite element method analysis model in Plaxis 2D.

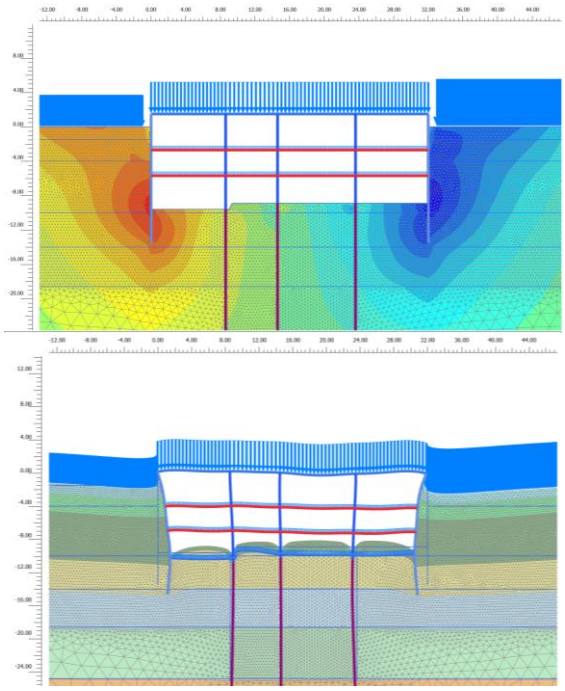

Results from both the reaction modulus and finite element method models have been validated against real data obtained from instrumentation and monitoring, Gutjahr et al. (2003). This is illustrated in Fig. 5, which shows the horizontal deformations of a D-Wall during a Top-Down excavation, Rodriguez et al. (2022). Note that these observations are recorded during all excavation stages and compared against the theoretical deformation obtained from the analysis models. This is valuable information to calibrate values of both reaction and elastic modulus.

**Fig. 5.** Horizontal deformations in a D-Wall for a Top-Down excavation, from inclinometer data.

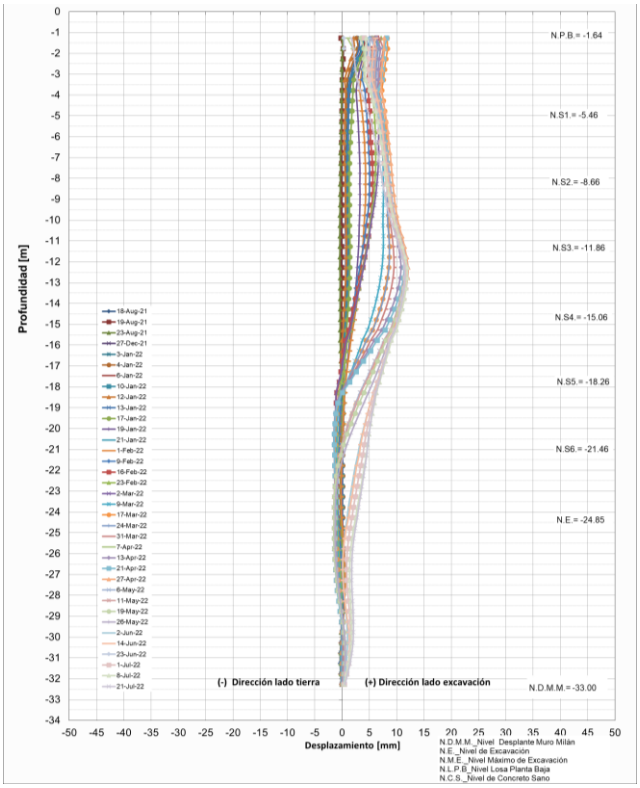


Moreover, considering that current practice for the design of basement walls in Vancouver is conservative, as suggested by Amirzehni, E. et al. (2015 and 2018), and that a D-Wall is a more robust structural element compared to a standard reinforced concrete basement wall. Therefore, the Top-Down excavation system alongside a D-Wall represents an attractive and feasible alternative.

## Slabs

As previously stated, the basement slabs are the elements that will react against the lateral earth pressure, eliminating the need for additional shoring or anchoring on the D-Wall. These slabs are commonly analysed in structural analysis software, as depicted in Fig. 6, where the excavation shafts are also visible. With these models, it is possible to obtain deformations, bending moments, shear, and stress distribution, which are all required for design.

It is important to note that the working platform during the Top-Down excavation will be one of the definitive slabs. Furthermore, it will be subjected to temporary loading that in most cases is higher than the service loading for the slab and thus should be considered in its design. Meanwhile, the rest of the basement slabs should be analysed and designed according to their respective service loads.

**Fig. 6.** Stress distribution in basement slab.

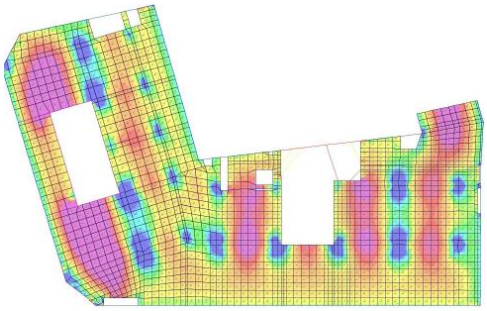

The bottom slab plays an equally important role in this excavation system. This slab needs to be designed to distribute all the stresses that reach the base of the excavation while also resisting any possible water pressure. Likewise, it should be designed considering soil-structure interaction in both static and dynamic conditions.

## Vertical beams

Another essential component for the Top-Down excavation system is the vertical beams or plunge columns that will support the working platform and the rest of the slabs that are built as the excavation advances. The vertical beams, shown in Fig. 7, are pre-embedded within the deep foundation elements. These sections are designed for buckling and require mechanical and welded connections accordingly.

**Fig. 7.** Vertical beams pre-embedded in deep foundation.

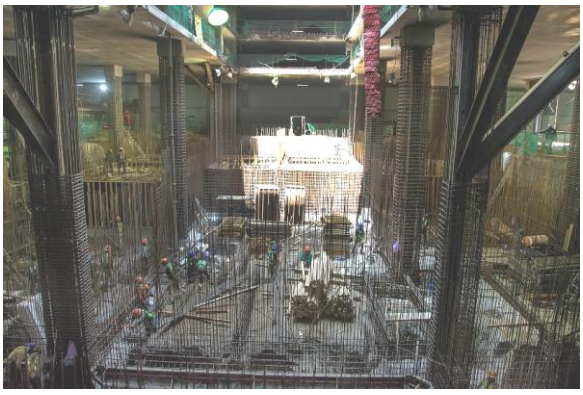

With each excavation stage, the vertical beams are uncovered and the node that connects them with the slab can be built. This node, commonly referred to as stump and depicted in Fig. 8, also serves to prevent punching shear failure. Therefore, the plunge columns along with the stumps constitute the load transfer mechanism from the slabs to the foundation. In addition, the definitive columns can potentially be built as the excavation progresses, as seen in Fig. 9.

**Fig. 8.** Vertical beams and stumps for load transfer.

**Fig. 9.** Definitive columns built while excavating.

## Foundation

The deep foundation elements are regularly large diameter piles or barrettes. These are designed considering the loads from the structure in its various combinations for the static and dynamic conditions, as well as the corresponding load factors.

The bearing capacity should meet local codes and guidelines. Similarly, it is crucial to account for the vertical deviation during the construction of these elements. The structural design of the deep foundation should consider axial compression resistance, minimum or tension reinforcing, and the possibility of flexural compression, as depicted in the interaction diagram in Fig. 10.

Finally, in terms of quality assurance, it is advised to perform pile integrity testing in accordance with the requirements of local practice and codes.

**Fig. 10.** Interaction diagram of a deep foundation element.

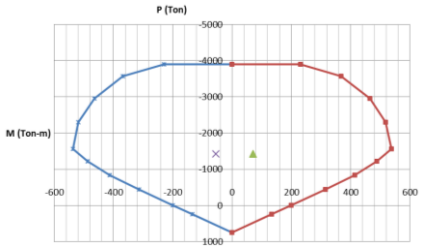


# Construction

## Diaphragm Wall

A D-Wall is an impervious reinforced concrete wall cast in panels. To build a D-Wall, guide walls are necessary. These serve as alignment, as guide for the excavation tool, and to support the reinforcing cages. The required equipment to build a D-Wall is illustrated in Fig. 11. Namely an excavation tool such as a mechanic grab, hydraulic grab, or hydro-fraise. In addition to a desander, a service crane, a tremie rack, return pumps, drilling mud silos, and a mud central. The standard thicknesses for D-Walls are 0.5, 0.6, 0.8, 1.0, 1.2, 1.5, and 1.8 m. Furthermore, Fig. 12 illustrates a hydraulic grab excavating a diaphragm wall panel.

**Fig. 11.** Common equipment for D-Wall construction.

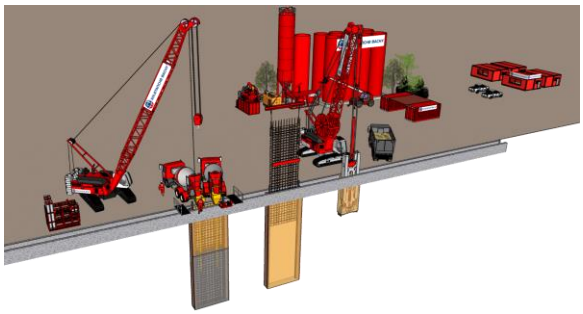

**Fig. 12.** Hydraulic grab excavating a D-Wall panel.

## Panel joint

The water tightness between panel joints is achieved with a patented CWS formwork. In essence, a temporary steel stop end that allows the installation of a PVC or Neoprene water stop along the entire panel joint, as seen in Fig. 13. Furthermore, this formwork guarantees the contact between adjacent panels, thus forming a continuous concrete wall.

**Fig. 13.** CWS formwork for D-Wall panel joints.

## Verticality

Verticality control is rigorous and continuous for each diaphragm wall panel. D-Walls can be excavated with mechanical and hydraulic grabs, as well as with a hydro-fraise. Mechanical grabs were the first tool used for D-Wall excavation. Hydraulic grabs, on the other hand, benefit from its power and versatility in harder soils, allowing for higher productivity. Whereas the hydro-fraise can excavate harder soils due to its two counter-rotating drums with cutting teeth. In practice, the most used excavating tool is the hydraulic grab shown in Fig. 14.

With these tools, the tolerance of vertical deviation can range between 0.8% to 1%. In Fig. 15, the verticality controls available to the hydraulic grab operator are shown. In addition, real-time measurements of the alignment are monitored, and corrective action can be taken at any time during excavation. As a precautionary measure, the vertical accuracy of a panel can also be diagnosed and verified with an ultrasonic echo sensing system test.

**Fig. 14.** Hydraulic grab for diaphragm wall excavation.

**Fig. 15.** Verticality controls available to the grab operator.

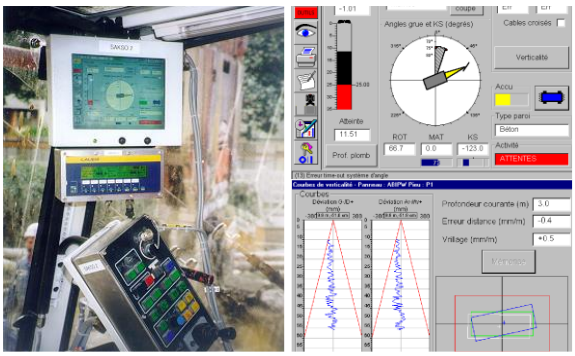

## Drilling fluid

One of the keys to the D-Wall technique lies in the stability of the walls during its excavation. This is achieved by using polymer or bentonite mud as drilling fluid, a material made on-site, regenerated, and de-sanded in one or more mud centrals. It is essential to constantly safeguard the quality of the drilling fluid on-site and throughout the various construction stages of a D-Wall, Fig. 16 shows drilling fluid control at an on-site mud central.

The drilling fluid maintains the stability of the excavation walls. As a reference, Table 1 displays a set of characteristic parameters for bentonite mud, differentiating between mud in its new state and mud before concreting a D-Wall panel.

**Table. 1.** Sample bentonite mud characteristics, for new mud and mud before concreting a D-Wall panel.

| Parameter | New mud | Before concreting |
|---|---|---|
| Marsh viscosity (s) | 33-40 | 33-50 |
| Density | 1.02-1.05 | <1.15 |
| Cake (mm) | <1 | <3 |
| PH | 7-10 | 7-11 |
| Sand content (%) | 0 | <3 |

**Fig. 16.** Drilling fluid control at on-site mud central.

## Concrete

To guarantee the quality of the D-Wall, a special concrete mix designed specifically for diaphragm walls must be used. Similarly, concrete quality control is fundamental. Although D-Walls are built with structural concrete with a compressive strength varying from 30 to 40 MPa, they require a special concrete mix. This mix must be self-compacting and have a particular slump and placement time to guarantee its workability characteristics during panel concreting. Furthermore, concreting of a D-Wall must always be continuous and performed using one or more tremie pipes which are kept within the fresh concrete to avoid cold joints as the concrete rises.

## Capping beam

Another fundamental and often overlooked element of a D-Wall is the capping beam. This continuous element ties all the panels together along the entire alignment. Its main purpose is to homogenize the displacements and forces at the top of the D-Wall. Moreover, considering that the maximum shear force under static or seismic conditions will occur at the ground-level interface, the depth of the beam and reinforcing can be designed to resist these forces in service conditions. See Fig. 17 and Fig. 18, which illustrate the geometry, size, and reinforcing that the capping beam for a diaphragm wall can have.

**Fig. 17.** Geometry and size of a D-Wall capping beam.

**Fig. 18.** Size and reinforcing of a D-Wall capping beam.

## Working platform slab

The working platform slab is paramount for the Top-Down excavation system. As previously mentioned, this slab is definitive and will need to resist heavy loading from cranes, trucks, concrete mixers, construction materials, and all the equipment that may be required. See Fig. 19, which illustrates the use and common loading on the working platform slab, and where the excavation shaft is also visible.

**Fig. 19.** Working platform slab for Top-Down.

# Successful projects

## Project in actively seismic region

The Top-Down excavation system was implemented for a 50-story 235 m tall high-rise building located in Mexico City. The project has a 1 m thick D-Wall with a tip elevation at -55 m, a deep foundation at a depth of -64 m, and civil works for 7 basements with under slab excavation to a maximum depth of 25 m. The D-Wall capping beam, working platform slab, under-slab civil works, and simultaneous superstructure, are shown in Fig. 20, Fig. 21, Fig. 22, and Fig. 23, respectively. It should be noted that the maximum recorded Peak Ground Acceleration (PGA) after the inauguration of the project in 2016 has been 101, 314, and 305 cm/s2 in the NS, EW, and Z components, respectively, Lermo et al. (2020), which is approximately 0.10, 0.32, and 0.31 g.

**Fig. 20.** D-Wall capping beam.

**Fig. 21.** Working platform slab.

**Fig. 22.** Civil works and under slab excavation.

**Fig. 23.** Simultaneous construction of superstructure.

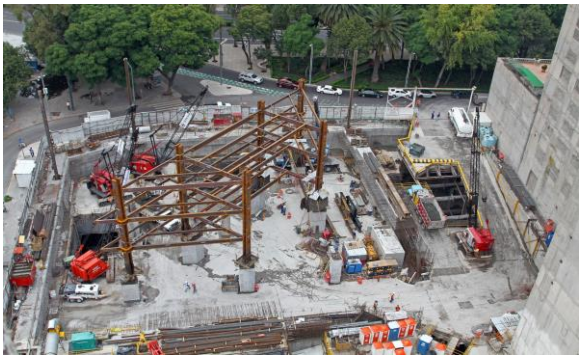

## Project with complex surroundings

Another successful application in the same highly active seismic region was for two 30-story towers, with 6 and 8 basement levels, reaching 25 m and 33 m of depth, see Fig. 24 and Fig. 25 for pictures from the 8-basement excavation. These two deep excavations were performed simultaneously, being separated by a building in operation. To add to the complex urban environment, the projects are surrounded by a tunnel from the metro system and 2 high-rise buildings with 4 and 8 basements. The metro line alignment had drastic implications for the 6-basement excavation, forcing a reduction of the parkade surface from levels 4 to 6, and implicating an interior D-Wall, as seen in the elevation shown in Fig. 26. In both excavations, the earth retaining system is a 0.6 m thick D-Wall with tip elevations ranging from -27 m to -40 m. Meanwhile, the deep foundations are cast-in-place piles of 1 m to 2 m in diameter with tip elevations ranging between -33 m to -46 m within the cemented and compact tuff material. Although this solution guaranteed a negligible urban impact, it did require continuous collaboration among all disciplines.

**Fig. 24.** Working platform slab and excavation shafts.

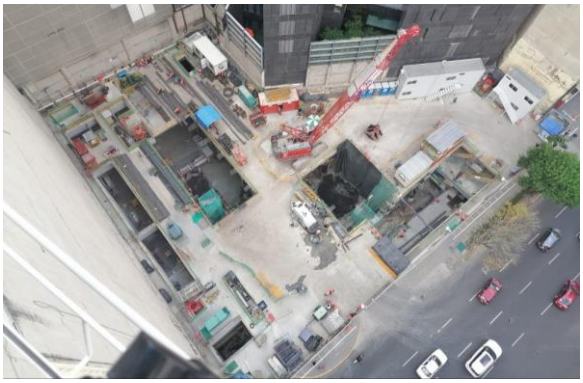

**Fig. 25.** Top-Down excavation works for 8 basements.

**Fig. 26.** Reduction of parkade surface due to metro line.

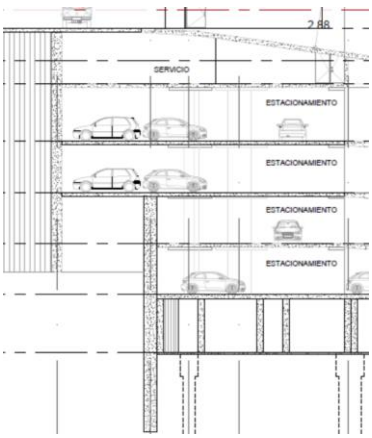

## Large urban excavation

Similarly, this solution has been applied to a project in New York City where the site covered two city blocks, see Fig. 27. In this case, the property line constraints and a rail line did not allow for a conventional open pit excavation with tiebacks. The major benefit of the Top-Down was the ability to progress with the 6-story high-rise superstructure construction while the basements reaching a depth of 18 m were excavated and built at the same time. Overall, this resulted in significant time and cost savings. In this project, the structural and watertight D-Wall had tip elevations ranging between -30.5 m and -45.7 m. While the deep foundation had a total of 96 piles ranging between 1.8 m to 2.1 m diameter, and tip elevations ranging from -37 m to -84 m. Note that the D-Wall and Pile works were simultaneously performed, as shown in Fig. 28. During these works, difficult drilling conditions were reported due to the encounter of boulders and cobbles, which affected productivity. In addition, the removal of debris and contaminated soil was an additional challenge during under-slab excavation, as seen in Fig. 29.

**Fig. 27.** Plan view of large urban excavation.

**Fig. 28.** D-Wall and Pile works for Top-Down.

**Fig. 29.** Under slab Top-Down excavation.

## Top-Down projects worldwide

Worldwide, Soletanche Bachy and its subsidiaries have implemented the Top-Down excavation system for purposes of deep excavations for basements and underground parking garages, as well as for large cut and cover projects, at least once or multiple times in the following countries: Chile, Colombia, France, Mexico, Monaco, New Zealand, Poland, Singapore, Spain, USA, and Vietnam. Whereas other D-Walls have been successfully built in Australia, Hong Kong, Malaysia, UAE, and throughout Europe.

# Conclusions

This paper presented an overview of the Top-Down excavation system, a robust solution that successfully integrates earth retention, deep foundation, and excavation works. Furthermore, it described its application in complex surroundings and difficult geotechnical conditions to overcome the challenges owners, designers, and contractors face in these intricate projects.

Consequently, this system effectively reduces urban impact and delivers a safe alternative to open-pit excavations. In addition, it can potentially reduce construction time because the excavation and basement slabs are built simultaneously. Moreover, it may also be possible to build a portion of the superstructure at the same time. Additionally, the earth retention, provided by a D-Wall is a watertight definitive structure that can have a dual purpose as both a bearing and retaining element.

Similarly, the document provided a high-level description of the analysis and design for the main components of this solution, i.e., earth retention, slabs, vertical beams, and foundation elements. Likewise, the most important construction aspects related to the D-Wall, panel joint, drilling mud, verticality, concrete, and capping beam were discussed. Finally, a brief and limited selection of successful Top-Down projects has been presented.

## References


Amirzehni, E. et al. (2015). Seismic performance of deep basement walls. 6th International Conference on Earthquake Geotechnical Engineering, Christchurch, New Zealand.

Amirzehni, E. et al. (2018). Recommendations for the seismic design of deep basement walls. Eleventh U.S. National Conference on Earthquake Engineering, Los Angeles, California.

Chadeisson, R. (1961). Parois continues moulees dans le sols. Proceedings of the 5th European Conference on Soil Mechanics and Foundation Engineering, Vol. 2., Paris, pp. 563-568.

Dodel E., Schmitt P., Simon G. (2002). Active and passive earth pressure: A new approach for an old concept, Soletanche-Bachy, Paris. Fifth European Conference on Numerical Methods in Geotechnical Engineering, NUMGE 2002, September 4-6, 2002, Paris, France.

EN1997-1 (2004) Eurocode 7: Geotechnical design - Part 1: General rules. European Committee for Standardization.

EN1998-5 (2004) Eurocode 8: Design of structures for earthquake resistance - Part 5: Foundations, retaining structures and geotechnical aspects. European Committee for Standardization.

Gutjahr I., et al. (2003). Instrumentation of the diaphragm wall of the Blanc-Mesnil Basin: retro-analysis and calibration of calculation models, Soletanche, Revue Française de Géotechnique, 2e trimestre.

Lermo J. et al. (2020). Actualización de la zonificación sísmica de la ciudad de México y áreas aledañas-parte norte. Instituto de Ingenieria, Universidad Nacional Autónoma de México.

Rodriguez, O. et al. (2022). Design and simultaneous construction of 2 nearby deep excavations for 6 and 8 basements, by means of the Top-Down system, in the transition zone of Mexico City. XXXI Reunion Nacional de Ingenieria Geotecnica, Guadalajara, Jal., Mexico.

Schmitt P. (1995). Méthode empirique d'évaluation du coefficient de réaction du sol vis-à-vis des ouvrages de soutènement souples, Soletanche, Revue Française de Géotechnique, 2e trimestre.

Seed, H.B., and Whitman, R. (1970). Design of earth retaining structures for dynamic loads. In Proceedings of the ASCE Specialty Conference on Lateral Stresses in the Ground and Design of Earth Retaining Structures, Cornell University, Ithaca, N.Y. ASCE. Vol. 1, pp. 103–147.

# Repair of the Sumas River Dike Breach: A Case History

Brian L.J. Mylleville, Ph.D., P.Eng.
Senior Geotechnical Engineer, Kontur Geotechnical Consultants Inc.

Brian Wilson, B.Sc., P.Eng.
Vice President, Keller – North America

Colin Kristiansen, M.B.A., P.Eng.
Kerr Wood Leidal Associates Ltd.

**ABSTRACT** In November 2021, during an unprecedented atmospheric river event, the Sumas River Dike was breached resulting in flooding of a large area of the Sumas Prairie in Abbotsford, BC. The site of the Sumas River Dike breach is approximately 4.5 km southwest (upstream) of the Barrowtown Pump Station along the base of Sumas Mountain. This paper describes the main breach that occurred including the failure mechanism and the key geotechnical engineering considerations related to design and construction of the breach repair. A two-staged strategy was adopted for repair of the dike breach that included the initial emergency repair to close the breach followed by the additional remedial work required to restore the temporarily repaired dike section back to a dike with a low permeability core . Details of the two-stage repair strategy are described including the various options considered, as well as the challenges faced during construction. The flood event also created significant challenges during construction in terms of the supply of the materials required to repair the breach, access to these materials, and maintenance of access between the work site and material supply. These challenges are presented with the intent of providing some insights for future emergency preparedness planning.

## Introduction

On November 16, 2021, during a series of unprecedented atmospheric river events, the Sumas River Dike (also referred to as the Upper Sumas River Dike) was breached resulting in flooding of a large area of the Sumas Prairie in Abbotsford, BC. Emergency response focused on closing the breach to stop flowing water from the Sumas River entering Sumas Prairie. The widespread flood event created significant challenges in terms of site access and material supply during the emergency response.

This paper describes the main breach that occurred including the failure mechanism and the key geotechnical engineering considerations related to design and construction of the breach repair. A two-staged strategy was adopted for repair of the dike breach that included the initial emergency works to close the breach followed by the additional remedial work required to re-establish a low permeability core within the temporarily repaired dike section. Details of the two-staged repair strategy including the options considered for the low permeability core are discussed in this paper. Several challenges that had to be overcome during construction are described with the intent of providing some insights for consideration on similar projects as well as for future emergency preparedness planning.

## Site Location and Description

The reach of the Sumas River that flows north of the Trans-Canada Highway (Highway 1), along the southeast base of Sumas Mountain, between Highway 11 and Yale Road, was once the approximate shoreline of the former Sumas Lake. Between 1920 and 1924, Sumas Lake was drained for flood control and agricultural purposes after which the first flood protection dikes were constructed. The site of the main breach of the Sumas River Dike is approximately 4.5 km southwest (upstream) of the Barrowtown Pump Station (see Fig. 1) between about Chainage 5+400 and 5+550.

**Fig 1.** Sumas River Dike breach location.


The most recent upgrade occurred in the late 1980's as part of the Abbotsford Flood Control Program and included adding a granular filter layer to the land side slope of the dike. The dike bulk fill was sourced locally from the nearby quarries including the Short Road Pit and the Quadling Quarry, located adjacent to Barrowtown Pump Station. The land side and water side slopes of the original dike section vary from 2 Horizontal to 1 Vertical (2H:1V) to 3H:1V, with toe to crest height between about 4m to 5m and a crest width of about 4m. A typical section of the original dike section for the reach of dike that was breached (taken from the "As-Constructed" Drawing Set No. 5460-1-10, Rev. A, Sheets 7 to 15, dated 1988 and prepared by Crippen Consultants) is shown on Fig. 2.

**Fig 2.** Original Dike Section.

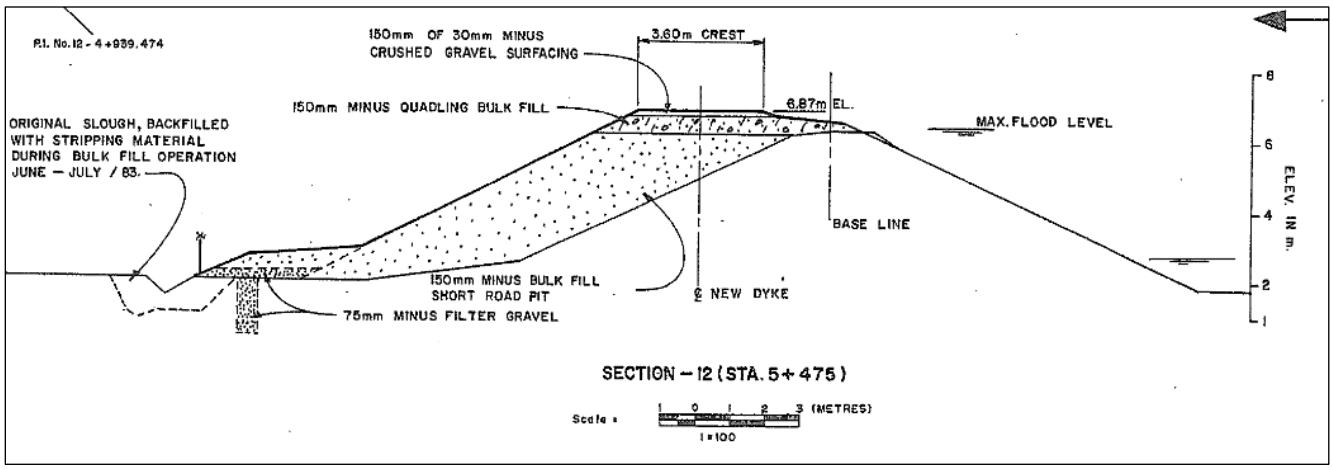


The dike is underlain by a surficial layer of lacustrine deposits (silt to clay), normally less than 5m thick, which is underlain in some areas by Fraser River Sediments, comprising fine sand to clayey silt. These conditions were checked by a site-specific geotechnical exploration carried out following completion of the initial emergency repair and prior to design for the remedial phase of the work to re-establish a low permeability core.

## The Breach

The Sumas River Dike Breach occurred on November 16, 2021, during a series of unprecedented atmospheric river events. The breach occurred as a result of floodwaters from the Sumas River overtopping the dike followed by rapid downcutting of the dike structure allowing floodwaters from the Sumas River to flow into Sumas Prairie. The length of the dike breach was about 150m with scour that extended about 4m below the original ground surface (base of dike) and extended about 150m south into the farm field adjacent to the dike. Google Earth Imagery dated July 29, 2022, clearly shows the extent of the initial emergency repair of the dike breach and scour hole in the adjacent farm field. An aerial photograph of the breach taken on November 17, 2021 (day after the breach), is shown on Fig. 3.

**Fig 3.** Aerial image of the dike breach.

Visual observations of the dike near the breach clearly showed evidence of significant erosion and downcutting of the landside slopes of the dike with several sections of the dike slope eroded to near-vertical configuration near the landside crest of the slope. The exposed near-vertical sand and gravel fill was the material that was added to the landside of the dike in the 1988 upgrade with clear evidence of the well-compacted layers developed during the previous upgrade construction. Deposits (pinnacles) of gravel and cobble sizes extended far into the adjacent farm fields at several locations. Fig. 4 illustrates erosion that occurred along the landside slopes of the dike as a result of overtopping.

**Fig 4.** Erosion on landside slope of the dike.

## Closing the Breach

At the breach, most if not all of the dike structure was lost over a length of about 150m, and in addition, a large scour hole was eroded well below the toe of the dike and beyond, extending some 150m into a farm field to the southeast. The scour hole was about 3m to 4m below the base (bottom) of the existing dike. Ideally, a dike should have a low permeability core constructed of silty and/or clayey soils. However, emergency repair work was carried out during periods of intense precipitation, working initially under conditions of flowing floodwaters and partially underwater, making it impossible and impractical to use fine-grained soils. To attempt to do so would likely have been disastrous. The plan put forward for closure of the breach was to construct an initial crossing (closure) to stop flow from Sumas River, then continue to widen and build up the closure once the open flowing water was stopped. Fig. 5 shows the initial construction of the dike breach closure.

**Fig 5.** Initial Breach Closure.


The entire closure of the breach was constructed using crushed granular fill of varying sizes, with coarser 600mm minus crushed rock specified for the outside (along the side slopes) and finer 75mm minus crushed rock specified within the central portion of the dike. The initial closure was widened to the south and raised using the finer 75mm minus crushed rock to allow for future installation of a low permeability barrier or core. The widening and raising of the breach closure continued using the smaller crushed rock (see Fig. 6). This material was placed in lifts and compacted using a large vibratory compactor. Specifying the use of finer 75mm minus crushed rock to construct the central portion of cross-section for the dike closure was essential in order provide some degree of flexibility in terms of considering options to reinstate a low permeability barrier, without which, the dike would leak.

**Fig 6.** Construction of the breach closure.

As the dike breach repair widening and raising was nearing completion, the Sumas River was again reaching near flood stage levels during the second series of Atmospheric Rivers. It was observed that some of the finer, loose and unconfined material within 75mm minus crushed rock fill material was starting to mobilize (move) in localized zones where seepage was greatest on the landside slope of the dike. Subsequently, a layer of larger 600mm minus crushed rock was placed on the landside of the dike as ballast and support. It was recognized from the onset, that seepage through the body of the dike closure would occur and continue until such time that a suitable low permeability barrier or core was installed to mitigate seepage.

Fortunately, the source of fill material was relatively close to the site, being the Jamieson Quarry on the south side of Sumas Mountain. Even though the material source was close to the site, there was only one open haul route available during one period of the initial operations due to widespread flooding. A section of that haul route adjacent to the Sumas River, which was experiencing overland flooding from upslope, was continually monitored and maintained to keep it open to truck traffic.

During initial construction of the dike breach closure, spatial constraints at the breach site did not allow for more than one excavator and one dump truck at a time with just sufficient space for the dump truck to turn around and leave once it was emptied. With the dike only being wide enough for one standard dump truck, trucks were continually being advanced forward to the breach moving from pullout to pullout along the dike between the empty trucks returning from the breach site. Loaded dump trucks were lined up waiting to access the dike at times that extended over one kilometre in length (see Fig. 7).

**Fig 7.** Loaded trucks waiting to access the dike.

Once the initial breach closure was completed (cutting off open flow through the breach) and had sufficient width, trucks could then follow a haul route on the dike without the need to turn around at the breach site. Fig. 8 shows the landside slope of the completed dike breach closure with adjacent water-filled scour hole which is on the land side of the dike.

**Fig 8.** Landside slope of the completed dike breach closure.

## Geotechnical Exploration

After the emergency repairs to close the breach were completed, a geotechnical exploration was completed to check the extent (depth) of the recently-placed crushed rock fill zone, the characteristics of the underlying foundation soils and to confirm the presence or absence of larger rock sizes within the central portion of the repair (constructed of the finer 75mm minus crushed rock) that would present as obstructions to the proposed core construction activities. This information was also used to establish the required extent of the low permeability barrier and to assess suitable options to construct a low permeability barrier required to mitigate seepage through the breach closure. Twelve (12) test holes were drilled using sonic drilling methods to just over 15m depths within the central portion of the breach closure spaced out along the length of the repaired section. A summary plot of the test hole results is shown on Fig. 9. Of note, the geotechnical exploration did detect some larger pieces of crushed rock in that zone that was intended to be 75mm minus crushed rock.

**Fig 9.** Summary of test hole exploration.

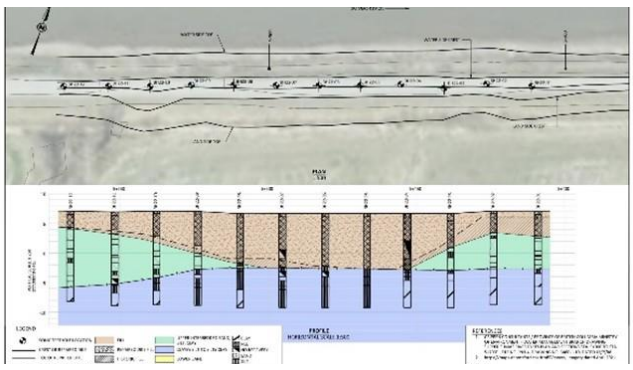

## Options for Seepage Mitigation

As previously discussed, the entirety of the dike breach repair was constructed using crushed granular fill of varying sizes and therefore seepage would continue through the body of the dike until a low permeability core or barrier was installed within the central portion of the dike. Three options for seepage mitigation that were considered included: 1) re-construction of the dike section with a low permeability core; 2) construction of a low permeability core using deep soil mixing technology; and 3) construction of a steel sheet-pile barrier.

The re-construction option would require removal of a large portion or most of the repaired section of dike breach and replace it with new engineered fill including a low permeability soil core, filter(s), drainage, and bulk fill zones. This option would be time consuming and encounter considerable constructability challenges (e.g., excavation support, dewatering, and the like) associated with earthworks being carried out as much as 4m or more below the groundwater table and in proximity of the flowing Sumas River. (e.g., a temporary cofferdam would most likely be required during construction).

The deep soil mixing option involves mechanically mixing the in-situ soil, in this case 75mm minus crushed rock/gravel dike fill, with a bentonite/cement slurry mixture to form a low-permeability barrier (core) along the center of the breach closure (with permeability consistent with the in-situ silty and clay soils). The barrier is constructed by building a series of overlapping rectangular panels along the centreline of the breach closure to form a barrier to mitigate seepage. The primary construction challenge would be associated with encountering larger crushed rock sizes resulting in cutter teeth breakage and possible cutter head damage.

The steel sheet-pile wall option would involve installing (driving) a continuous line of interlocking sections of steel sheet-piles along the centre of breach closure to act as a low-permeability barrier to mitigate seepage through the dike fill. However, there could be constructability challenges associated with driving sheet piles through well-compacted 75mm crushed gravel fill and encountering larger crushed rock sizes while maintaining connection between adjacent sheet piles.

One of the key considerations in selecting the preferred option to reinstate a low permeability barrier in the breach closure was that, as much as possible and practical, the preferred option should minimize the need for de-construction.

The option selected for construction of the low permeability core was Cutter Soil Mixing (CSM), which is one of several proven and locally available methods for deep soil mixing and successfully used in other similar barrier applications (Arnold et al., Holzman et al. and others (2011)).

## Design of the Barrier

The overall objective was to construct a barrier within the closed breach section that was flexible and with low permeability thereby creating a structure that would once again function as a dike.

Steady state seepage analyses were carried out using commercially available computer software Slide (RocScience 2018, ver. 8.032) to confirm the benefit of installing a barrier with low permeability ($1x10^{-9}$ m/s) to mitigate seepage flows through the breach closure which was constructed entirely of crushed rock of varying sizes (75mm minus material in the central portion and larger, 300mm to 600mm minus on the outside slopes). The findings of the seepage analysis indicated that for the breach closure without a low permeability barrier, the estimated seepage through the closure would likely range in the order of between about 5 and 20 litres/min per metre length of dike closure. This considers conditions in the Sumas River that vary from "normal" to flood level. Installing a low permeability barrier that is 600mm thick and extends 4m into the underlying foundations soils reduces seepage by about two (2) orders of magnitude, or to between about $1x10^{-2}$ and $5x10^{-2}$ litres/min per metre length of the dike closure. Fig. 10 illustrates the seepage analysis model and plots of findings under flood conditions.

To maintain flexibility in the barrier, an Unconfined Compressive Strength (UCS) of 1 MPa was specified for the constructed barrier.

**Fig 10.** Seepage analysis plots.

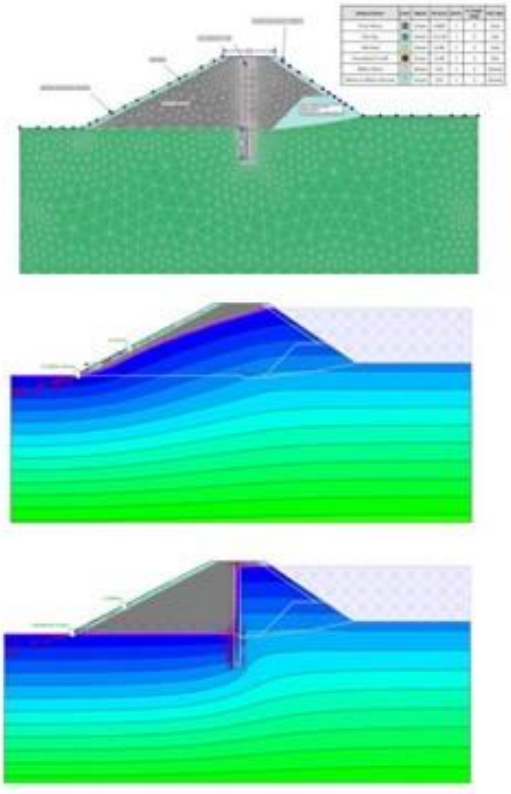

## Construction of the Barrier

As previously noted, the barrier was constructed by means of Cutter Soil Mixing ("CSM") technology. CSM is one of several deep soil mixing methods used locally in construction of cut-off barriers and in ground improvement applications. The CSM equipment (RTG RG 27-S rig) consists of a large drill rig, similar to a pile driving rig, that is equipped with a mast that supports a rigid kelly-bar to which the cutting tool is attached. The cutting tool is comprised of counter-rotating drums that are fitted with cutting teeth with a configuration that is specifically designed for cutting and mixing in-situ soils with bentonite and Portland cement slurries. The CSM rig is supported by an excavator, loader, and a batch plant that produces the bentonite and Portland cement slurries. The bentonite slurry and Portland cement slurry are prepared in the batch plant (set up and located adjacent to the work site) and pumped though hoses to the CSM rig. Fig. 11 shows the CSM rig used for construction of the barrier.

**Fig 11.** CSM Rig.

The CSM process involves constructing rectangular panels that are 2.8m long by 640mm wide and extend to the target depth. As the cutting tool advances or cuts its way down into the ground, bentonite slurry is continually added to aid as a cutting fluid and to lower the permeability of the mixed soil-slurry mass. When the cutting tool reaches the target depth, Portland cement slurry (required for strength) is then introduced as the cutting tool is slowly retrieved from the ground. Once the Portland cement is introduced into the process, the contractor's experience and time become a factor as any missteps by the crew or equipment issues could lead to the cutting tool getting stuck in the ground. The contractor tailors the bentonite slurry and Portland cement slurry application to achieve the performance requirements set out in the contract specifications. A total of sixty (60) CSM panels were required to construct the barrier with depths varying between 5.25m and 12.75m. The CSM panel layout is shown on Fig. 12.

**Fig 12.** CSM panel layout.

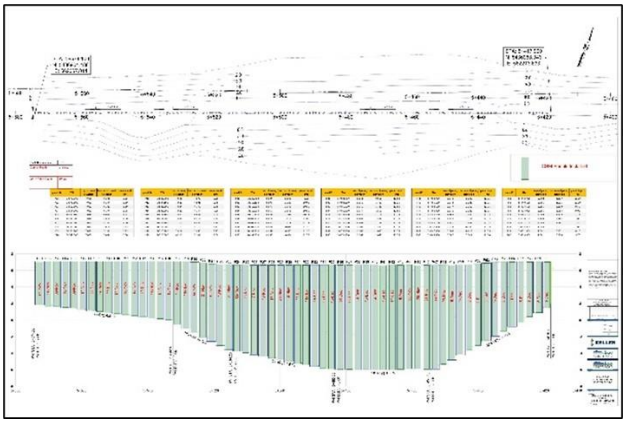

During the CSM panel construction process, an onboard monitoring system collects real-time data for each panel construction including progress (cutting tool depth vs. time), bentonite slurry application, Portland cement slurry application and deviation of the cutting tool/kelly-bar from the barrier alignment. A CSM report, or also commonly referred to as "B-Report", is prepared for each panel that is constructed (see Fig. 13).

**Fig 13.** Typical CSM report.

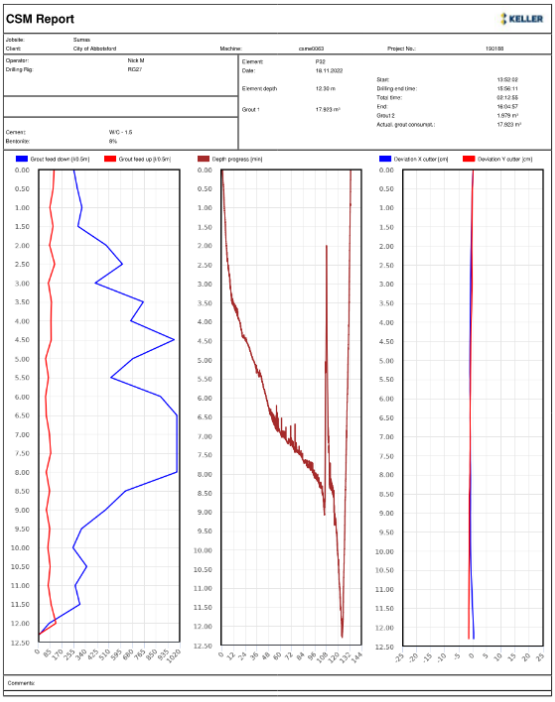


The left plot in the CSM report in Fig. 13 is a record of bentonite slurry consumption represented by the right (blue) line as the cutting advances down into the ground and then Portland cement slurry consumption represented by left (red) line as the cutting tool is withdrawn upward. The central plot records the progress of the cutting tool for both advance into the ground and withdrawal (from left to right). It is noted that there is greater time and "noise" on the progress plot between about 6.5m and 9m; this is due to difficulties advancing the cutting tool beyond some pieces of larger crushed rock in that zone within the crushed dike fill that was used to close the breach. For Panel No. 32, shown on Fig. 13, it took about 2 hours, 12 minutes to construct the panel which is considerably longer than might be expected.

Some of the larger pieces of crushed rock being present in what is supposed to be mostly 75mm minus crushed rock is most likely due to some larger material being used on the water side during construction of the initial closure ramp into the breach, some larger pieces mixed in with fill delivered to the site and possibly also due to this material having been placed in flowing water. As much as possible and practical, the operator tried to keep the water side slope of the initial closure as steep as possible to keep the outside larger pieces of crushed rock away from the central portion of the dike closure. A total of about 300 sets of teeth were broken on the CSM cutter tool bouncing and grinding on pieces of larger crushed rock that were encountered.

After a period of breakage and delays, a decision was made to pre-drill the panel locations to try to retrieve some of the larger pieces of crushed rock or possibly loosen them with the hopes that they could be "kicked" aside by the cutting tool. Initial attempts at pre-drilling were carried out with uncased holes; however, due to caving in some of the hole, particularly below the water table, this approach had limited success and was eventually abandoned.

The second approach at pre-drilling with cased holes proved to be far more successful. The contractor developed an efficient method for pre-drilling using two adjacent cased holes where the lead (first) cased hole was being drilled (and casing advanced into the ground) with material retrieved dumped onto the ground. After sorting through the fill material and removing the larger pieces of crushed rock, the remaining finer crushed gravel fill was then replaced into the trailing (second) cased hole (and that casing gradually withdrawn). In the end, about half of the sixty (60) CSM panels required pre-drilling. Fig. 14 shows the predrilling arrangement with cased holes.

**Fig 14.** Pre-drilling with casing.

Pre-drilling, particularly with cased holes, proved to be beneficial in getting the remaining CSM panels completed in a much shorter time, and of course, with considerably less risk of damaging equipment as the effort to construct the panel is reduced. Panel Nos. 33 to 43 were pre-drilled using the cased hole approach. Fig. 15 shows both the CSM and pre-drilling equipment on top of the dike breach closure (the water filled scour hole is in the foreground and Sumas River and Sumas Mountain in the background).

**Fig 15.** CSM and pre-drilling equipment.

The benefit of pre-drilling with a cased hole can be illustrated looking at the CSM Report for Panel No. 34 (see Fig. 16), which is the panel that was installed two (2) panels east of Panel No. 32 (results of which are previously shown above). The time to complete the panel was considerably less, about 54 minutes in this case. As can be seen in the progress (middle) plot on Fig. 16, the cutting tool progress now shows a relatively uniform up and down of the cutting tool without the "noise" associated with bouncing and grinding on larger pieces of crushed rock.

**Fig 16.** CSM Report for Panel No. 34.

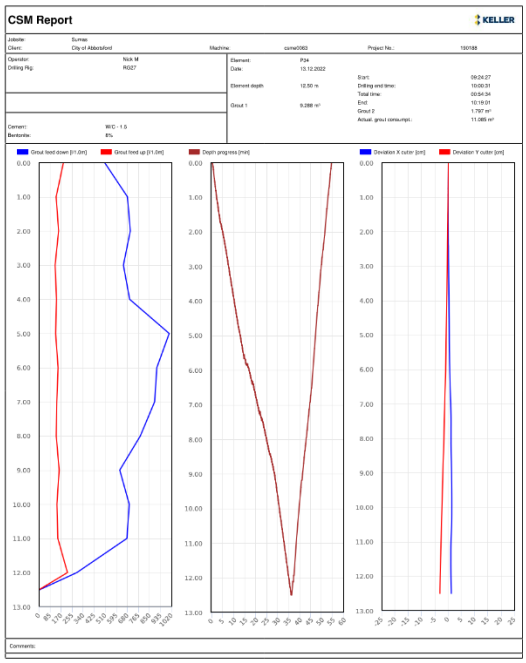


In addition to the challenge of dealing with obstructions, cold weather played havoc with CSM equipment in the latter part of November and early December 2022 resulting in freezing of hoses and lines that feed bentonite and Portland cement grout to the cutting tool.

Samples obtained from completed panels were collected on a prescribed sampling schedule set out in the contract specifications for Unconfined Compressive Strength (UCS) testing to confirm the CSM panels achieve the specified UCS. Samples were also obtained for hydraulic conductivity testing and results of this testing confirmed that the hydraulic conductivity of the constructed panels satisfied the contract specification.

## Final Review and Fish Salvage

After completion of the CSM barrier, a final field review of the landside slope was completed looking for visible seepage (point sources of flow) but could only be completed after the water filled scour hole was drained.

Following about a one month delay due to unseasonably cold weather and the Christmas break, the contractor was able to drain (by pumping) the water-filled scour hole on the landside of the breach repair. During the pumping process, and as water levels were lowered in the scour hole, a fish salvage was undertaken to recover fish trapped in the scour hole because of the dike breach. Fish species recovered included several sturgeon some up to 2.1m long, a pair of coho salmon, and numerous other fish. These fish were flushed through the breach when it occurred and then were effectively trapped in the water-filled scour hole for a period in excess of one year. Fig. 17 shows one of several sturgeon that were recovered.

**Fig 17.** Sturgeon recovered from the scour hole.

Once the water was pumped down, and with fish salvage work still underway, a visual review was carried out along the exposed water side slope of the dike breach repair. At the time of the field review, the head difference between the Sumas River and the scour hole was about 3m. No point sources of flow were observed along the exposed water side slope of the dike breach repair, but several areas of seepage flow were observed along the perimeter of the scour hole with this seepage being groundwater draining from the surrounding farm field. Discussions with the farmer, whose property was directly impacted by the breach, confirmed that the area of the field occupied by the scour hole was always considered a localized wet area. Fig. 18 shows the drained scour hole with fish salvage still underway.

With no observed point sources of flow along the water side slope of the dike breach repair satisfying the final performance criteria, the repair was considered complete.

**Fig 18.** Drained scour hole and exposed water side slope of dike breach repair.

## Challenges

As with any major emergency work, challenges will test the collective experience and innovation of the team with the repair of the Sumas River Dike breach being no different. The key challenges faced during repair of the breach included:

- Weather – during the initial stages of the emergency works, heavy precipitation made for difficult working conditions including continued flooding of some crucial access roads requiring continual monitoring and maintenance. During initial emergency repair of the breach, and during the second series of atmospheric rivers, rising flood waters did threaten continued work at the breach site. Trigger points (levels) had to be established in terms of the minimum freeboard required to allow work to continue.
- Materials – securing fill materials of suitable quality and quantity can be challenging. Fortunately, the large quantity of material required to initially close the open breach and then raise the dike could be produced at the Jamieson Quarry situated on the southeast side of Sumas Mountain. One of Mainland's operations had to be reserved to the Sumas Dike emergency repair only, as there was, as one would expect, other demands competing for material and resources as a result of the widespread flooding. At times, materials delivered to site had to be sorted either because the material was not appropriate or large pieces of crushed rock were intermittently mixed in with finer material or it was just the wrong material which had to be dealt with after it was dumped, in turn slowing down progress.
- Access – much of Sumas Prairie was flooded, access and haul routes had to be planned and carefully staged and coordinated as many of the local roads including stretches of the Trans-Canada Highway were closed. Fortunately, the source of fill was nearby; however, there was only one open route during initial operations which had to be constantly monitored and maintained because of overland flooding; failure to do so would have resulted in losing part of the road. Police and other emergency authorities were controlling access to remaining open roads including accessible local sections of the Trans-Canada Highway for public safety. Hauling on top of a narrow dike required a well-coordinated staging plan and concerted effort to ensure timely, continual, and safe delivery of fill material to the breach site.
- Subsurface obstructions – during construction of the low permeability barrier in the closed breach section, larger pieces of crushed rock were encountered and posed a significant challenge for the CSM equipment resulting in delays and equipment damage. A highly experienced contractor was able to overcome those challenges.

## Lessons Learned

Several lessons were learned from this (hopefully) once in a lifetime experience:

- An experienced and motivated team was crucial to the successful completion of the initial emergency works in a safe and timely manner.
- Some foresight in terms of specifying appropriate materials for the initial dike closure (the finer 75mm minus crushed gravel for the central portion of the closure) proved invaluable to the successful construction of a low permeability barrier using CSM technology without the need to deconstruct the initial works.
- Pre-drilling with casing proved to be a successful approach to removing obstructions (larger crushed rock) within the dike fill and contributed to successful construction of the low permeability barrier.

## Acknowledgements

The authors wish to acknowledge and thank the City of Abbotsford for the opportunity to share knowledge gained from this project with the geotechnical consulting community. Further, the authors wish to thank their colleagues for the invaluable support provided during the entirety of the project and in preparing this publication.

## References

Arnold, M., Beckhaus, K. and Wiedenmann, U. 2011. Cut-off wall construction using Cutter Soil Mixing: a case study, GmbH & Co., Geotechnik 34 (2011), Heft 1.

Holzmann, B., MacKay, Siddle, D. and Olivera, R., 2019. Site Characterization for Cutter Soil Mixing of a Vertical Barrier Wall, 26th Vancouver Geotechnical Society Symposium (2019).

# Limitations in Existing Methods for Analysing MSE Walls Reinforced with Steel Strips

Lalinda Weerasekara, Ph.D., P.Eng.
Senior Geotechnical Engineer, WSP Canada Inc., Nanaimo, BC.

**ABSTRACT** The current practice for designing mechanically stabilized earth (MSE) structures involves empirical methods to estimate the maximum reinforcement loads using different variants of tributary area method (e.g., AASHTO Simplified, Coherent Gravity and Simplified Stiffness methods) which were validated only for working stress conditions. Since soil-reinforcement interaction is not explicitly accounted in these methods, there are key limitations in attempting to estimating the ultimate state especially in walls with inextensible reinforcements. This paper compares above design methods against the Soil Reinforcement Interaction (SRI) method, an analytical solution that considers the complex soil-reinforcement interaction occurring in MSE walls. Several critical shortcomings of the current state practice can be overcome using this method, including the ability to (i) estimate the ultimate state by considering more realistic failure modes, (ii) estimate the load transmitted to the facing connection, (iii) estimate the tensile force distribution along the reinforcement (iv) quantify the toe resistance (v) analyse walls with non-uniform reinforcement lengths and configurations (vi) design for vertical and horizontal obstructions and (vii) explain different behavioural characteristics. Where applicable, actual instrumented walls are utilized to demonstrate these benefits. The paper focuses mainly on walls reinforced with inextensible reinforcements where above shortcomings have the greatest impact.

## Introduction

This paper attempts to highlight some of the key limitations of existing design methods available for estimating the internal stability of Mechanically Stabilized Earth (MSE) walls and how those can be overcome using the Soil Reinforcement Interaction (SRI) method. The paper focuses mainly on walls reinforced with inextensible reinforcements such as steel strips, although certain comments are also applicable to MSE walls with extensible reinforcements. For comparison purposes, Coherent Gravity (Schlosser 1978), AASHTO Simplified (AASHTO 2020) and Simplified Stiffness (Allen and Bathurst 2015) methods are considered in this paper. First two methods are recommended in the American Association of State Highway and Transportation Officials (AASHTO) and Canadian Highway Bridge Design Code (Canadian Standards Association 2019). for the design of MSE walls with inextensible reinforcements. In these methods, the maximum reinforcement forces ($P_{max}$) in the most general form, is calculated based on the tributary area concept as follows:

[1] $$P_{max} = K\,\sigma'_v\,S_v S_h$$

$\sigma'_v$ is the vertical effective stress at reinforcement level, $S_v$ and $S_h$ are the vertical and horizontal spacings between reinforcements and $K$ is an empirical lateral earth pressure coefficient which is back calculated from instrumented walls. Consequently, different $K$ values and distributions with depth are considered to demonstrate the differences in reinforcement stiffnesses and soil-reinforcement interactions. Using $P_{max}$ calculated for each reinforcement layer, the following three failure mechanisms are evaluated for each reinforcement layer: (a) tensile rupture of the reinforcement, (b) pullout and (c) connection failure.

## Soil Reinforcement Interaction (SRI) Method

A brief description of the SRI method is given below and further details can be found in Weerasekara et al. (2017). The SRI method is a combination of the following three sub-models:

1. SRI Friction model: A model to account for the frictional forces at the soil-reinforcement interface.
2. SRI Local model: An analytical solution to model the soil-reinforcement interaction in each reinforcement; and
3. SRI Global model: An approach to account for the equilibrium and interaction of multiple reinforcements in the reinforced soil mass.

### SRI Friction Model

The friction per unit length ($T$) at the soil-reinforcement interface is expressed using a bi-linear model (Fig. 1), where the peak frictional resistance ($T_1$) is expressed in the following form.

[2] $$T_1 = \frac{2bH\gamma \tan\varphi'_g}{1-[2(1+\nu)/((1-2\nu)(1+2K_0))]\tan\varphi'_g \tan\psi_{max}}$$

where $b$ is the width of the reinforcement, $H$ is the burial depth, $\gamma$ is the unit weight of the soil overburden, $\varphi'_g$ is the soil-reinforcement interface friction angle, $\upsilon$ is the Poisson's ratio of soil, $K_0$ is the lateral earth pressure coefficient at-rest and $\psi_{max}$ is the peak angle of dilation. As the magnitude of soil dilation depends on the mean effective stress, the classical stress-dilatancy framework proposed by Bolton (1986) can be used to express $\psi_{max}$ in the following form:

$$\Psi_{max} = 6.25(I_D(Q - ln\sigma') - R) \quad [3]$$

$\Psi_{max} = 6.25(I_D(Q - ln\sigma') - R)$

where $\sigma'$ is the mean effective stress and $I_D$ is the relative density of the soil which can be obtained from conventional testing or approximately estimated based on the degree of compaction or measured soil unit weight. Parameters $Q$ and $R$ are the only empirical parameters in the model which generally depend on the soil type. The frictional resistance attributed to soil dilation is expected to decrease gradually and becomes negligible at a displacement of ($\overline{u_2}$). Above is an important consideration for extensible reinforcements because different sections of the reinforcement will experience different magnitudes of friction due to the progressive development of friction along the reinforcement. At a displacement of ($\overline{u_2}$), the interface friction per unit length ($T_2$) is given by the following:

$$T_2 = 2bH\gamma \tan\varphi'_g \quad [4]$$

The value of $\overline{u_2}$ is typically obtained from experimental observations. For a typical MSE wall, the results are relatively insensitive to the value selected for $\overline{u_2}$. Guidelines related to the selection of input parameters is given in Weerasekara et al. (2017).

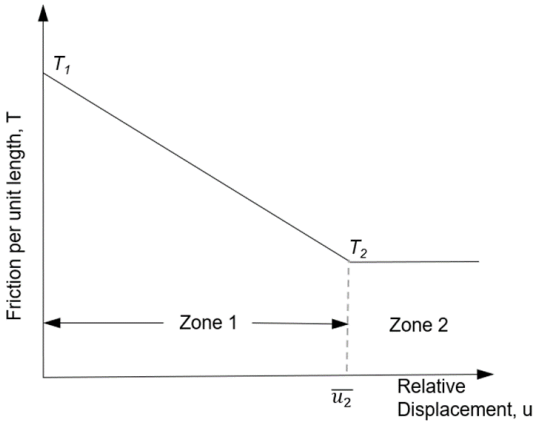


**Fig. 1.** Schematic representation of SRI Friction model

$$T_1 = \frac{2bH\gamma \tan\varphi'_g}{1-[2(1+v)/((1-2v)(1+2K_0))]\tan\varphi'_g \tan\psi_{max}}$$

## SRI Local Model

Using the interface frictional model and reinforcement stiffness, the following governing equations of the SRI Local model can be obtained by considering the force equilibrium at an element level.

$$u = \left(\frac{\kappa}{\lambda}\right)\left(1 - \cos\sqrt{\lambda}l\right) \quad [5]$$

$$\varepsilon = \left(\frac{\kappa}{\sqrt{\lambda}}\right)\left(\sin\sqrt{\lambda}l\right) \quad [6]$$

where,

$\lambda = \frac{(T_1 - T_2)}{J_r \overline{u_2}}$ and $\kappa = \frac{T_1}{J_r}$ with $\sqrt{\lambda}l < \frac{\pi}{2}$

$l$ is the mobilized friction length along the reinforcement due to the displacement occurring at the failure plane of the MSE wall. In a pullout test, $u$ is displacement at the pulling end which is equivalent to one-half of the separation of the stable and unstable soil masses along the failure plane of the MSE wall. $J_r$ is the axial stiffness of the reinforcement which is equal to the reinforcement modulus multiplied by the cross-sectional area. In terms of steel strip reinforcements, this represents the Young's modulus times the total cross-sectional area of steel strips encountered within a unit width.

If the displacement is known, the mobilized frictional length along the reinforcement ($l$) can be obtained by rearranging Eq. (5) as follows:

$$l = \left(\frac{1}{\sqrt{\lambda}}\right)\cos^{-1}\left(1 - \frac{u\lambda}{\kappa}\right)$$

$$l = \left(\frac{1}{\sqrt{\lambda}}\right)\cos^{-1}\left(1 - \frac{u\lambda}{\kappa}\right) \quad [7]$$

Knowing the strain, tensile force in the reinforcement at any given location can be obtained as follows:

$$P = J_r \times \varepsilon \quad [8]$$

Above analytical approach provides a framework to relate the displacement, strain, force and mobilized frictional length along the reinforcement. If any single parameter is known, the remaining three parameters can be estimated.

In this formulation, it is important to highlight the difference between $P$ and $T$. Note that $T$ acts on the reinforcement as an external frictional force and independent of the reinforcement stiffness, while $P$ is the force developed in the reinforcement due to this

external force and depends on the reinforcement stiffness. This difference is often overlooked and has led to several confusions.

## SRI Global Model

The SRI Global model provides a framework to assess the stability of the entire reinforced soil mass, such that the total resistance provided by the soil reinforcements are equated to the total driving forces from earth pressures, surcharge and other loads that contributes to the instability. The lateral earth pressure will continue to decrease from at-rest condition and reach the active state if the displacement is large enough. While this occurs, the resistance from reinforcements will increase as the soil mass displaces. For this computation, the moments are calculated about the base of the wall since the mobilized resistance at this location ($R_T$) is not typically known. The equilibrium is reached when the total driving moment is equal to the total resisting moment, which can be expressed as:

[9] $$\mathrm{F}_s \times H_s = \sum_{i=1}^{n} P_i \, h_i$$

where, $P_i$ is the maximum tensile force in the reinforcement, $h_i$ is the height to $i^{th}$ reinforcement from the base of the wall and $n$ is the number of reinforcements. $F_s$ is the total horizontal driving force and $H_s$ is height to the resultant horizontal driving force measured from the base of the wall (see Fig. 2). For a given displacement of the unstable soil mass, the tensile force developed in each reinforcement layer is obtained from the SRI Local model.

Once the moments are in equilibrium, $R_T$ is the difference between horizontal driving forces and total resistance provided by the reinforcements. Besides the force equilibrium, above analytical framework ensures the displacement compatibility.

Successful implementation of the SRI Global model requires, proper application of boundary conditions encountered in a MSE wall. As schematically shown in Fig. 2, any reinforcement encountered in a MSE wall should fall into one of the following four categories:

(i) No impact from boundary conditions (Case 1): Mobilized length measured from the failure surface is less than the distance to the wall facing or to the free end. The equations derived from the SRI Local model are applicable without any modifications. This is the most common condition encountered in walls with extensible reinforcements using the minimum reinforcement length recommended in design guidelines.

(ii) Free end of the reinforcement is mobilized (Case 2): In this case, the maximum tensile force is obtained using the SRI Local model with $l = L_2$ (< $L_1$). As shown in Fig. 2, $L_2$ is the distance from the failure surface to the free end and $L_1$ is the distance from the failure surface to the wall facing. Additional increase in displacement will not result in further increase in reinforcement load. In walls with inextensible reinforcements, this boundary condition is often observed in the upper layers.

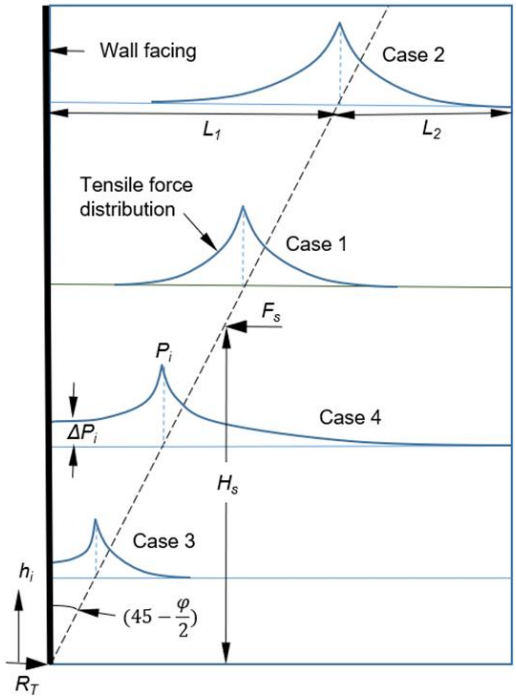


**Fig. 2.** Different boundary conditions experienced by reinforcements.

(iii) Resistance from the wall facing is mobilized (Case 3): The force in the reinforcement can be estimated using the SRI Local model until the mobilized length is equal to $L_1$ (< $L_2$). Beyond this displacement, any increase in displacement ($\Delta u$) will result in a net increase in tensile force ($\Delta P$) which is given by the following:

[10] $$\Delta \mathrm{P} = J_r \left[\frac{\Delta \mathrm{u}}{L_1}\right]$$

The total tensile force along $L_1$ length is the summation of $\Delta P$ and the reinforcement load estimated from the SRI Local model using Eq. (8). Note that $\Delta P$ is the connection load developed at the facing. This is a common occurrence in bottom layers of walls reinforced with inextensible reinforcements.

(iv) Resistance of the wall facing and free length are mobilized (Case 4): Initially, the wall facing resistance is mobilized similar to Case 3. Further increase in displacement will mobilize $L_2$ length. When this occurs, tensile force will not increase further similar to Case 2. Unless the wall includes a truncated base, this is judged to be a rare occurrence and likely to occur in bottom reinforcements of walls with inextensible reinforcements.

The SRI model can be implemented in a spreadsheet as outlined by Weerasekara et al. (2017). Except for *Q* and *R* parameters in Bolton's equation, the input parameters used in the SRI model are not empirical and they can be obtained experimentally or through direct measurements. For geogrids, ribbed steel strips and steel wire meshes, pullout tests can be used to back calculate the interface friction which is otherwise difficult to determine directly. Once the input parameters are known, the solution can be obtained by gradually increasing the wall displacement until the resistance and demand moments are equal. Using nine full-scale instrumented walls reinforced with smooth and rough steel strips, Weerasekara (2018a) demonstrated that SRI method can successfully estimate the maximum reinforcement load distributions under working stress conditions. Although this approach is adopted by other researchers to validate the MSE design approaches, Weerasekara (2018a) highlighted the shortcomings of this approach of validating design methods where the methods are validated only under working stress conditions. Further details related to this aspect are discussed in subsequent sections.

## Shortcomings of Existing Design Methods

### Issue 1: Pullout Resistance Calculation

Pullout failure of reinforcement is recognized as one of the three failure modes associated with MSE walls although it is the rarest failure mode observed in practice (Bathurst et al., 2012, Holtz, 2017). While there are number of studies conducted to improve the predictions of $P_{max}$, there are only a limited number of methods to estimate the mobilized reinforcement length. The most recognized is the method outlined in the FHWA manual FHWA-RD-89-043 (Christopher et al. 1990) which is widely adopted in practice. According to this method, the mobilized reinforcement length (*l*) beyond the potential failure surface is estimated using the following empirical relationship:

$$l = \frac{P_{max}}{F^* \alpha \sigma_v C R_c} \quad [11]$$

where *C* is a factor that accounts for the reinforcement surface area, $R_c$ is the reinforcement coverage ratio, $\alpha$ is a scale effect correction factor and $F^*$ is the pullout resistance factor. The calculated length is further increased by applying an appropriate factor of safety for allowable stress design (or a resistance factor for the limit state design). The reinforcement stiffness, which is the most influential parameter for pullout response, is not explicitly considered and its impact is assumed to be captured indirectly in the empirical parameter $\alpha$. Although method such as Simplified Stiffness method were developed to estimate the impact of reinforcement stiffness on $P_{max}$, once $P_{max}$ is estimated, the pullout resistance is still estimated using Eq. (11) which fails to recognize the direct impact of reinforcement stiffness on the mobilized reinforcement length.

Recognizing the importance of $\alpha$ and $F^*$ on the overall pullout resistance, it is critical to know how these parameters are determined. Current design guidelines recommend $\alpha$ and $F^*$ be determined from direct shear and pullout tests. In a pullout test, reinforcement will continue to elongate before mobilizing the entire reinforcement length. Once the friction is fully mobilized over the entire reinforcement length, the trailing end will begin to move. For extensible reinforcements, Christopher et al. (1990) recommended $\alpha$ be determined at a deflection of 15 mm (5/8-inch) measured at the back of the reinforcement if the reinforcement does not rupture at this displacement. A minimum reinforcement embedded length of 600 mm is recommended for the pullout test. For inextensible reinforcements, corresponding $\alpha$ value is determined when the pulling end or trailing end displacement is 15 mm. Although above deflection limit was selected to limit the deformations in the walls, it is unclear how this unique displacement and reinforcement embedment length relate to the pullout occurrence or serviceability of the actual wall.

Eq. (11) assumes a linear relationship between pullout capacity and normal stress. However, numerous experimental studies have demonstrated that relationship between pullout capacity and overburden stress is nonlinear (e.g., Juran et al. 1998). This is attributed to constrained dilation of dense granular soils which diminishes as the soil overburden is increased. Even if experimental results are available for a certain overburden stress, that cannot be interpolated or extrapolated to other overburden stresses to estimate corresponding $\alpha$ and $F^*$ values due to the empirical nature. It is not practical to conduct pullout tests at all potential overburden stresses to determine $\alpha$ and $F^*$ values for

each reinforcement layer. Moreover, compared to the relationships developed for the SRI method, it is optimistic to assume that $\alpha$ and $F^*$ parameters alone can capture the impact of reinforcement stiffness, overburden stresses and interface friction. Huang et al. (2010) study of the FHWA pullout model indicated a very poor accuracy for geogrids. To overcome the shortcoming, they proposed nonlinear and bi-linear relationships for $\alpha$ and $F^*$ parameters that vary with the normal stress. Even this proposed modification does not consider the actual geogrid-soil interaction; therefore, key parameters such as reinforcement stiffness is absent in the formulation.

In contrast, Eq. (7) of the SRI model incorporates an improved interface friction model (i.e., SRI Friction model) and account for the soil-reinforcement interaction by incorporating the reinforcement stiffness (i.e., SRI Local model) and relevant boundary conditions and impact from other reinforcement layers in the wall towards equilibrium (i.e., SRI Global model). Weerasekara et al. (2017) and Weerasekara et al. (2010) demonstrated that pullout characteristics can be reliably determined using the SRI Local model by modelling large number of pullout tests. A true validation exercise should consider multiple pullout tests conducted at different reinforcement lengths, overburden stresses, etc. Initially, one test may be used to determine parameters such as the interface friction angle if direct measurements are not feasible. The remaining tests should be modelled by changing only the appropriate test variables to check if that will provide an accurate prediction of the measured pullout response. Furthermore, the validation exercise should not focus only on the pullout force - displacement relationship but should also consider interrelationships between displacement, strain and mobilized length since they are all related. For example, it may be possible to achieve a reasonable match for the pullout resistance versus displacement relationship while the prediction for the mobilized reinforcement length is poor. Although it is difficult measure the mobilized length directly, it is possible to measure the instance when the trailing end of the reinforcement starts to move. When this occurs, the mobilized reinforcement length is equal to the reinforcement length inside the pullout box. In pullout tests, this can be used to validate the predictions for the mobilized length.

## Issue 2: Demand at Facing Connection

Besides the pullout and tensile rupture of the reinforcement, the tensile rupture of the reinforcement at the facing connection is recognized as a failure mode associated with MSE wall. As discussed in the subsequent section, this failure mode is more likely to occur in walls reinforced with inextensible reinforcements. Although the actual tensile demand is less than $P_{max}$ at the facing connection, the tensile capacity of the reinforcement at the facing is generally small due to the allowances made for the connection. Therefore, it is critical to know the load transferred to facing connection to determine if the tensile capacity of the connection will be exceeded. However, none of the current design methods can estimate the load at the facing connection because of their inability to predict the load distribution along reinforcements. Therefore, it is typical to assume that tensile demand at the facing connection is equal to $P_{max}$ which occurs elsewhere. This cannot be justified using known physics and also contradicts the observations from instrumented walls. The tensile load transferred to the facing connection is expected to be smaller than $P_{max}$, and will depend on $J_r$, $P_{max}$ and $L_1$.

However in past experiments, it was observed that settlement of the soil behind the wall facing can create drag loads that are transferred to the reinforcement (Damians et al. 2015), especially near the top of the wall. Although the SRI method cannot estimate the these drag loads, they are unlikely to impact the global stability of the wall.

## Issue 3: Ultimate Load, Failure Mode and Factor of Safety Calculations

Though existing design methods can predict the maximum reinforcement loads under working stress conditions with reasonable accuracy, they are not validated against the ultimate collapse limit state. The ability to predict the performance at working stress conditions is only part of the design challenge. Without validating their ability to predict the ultimate load carrying capacity, there is no guarantee that the estimated factor of safety or capacity/demand ratio under limit state design is accurate.

In the current practice, calculations are performed at each reinforcement layer and the failure of the entire reinforcement mass is assumed when the demand in at least one reinforcement exceeds the capacity of a select failure mode. Limitation of this assumption should be apparent especially when displacement-controlled failure modes such as reinforcement pullout are considered. For example, if the friction is fully mobilized in one or more reinforcement (i.e., factor of safety against pullout is unity), can that lead to the failure of the entire reinforced soil mass? The failure surface typically intersects several reinforcement layers. If the pullout resistance is fully mobilized in a certain reinforcement layer(s), further deformation of the wall can increase the contribution from the remaining reinforcement layers until equilibrium is attained. Above limitation may not cause a significant error in walls reinforced with extensible reinforcements

because the failure often occurs due to tensile rupture of the reinforcement away from the connection, and at that moment, the remaining reinforcements may not have a reserve capacity to accommodate the lost resistance from the ruptured reinforcement.

The best example to demonstrate the above limitation is the full-scale instrumented walls completed at the Waterways Experimental Station (WES). The test details and results are given in Al-Hussaini and Perry (1978). One wall was reinforced with smooth steel strips and other was reinforced with nylon strips. Apart from reinforcement type and horizontal reinforcement spacing, two walls were identical with respect to their final design height, vertical reinforcement spacing, reinforcement length, soil type and compaction effort. The walls were 4.9 m long, 3.1 m wide, designed to reach a height of 3.66 m. The steel strip wall was reinforced with six layers of smooth galvanized steel strips of 0.635 mm thick, 102 mm wide and 3.1 m long with a horizontal and vertical spacing of 0.77 m and 0.6 m, respectively. The steel strips were connected to the aluminium facings using double angle connectors and two 6.35 mm diameter bolts. The nylon strip reinforced wall included heavy neoprene-coated nylon fabric strips of 100 mm wide, 2 mm thick and 3.05 m long. While the vertical spacing was similar to the steel strip wall, the horizontal spacing of nylon strips was 1.2 m. Both walls were backfilled with clean sub-angular to angular concrete sand and nominally compacted. Details related to modelling of these two walls using the SRI method can be found in Weerasekara et al. (2017) and Weerasekara (2018b).

Using the current methods, both walls are predicted to fail due to pullout of the upper reinforcements. Although the nylon strip reinforced wall collapsed due to pullout while it was under construction, the steel strip wall experienced less than 5 mm of movement once it reached its design height. As the wall showed no signs of failure, it was surcharged to failure in increments of 12 kPa. Eventually, the wall collapsed when the loading when the surcharge was approximately 90.4 kPa. The inspections of the collapsed wall revealed failures at the facing connection. To the best of author's knowledge, the steel strip reinforced wall is the only wall in the public domain that can be used to validate the ultimate load carrying capacity of a wall reinforced with inextensible reinforcements; therefore, the observations cannot be ignored.

The performance of the wall under all stages of loading was modelled using the SRI model. For each loading increment, wall deformation was incrementally increased until the driving moment is equal to the resisting moment. Figs. 3(a) and (b) show the resisting and driving moments calculated prior to surcharging and with a surcharge of 90 kPa. According to the SRI method predictions, at a surcharge of 90 kPa, the failure was imminent as the connection load in the bottom three layers have approached the tensile strength limit. When this threshold load is exceeded, tensile rupture was simulated by setting the connection strength to zero. This is reflected in the sudden reduction in the resisting moment in Fig. 3(b). According to the SRI method predictions, failure was initiated by the tensile rupture of one of the strips in the bottom three layers at the facing connection. The failure would have been sudden and brittle as the remaining layers are not able to accommodate the surplus load, which is consistent with the actual failure observations. To estimate the failure of this wall, the design method should be able to estimate the distribution of the reinforcement load along the reinforcement, including the force transmitted to the facing connection. Except for the SRI method, other design approaches cannot estimate the load transmitted to the facing connection and there are serious deficiencies in the pullout estimations as highlighted above.

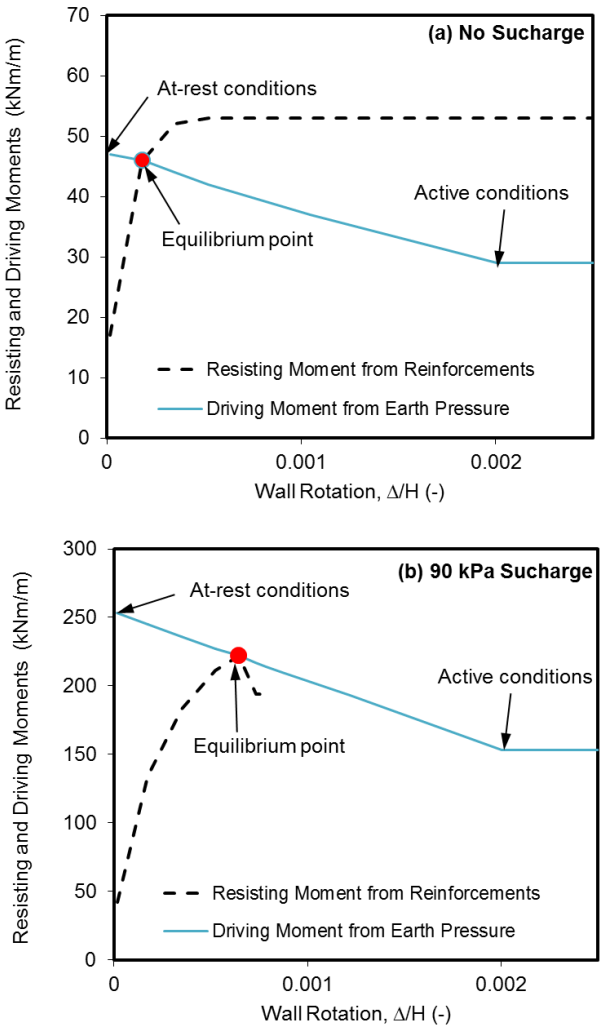

**Fig. 3.** Resisting and driving moments calculated (a) prior to surcharging and (b) with a surcharge of 90 kPa for steel strip reinforced WES wall.

In walls with inextensible reinforcements, another limitation of the pullout resistance calculation using the existing approaches is evident when examining the load (or strain) distributions along reinforcements in instrumented walls. With a minimum factor of safety of 1.5 targeted against pullout under working stress conditions, tensile force is expected to reach zero well before the end of the reinforcement. In other words, Case 2 and 4 boundary conditions should not prevail under working stress conditions according to the existing design methods. However, this contradicts the actual reinforcement strain distributions observed in instrumented walls with inextensible reinforcements, especially near the top of the wall. For example, Runser et al. (2001) published the reinforcement load distributions of the 16.9 m high Minnow Creek wall that was reinforced with ribbed steel strips. The reinforcement length was 15.4 m in the bottom four layers and 12 m in the remaining layers (Fig. 4). The reinforcement load distributions obtained under working stress conditions indicated full mobilization of friction in reinforcement layers located approximately in the upper 12 m (Fig. 5). Each reinforcement layer would have been designed with a minimum factor of safety of 1.5 against pullout. However, the measured reinforcement strain distributions contradict this assertion as the actual factor of safety against pullout is unity in the upper reinforcements even under working stress conditions. As indicated by the small wall deformations measured after construction (i.e., only 30 mm for the 16.9 m high wall), the wall is not at risk of failure from pullout and likely to have satisfied the design intent.

Even in the WES steel strip wall, the existing design approaches would estimate a factor of safety less than unity against pullout in the upper reinforcement layers prior to surcharging of the steel strip reinforced wall. For the WES steel strip wall, it is interesting that the SRI method also predicts full mobilization of reinforcement length in the upper four reinforcement layers (i.e., factor of safety of one) which is consistent with the actual field measurements. The maximum tensile force developed in the upper reinforcement layers were governed by Case 2 boundary condition, such that further increase in wall displacement would not increase the tensile demand as the entire reinforcement length is already mobilized. This is expected as steel strips require only a small displacement to mobilize its entire reinforcement length due to its relatively high stiffness.

Question remains why these two walls did not fail even when most of the reinforcement layers mobilized their maximum pullout resistance? The SRI method shows that only a small fraction of soil strength is mobilized when the equilibrium is reached under working stress conditions although most of the reinforcement contribution is utilized. This is apparent when comparing the demand/resistance plots. The safety margin is largely provided by the soil resistance that has not been mobilized. Above is consistent with the following statement made by Prof. Bob Holtz during the 2017 Terzaghi lecture: "*With steel-reinforced soil, the steel does most of the work, and the sand just goes along for the ride. Not so with geosynthetic reinforcement*". Although this has been common knowledge, only SRI method can provide an analytical explanation to verify this assertion.

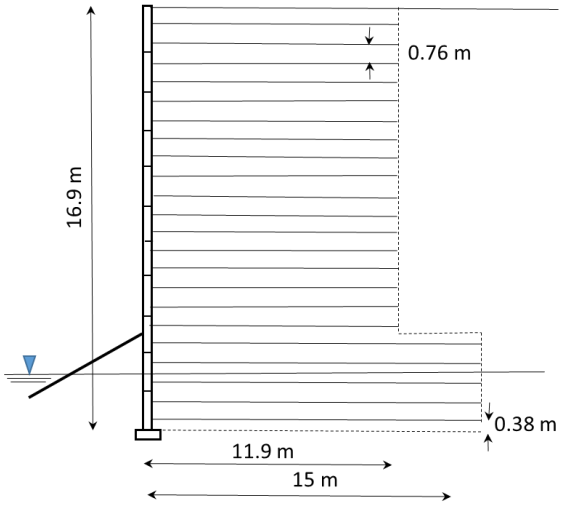


**Fig. 4.** Wall geometry of Minnow Creek Wall

Furthermore, analysis of the WES steel strip wall demonstrates that failure was governed by more than one failure mode (i.e., pullout of the upper reinforcements and tensile failure of the bottom reinforcements at the facing connection). Sensitivity analyses carried out by the author on other steel strip reinforced walls have indicated a similar failure mechanism in walls built to current standards. This complex interaction between different reinforcements and gradual mobilization of soil and reinforcement resistances could not be demonstrated using other design methods.

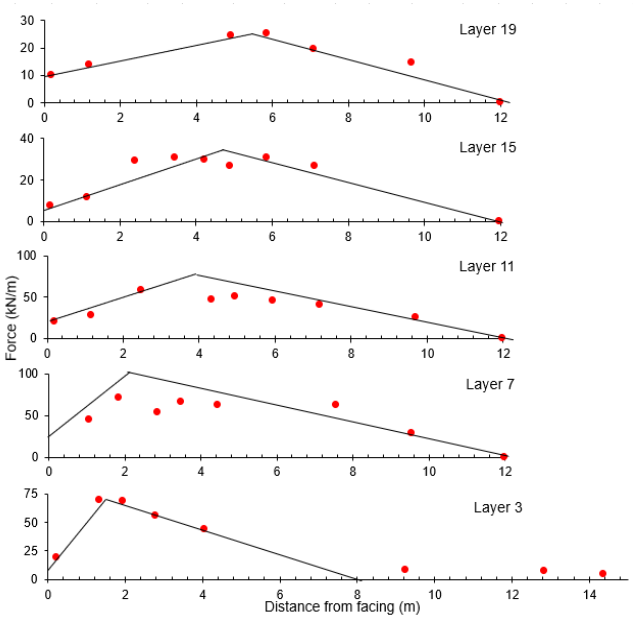


**Fig. 5.** Measured reinforcement load distributions in Minnow Creek Wall (reproduced from Runser et al. 2001).

The WES nylon strip reinforced wall is a rare occurrence where the wall failure can be attributed to pullout. The failure of the wall occurred due to pullout after reaching a wall height of 3.05 m. Fig. 6 shows the resistance and demand curves obtained using the SRI method. Compared to the steel strip wall, relatively low reinforcement stiffness leads to a slow development of resistance compared to the sharp increase in resistance observed in the steel strip reinforced wall. As a result, the nylon strip wall requires a larger displacement to reach equilibrium, which is greater than the displacement required to mobilize the active soil resistance. This constitutes to the pullout failure of the reinforced soil mass.

Two WES walls demonstrate the importance of reinforcement stiffness and its influence on the failure mechanism. For example, in the absence reinforcement stiffness in the formulation, the existing methods would predict pullout failures in both walls. In contrast, the SRI method correctly predicted the failure of the nylon strip reinforced wall; more importantly, the non-failure of the steel strip reinforced wall prior to surcharging. Besides explaining the failure modes, these demand/resistance plots can also explain the ductile or brittle behaviours observed in structures reinforced with different reinforcement types.

.

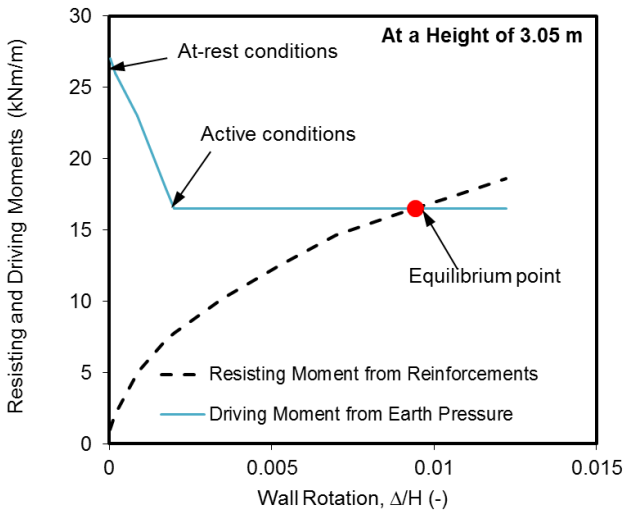


**Fig. 6.** Resisting and driving moments calculated for the nylon strip reinforced WES wall at height of 3.05 m.

Despite the differences in reinforcement types, the SRI method demonstrates that fundamental wall behaviours are similar in these two walls if the soil-reinforcement interaction is considered. This is a vital observation since SRI method does not require to assign different design parameters (e.g., lateral earth pressure coefficients) or adopt a different design method for these two walls as recommended in existing design codes and standards. Instead, using the correct reinforcement stiffness and interface friction angle, the behaviours of MSE walls with different reinforcement types can be explained

The SRI method shall not be considered as a working stress nor as a limit equilibrium-based method. For example, it is not required for all reinforcements and soil to reach their limit state at once as required in limit equilibrium-based method which is not a realistic assumption especially in walls with inextensible reinforcements. As evident in the WES steel strip reinforced wall, certain reinforcements can reach their maximum capacity even under working stress conditions. As the loading is increased, additional resistance is provided by the remaining reinforcements and soil. The SRI method can estimate the reinforcement loads under all stages of loading ranging from working stress conditions to ultimate state.

## Issue 4: Unique Wall Configurations and Ability to Optimize

The empirical methods can only be applied if the wall in question falls within the database that was used to calibrate the model. With walls designed to greater heights and different reinforcement configurations, the applicability of empirical methods is constrained. In comparison, under working stress conditions, Weerasekara et al. (2018a) demonstrated that SRI method can estimate the maximum reinforcement

load in steel strip reinforced walls using known theories without relying on empirical parameters calibrated from instrumented walls. Unlike empirical methods, each input parameter used in the SRI model can be verified by using independent tests.

Solely from an internal stability standpoint, the SRI method shows the potential for using different reinforcement lengths and strengths for improving the overall factor of safety or optimize the design, as opposed to using uniform reinforcement lengths irrespective of the actual design needs. For example, in the case of WES steel strip wall, the overall load carrying capacity of the wall can be increased by (a) using longer reinforcements in the upper layers and (b) strengthening the facing connections or reduce the demand in the bottom layers by decreasing the spacing between reinforcements. This example further demonstrates that shorter reinforcement lengths can be utilized in the bottom reinforcements as the mobilized length is less than the upper reinforcements. It is unfortunate if limitations in the database prevents implementation of measures to increase the robustness and reduce the construction cost.

In certain situations, accommodating uniform reinforcement lengths can become an expensive design proposition if competent soil or bedrock is to be excavated and removed to accommodate the reinforcement length. If the external stability requirements are satisfied, there is no basis to undertake such excavations such that the newly designed wall falls into the database used for the calibration of the design method. FHWA (Berg et al (2009) allows shortening of the bottom reinforcements to minimize excavation requirements if the wall is founded on rock or competent foundation soil. In such situations, for analysis purposes, FHWA recommends dividing the wall into rectangular sections of uniform lengths. It is unclear if such conditions can be accommodated by the empirical design method since the wall configuration may fall outside the database used for calibration of the method. Furthermore, for each wall section, pullout calculations are performed for each reinforcement layer; thus, the same limitations discussed in the preceding sections will prevail. Comparatively, the SRI method provides a rational basis to accommodate truncated reinforcements at the base after considering realistic failure modes for the entire soil mass.

Likewise, when the reinforcement length is limited by vertical or horizontal obstructions (e.g., manholes, utilities, culverts), the SRI method provide a framework to estimate the impact of the shorter reinforcement length. As the overall factor of safety is not necessarily depends on the weakest reinforcement, reduced contribution from a shorter reinforcement can be compensated by making changes to the remaining layers (i.e., using stiffer and/or longer reinforcements). FHWA (Berg et al (2009) also recommends the surrounding reinforcement layers be designed to carry the additional load which would have been carried by the shortened reinforcement(s). However, there are concerns related to the implementation of this recommendation as the existing design methods fail to consider a realistic failure mechanism and overall factor of safety is still governed by the weakest layer. In addition, when attempting to compensate for vertical and horizontal obstructions, effectiveness of closely spaced reinforcements is questionable when using tributary area based methods - see further discussions in the next section.

## Issue 5: Tributary Area Based Framework

While SRI method does not follow the tributary area concept, other design methods calculates $P_{max}$ as the product of the contributory area and average horizontal stress acting on that area. It should be reminded that this tributary area concept is only a simplification for the complex soil-reinforcement interaction occurring in MSE walls. The shortcoming of the tributary area method may not be readily apparent in walls with equally spaced reinforcements. The difference between tributary area methods and SRI method can be demonstrated using the following hypothetical example. The wall shown in Fig. 7a has three layers of continuous reinforcements with uniformly distributed layers. For an assumed horizontal earth pressure distribution, the tributary area method will estimate the smallest and largest tensile loads in reinforcement layers A and C, respectively. For comparison, a wall with closely spaced reinforcements can be considered as shown in Fig. 7b. The separation between reinforcements can be nominal such that frictional resistance of each reinforcement is not impacted by the neighbouring reinforcements. If the wall is in equilibrium, tributary area methods will estimate a very small tensile load in reinforcement layer B due to the small tributary area, while relatively large reinforcement loads are estimated for reinforcement layers A and C. In comparison, the SRI method will estimate similar tensile forces in all three reinforcement layers as they experience approximately similar vertical overburden stress (i.e., friction forces) and elongation to achieve displacement compatibility. It can be argued that SRI model predictions are more realistic although there are no numerical modelling or test walls constructed to verify the load distributions when reinforcements are spaced close to each other.

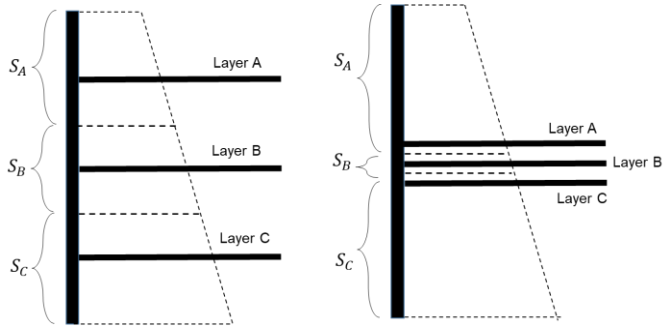


**Fig. 7.** Tributary areas for two hypothetical wall configurations (a) uniformly and (b) closely spaced reinforcements.

## Issue 6: Impact of Wall Toe Resistance

Several studies have highlighted the importance and influence of toe resistance on the magnitude and distribution of reinforcement loads (Huang et al. 2010; Leshchinsky and Vahedifard, 2012; Ehrlich and Mirmoradi, 2013). The reduced reinforcement load near the wall base can be attributed to the toe resistance generated from the soil embedment and friction. The toe resistance is not explicitly mentioned in existing design methods although it can be argued that it is implicitly considered since the design methods were developed from measurements obtained from actual instrumented walls where the toe resistance would have impacted the measurement. However, the toe resistance built into these empirical methods cannot be quantified. As a result, it is not possible to determine whether such magnitude of toe resistance would exist in a newly designed wall or allow the designer to adjust the toe resistance depending on the site conditions. In contrast, the SRI model allows the toe resistance to be quantified and adjusted if required.

According to the database compiled by Allen and Bathurst (2003), the normalized $P_{max}$ distribution in walls with extensible reinforcements is trapezoidal with reinforcements near the bottom experiencing very small tensile load. Comparatively, in walls with inextensible reinforcements, much larger contribution is provided by the bottom reinforcements resulting in a more triangular shaped normalized $P_{max}$ distribution. With inextensible reinforcements, the wall will reach its force equilibrium at a much smaller displacement/rotation. Therefore, a smaller soil resistance is mobilized at the toe of the wall; hence, a significant reduction in tensile load is not expected compared to reinforcements in the upper layers. This behavior is analytically explained using the SRI method.

## Issue 7: Extensibility of Reinforcement and Uniqueness of $P_{max}$ Distribution

The current design methods require the lateral earth pressure distribution to be pre-determined based on the extensibility of the reinforcement. For this purpose, reinforcements are classified either as extensible or inextensible based on the material type regardless of the actual elongation experienced by the reinforcement. Even if the same reinforcement is used in every layer, as evident in instrumented walls, reinforcements at different depths will experience different reinforcement strains such that extensible and inextensible conditions can coexist in the same wall. For example, this is evident in the database compiled by Allen and Bathurst (2003) where small strains have been measured in the bottom and upper reinforcement layers even when the wall is reinforced with extensible reinforcements. A polymer reinforcement located at a shallow depth may not experience a large elongation because the interface friction is not sufficient to develop large strains in the reinforcement. Likewise, an extensible reinforcement placed at the bottom of the wall may not develop significant strain as it is not required to elongate significantly if the wall is rotating about its base. Although some attempts have made to classify reinforcement extensibility by comparing against the soil stiffness, preceding sections indicate the limitations of using such approaches as the extensibility depends on many other factors. For example, British Standards (BS8006) recommends using the Tie-back Wedge method for walls with reinforcement strains exceeding than 1% and Coherent Gravity method for strains below this limit. It is unclear how a unique value of 1% is selected as the threshold for deciding significantly different lateral earth pressure distributions and design methods. For certain polymeric reinforcements with high strength and stiffness, it is uncertain if the reinforcement should be treated as extensible or inextensible. For example, Miyata et al. (2018) had to conduct a separate study to confirm that polyester straps should be considered as an extensible reinforcement in the Simplified Stiffness method.

In contrast, the SRI method does not require the reinforcement extensibility to be predetermined to decide the lateral earth pressure distribution. Most importantly, the SRI method shows that behaviors of extensible and inextensible reinforcements are fundamentally similar. It is not required to adopt different design parameters or lateral earth pressure distributions if the soil-reinforcement interaction is properly accounted. If required, normalized $P_{max}$ distributions can be obtained from the SRI method as an output. As indicated in Weerasekara et al. (2017), the results are consistent with different shapes of $P_{max}$ distributions observed in full-scale instrumented walls with extensible and inextensible reinforcements.

Furthermore, the SRI method shows that the normalized $P_{max}$ distribution measured under working

stress conditions will not remain the same at all stages of loading, including the ultimate state. For example, using the results of an instrumented wall completed at the Royal Military College of Canada (RMCC), Weerasekara et al. (2017), demonstrated that the normalized reinforcement load distribution obtained before surcharging is approximately similar to the trapezoidal load distribution considered in the original version of the K-Stiffness method where the reinforcement loads are small at the top and bottom (see Fig. 8). However, as the surcharge is increased up to failure, the relative contribution from the upper reinforcements have increased considerably causing the shape of the $P_{max}$ to change. In comparison, in the WES steel strip wall, the normalized $P_{max}$ distribution is changed slightly from its original shape as the wall is surcharged. These behavioral differences can be explained using the SRI method by considering the soil-reinforcement interaction and boundary conditions.

## Issue 8: Contradictions with Known Theories

In certain instances, the existing design methods may appear to contradict known soil mechanic theories. The SRI method can demonstrate that such conclusions can arise due to erroneous interpretation of results using frameworks that fail to recognize the soil-reinforcement interaction. For example, for the development of the Coherent Gravity method, Baquelin (1978) suggested that the at-rest lateral earth pressure will prevail near the top of the wall which will decrease with depth until active earth pressure is reached at 6 m below the top of the wall. Although this interpretation is consistent with the back-calculated lateral earth pressure coefficients based on tributary area based methods, this contradicts other experimental and numerical investigations conducted on lateral earth pressures (e.g., Chang, 1997; Kezdi, 1958). Typically, the lateral earth pressure coefficient is expected to be smaller at the top compared to the bottom if the wall is rotating about its base as the largest deformations are expected at the top. This confusion can be explained using the SRI method, which can show that the back-calculated lateral earth pressure coefficient in the Coherent Gravity method is an outcome of the soil-reinforcement interaction and not a reflection of the actual lateral earth pressure coefficient; hence, there is no contradiction.

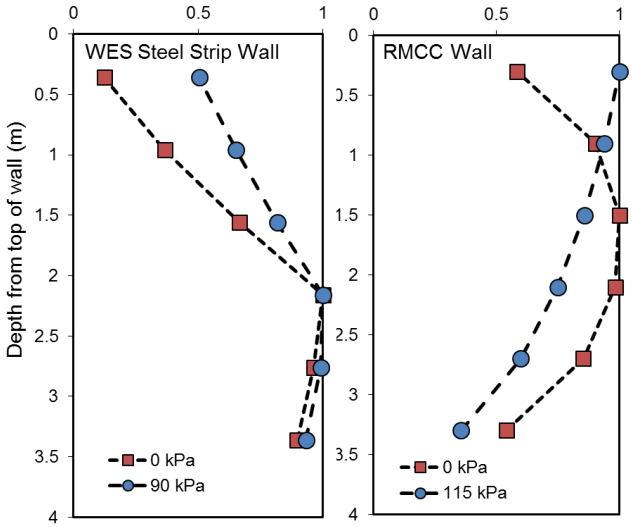


**Fig. 8.** Distributions of normalized maximum reinforcement loads with depth before surcharging and immediately before failure for (a) RMCC wall and (b) WES steel strip wall.

The SRI method can provide analytical explanations to some of the characteristics observed in instrumented walls. Besides simple observations such as the differences in displacements measured in walls with inextensible and extensible reinforcements, the SRI method can explain more complex behaviors such as the differences in normalized $P_{max}$ distributions under working stress conditions when extensible and inextensible reinforcements are utilized. Furthermore, using the pullout tests conducted by Jayawickrama et al. (2013) on ribbed steel strips, Weerasekara et al. (2017), demonstrated how observed trends in $F^*$ with depth can be explained using known soil mechanic theories (see Fig. 9). Test details and input parameters used in the prediction are summarized in Weerasekara et al. (2017); therefore, not repeated herein for brevity. Note that $F^*$ parameter in the Coherent Gravity method is related to $T_1$ in the SRI Friction model especially when inextensible reinforcements are concerned.

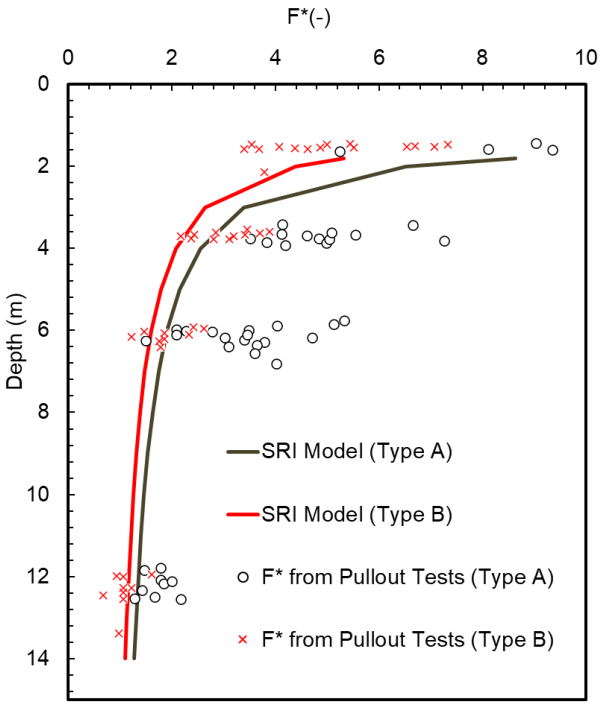


**Fig. 9.** *F** values estimated from the SRI Friction model and measured from pullout tests conducted on steel ribbed steel strips (adopted from Jayawickrama et al. 2013).

## Summary

The SRI method relies on a vastly different analytical framework to assess the internal stability of MSE walls compared to the existing empirical design methods that depends on the tributary area concept. The paper highlighted several limitations of existing design methods and how those can be overcome using the SRI method, and they are summarized below:

- The greatest benefit of the SRI method is in the ability to estimate a more reliable factor of safety and ultimate load carrying capacity as opposed to assuming that the lowest factor of safety calculated for each reinforcement is equal to the factor of safety of the entire wall. The shortcoming of this assumption is more apparent in walls reinforced with inextensible reinforcements. The current design methods such as the Simplified Stiffness, Coherent Gravity and AASHTO Simplified methods have been validated only under working stress conditions. To demonstrate that a design method can achieve a reliable factor of safety (or capacity/demand ratio as per limit state design), it should also be capable of predicting the ultimate state accurately. Without a reliable method to estimate the mobilization of tensile force along the reinforcement and load transmitted to the facing connection, it is not possible to estimate the ultimate state. Although the SRI method can estimate the factor of safety of each reinforcement layer and for each of the three failure modes, those should not be relied upon to determine the factor of safety of the entire soil mass due to limitations explained in this paper.
- The paper explained key limitations in estimating the pullout resistance using the FHWA approach (Christopher et al. 1990) and assumption that load transmitted to the facing is similar to $P_{max}$ that occurs elsewhere. Using of reinforcement stiffness in the soil-reinforcement interaction computation, the SRI method provides an improved framework to estimate the tensile load distribution and load transmitted to the facing connection.
- In inextensible reinforcements, often the tensile force is mobilized along the entire reinforcement length even under working stress conditions (i.e., factor of safety of unity), which does not reflect the minimum factor of safety targeted by the designer using the current design methods. However, the SRI method demonstrates that this condition alone is not sufficient to cause failure of the entire wall. Additional resistance is provided by the remaining reinforcement layers and soil. Surcharging may cause the bottom reinforcements to reach their tensile capacity at the facing connection. In such situations, the wall failure is caused by the combination of pullout of the upper reinforcements and tensile rupture of the bottom reinforcements at the facing connection. This complex failure mode cannot be simulated using the existing design methods.
- The SRI method facilitates design optimization by utilizing non-uniform reinforcement lengths and allowing walls with different heights and configurations be designed as the analysis method is not constrained by the database used for calibration. The method also provides a rational framework to design for vertical and horizontal obstructions and justify non-uniform reinforcement configurations in lieu of excavating and removing competent bedrock or soil to achieve a uniform reinforcement length.
- The SRI model allows the toe resistance to be quantified and allow the designer to adjust it to suit the field conditions. In comparison, toe resistance built into the existing design methods cannot be quantified or modified to match the site conditions.
- The SRI method does not require the reinforcement extensibility to be predetermined to decide the shape of $P_{max}$ distribution with depth. In addition, it is incorrect to assume that $P_{max}$ distribution will remain the same as the working stress conditions when the loading conditions change.

- The SRI method demonstrates that wall behaviors can be explained using known theories and conventional input parameters without resorting to an empirical approach. The known theories can be used to explain the observed behaviors without any contradictions.
- The SRI method demonstrates that behaviors of extensible and inextensible reinforcements are fundamentally similar if the soil-reinforcement interaction is properly accounted. As a result, the SRI method can explain different reinforcement load distributions, ductility/brittleness behaviors, observed failure modes, etc. In essence, there is no reason to use vastly different design methods and empirical design parameters depending on material used for reinforcing.

Similar to other soil-structure interaction problems, the SRI method can be implemented in the allowable stress design domain only. Any alteration to the input parameters using resistance factors could alter the failure mechanism. The input parameters should be as realistic as possible because it is not straightforward to determine if the select input parameter will result in a conservative design. It is appropriate to conduct parametric analysis to determine the robustness of the design.

One of the drawbacks of the SRI method is that the wall deformations estimated using this method are considerably smaller than those measured instrumented walls especially if extensible reinforcements are utilized. It is important to note that displacements estimated using the SRI model are associated with the strain in the reinforcements. Any slack in the reinforcement, deformations in the soil mass and bulging of the facing will result in additional deformations which cannot be accounted using the SRI method. Furthermore, the analytical formation in the SRI method cannot model the connection load that may develop from downward movement of backfill immediately behind the facing.

## References


AASHTO. 2020. LRFD Bridge Design Specifications. 9th Edition, American Association of State Highway and Transportation Officials, Washington, D.C.

Al-Hussaini, M., and Perry, E. B. 1978. Field experiment of reinforced earth wall. Journal of Geotechnical Engineering Division, ASCE, 104(3): 307–322.

Allen, T. M., and Bathurst, R.J. 2015. Improved simplified method for predictions of loads in reinforced soil walls. Journal of Geotechnical and Geoenvironmental Engineering, 141(11): http://dx.doi.org/10.1061/(ASCE)GT.1943-5606.0001355.

Allen, T. M., and Bathurst, R.J. 2003. Predictions of reinforcement loads in reinforced soil walls. Revised Report No. WA-RD 522.2, Washington State Department of Transportation (WSDOT), Olympia, Washington.

Allen, T. M., Bathurst, R. J., Holtz, R. D., Lee, W. F., and Walters, D. L. 2004. A new working stress method for prediction of loads in steel reinforced soil walls. Journal of Geotechnical and Geoenvironmental Engineering, 130(11): 1109 – 1120.

ASTM. 2001. Standard test method for determining tensile properties of geogrids by the single or multi-rib tensile method. D6637, West Conshohocken, Pennsylvania.

Baquelin, F. 1978. Construction and Instrumentation of Reinforced Earth Walls in French Highway Administration. ASCE, Pittsburgh, pp. 186–201.

Bathurst, R.J, Huang, B., and Allen, T.M (2012). LRFD calibration of the ultimate pullout limit state for geogrid reinforced soil retaining walls. International Journal of Geomechanics. 12: 399-413. 10.1061/(ASCE)GM.1943-5622.0000219.

Berg, R.R. Christopher, B.R., Samtani, N.C. 2009. Design and construction of mechanically stabilized earth walls and reinforced soil slopes – Volume 1, Publication No. FHWA-NHI-10–024, U.S. Department of Transportation, Federal Highway Administration, Washington, D.C.

Bolton. M. D. 1986. The strength and dilatancy of sands. Geotechnique, 36(1): 65-78.

Canadian Standards Association. 2019. Canadian Highway Bridge Design Code (CHBDC). CSA Standard S6:19, Canadian Standards Association, Toronto, Canada.

Chang, M-F. 1997. Lateral earth pressure behind rotating walls, Canadian Geotechnical Journal, 34: 498-509.

Christopher, B. R., Gill, S. A., Giroud, J.-P., Juran, I., Mitchell, J. K., Schlosser, F., and Dunnicliff, J. 1990. Reinforced soil structures, Volume 1: Design and Construction Guidelines. Federal Highway Administration (FHWA), Report No. FHWA-RD-89-043, Washington, D.C.

Damians, P., Bathurst., R.J, Josa, A., and Lloret, A. (2015). Numerical analysis of an instrumented steel reinforced soil wall, ASCE International journal of Geomechanics, 15(1): p. 04014037.

Ehrlich, M., and Mirmoradi, S. H. 2013. Evaluation of the effects of facing stiffness and toe resistance on the behavior of GRS walls. Geotextiles and Geomembranes, 40(1): 28 – 36.

Holtz, R. (2017). 46th Terzaghi Lecture: Geosynthetic reinforced soil: From the experimental to the familiar. Journal of Geotechnical and Geoenvironmental Engineering. 143. 10.1061/(ASCE)GT.1943-5606.0001674.

Huang, B., Bathurst, R. J. Hatami, K., and Allen, T. M. 2010. Influence of toe restraint on reinforced soil segmental walls. Canadian Geotechnical Journal, 47(8): 885 – 904.

Huang, B and Bathurst, R. J. (2009). Evaluation of soil-geogrid pullout models using a statistical approach. Geotechnical Testing Journal, 32. 10.1520/GTJ102460.

Jayawickrama, P., Surles, J.G., Wood, T.D., Lawson, W.D. 2013. Pullout resistance of mechanically stabilized reinforcement in backfills typically used in Texas. Research Report No. FHWA/TX-13/0-6493-R1, Vol. 1, Texas DOT, Austin, Texas.

Juran, I., Guermazi, A., Chen, C.L. and Ider, M.H. (1988). Modelling and simulation of load transfer in reinforced soil: Part 1, International Journal of Numerical Analytical Methods in Geomechanics, Vol.12, pp. 141-155.

Kezdi, A. 1958. Earth pressure on retaining wall tilting about the toe. Proceedings of the Brussels Conference on Earth Pressure Problems, Vol. 1, pp. 116–132

Leshchinsky, D., and Vahedifard, F. 2012. Impact of toe resistance in reinforced masonry block walls: Design dilemma. Journal of Geotechnical and Geoenvironmental Engineering, 138(2): 236-240.

Miyata, Y., Bathurst, R.J., and Allen, T.M. 2018. Evaluation of tensile load model accuracy for PET strap MSE walls, Geosynthetic International, 25(6): 656-671.

Runser, D. J., Fox, P. J., and Bourdeau, P. L. 2001. Field performance of a 17 m-high reinforced soil retaining wall, Geosynthetic International, 8(5): 367–391.

Schlosser, F. 1978. History, current development, and future developments of reinforced earth. Symposium on Soil Reinforcing and Stabilizing Techniques, Sydney, pp. 5–28.

Weerasekara, L. 2018a. Steel strip reinforced soil walls at working stress conditions, In proceeding of 71st Canadian Geotechnical Conference, GeoEdmonton, Edmonton, Canada.

Weerasekara, L. 2018b. Improvements to pullout failure estimation in MSE walls, In proceeding of 71st Canadian Geotechnical Conference, GeoEdmonton, Edmonton, Canada.

Weerasekara, L., and Wijewickreme, D. 2010. An analytical method to predict the pullout response of geotextiles. Geosynthetic International, 17(4): 193-206.

Weerasekara, L., Hall, B.E., and Wijewickreme. 2017. A New Approach for Estimating Internal Stability of Reinforced Soil Structures, Geosynthetic International, 24(4): 419 – 434.

# 3D Seismic Numerical Modeling of Infrastructure on Liquefiable Soils - Soil-Structure Interaction and Soil-Cement Grid Modeling

Viet (Victor) Tran, PhD, P.Eng., PMP
Principal Geotechnical Engineer, FECON Geotechnical Ltd., Port Coquitlam, BC
Email: victor@fecongeo.com

**ABSTRACT** 3D seismic numerical modeling using the FLAC3D program was carried out for three representative cases: 1) an embankment dam on a liquefiable layer, 2) a berth structure consisting of quay wall supported by anchor walls and tie-rods subject to soil liquefaction, and 3) a long pier consisting of vertical and battered steel pipe piles supporting deck structures. Soil-cement grids were considered in case 2 to mitigate liquefaction effects. The P2PSAND soil constitutive model, specifically designed for 3D modeling of liquefied soils, was employed to represent liquefiable soils. The P2PSAND model is based on the framework of the DM04 model and is a critical-state compatible and plasticity model utilizing bounding surface theory. The model can simulate non-linear response, liquefaction triggering and strength reduction of the soils during earthquake. Soil-cement grids of various sizes were modeled in 3D to evaluate the method's efficiency to reduce liquefaction and provide insight into the performance of the system. The structures were simulated with their 3D geometries to best evaluate the 3D soil and structure interaction. The effects of the earthquake direction, seismic wave propagation to surface, and sizes of soil-cement grids were also presented and discussed.

## Introduction

Embankments and marine structures are often located on steep river or marine slopes where subsurface soils can become liquefiable. These conditions frequently lead to significant deformations in both the soil and the structures. Typical design may involve 2D geotechnical seismic ground deformation analysis followed by seismic structural design. Post-seismic soil deformation along with p-y curves are often provided to the structural engineer to account for the kinematic effects. However, this structural assessment is often decoupled from the geotechnical analysis. While this process is straightforward, the ground deformation and the relatively simplistic p-y curves do not comprehensively capture the intricate soil-structure interaction during earthquakes. Moreover, 2D geotechnical modeling, although practical, often fails to adequately represent the three-dimensional (3D) characteristics of structures and ground reinforcement.

There are several soil constitutive models that have been widely used for soil liquefaction modeling. Nevertheless, most of these models are limited to two dimensions. Recent advancements have introduced new 3D soil models, such as P2PSand, which is available within the FLAC 3D program. This study aims to leverage the capabilities of this 3D soil model for simulating liquefaction. By utilizing the FLAC 3D program, this research will delve into the realm of 3D soil and structure interaction, shedding light on the seismic response of both soils and structures.

## Soil Constitutive Model

Multiple soil models have been developed to simulate the soil liquefaction of sand-like materials in geotechnical earthquake engineering. Among the prominent models are the PDMY model (Elgamal et al., 2003; Yang et al., 2003), DM04 model (Dafalias and Manzari, 2004), SANISand model series (Taiebat and Dafalias, 2008; Yang et al., 2022), NTUA sand model (Papadimitriou and Bouckovalas, 2002), UBCSand model (Beaty and Byrne, 2011), and PM4Sand model (Boulanger and Ziotopoulou, 2015).

In practical geotechnical earthquake modeling, two widely utilized 2D constitutive models are UBCSAND and PM4SAND. These models are available in several geotechnical software programs, although they are exclusively applicable to 2D plane strain conditions. More recently, to address the growing need for a 3D soil model capable of simulating soil behavior under seismic conditions, the P2PSAND model was introduced by Cheng and Detournay (2021).

The P2PSand model stands as a practical 3D two-surface plastic constitutive model founded on the DM04 model. This model encompasses both the theoretical robustness of the PM04 model and the pragmatic features of the UBCSand and PM4Sand models. Furthermore, the P2PSand model has been integrated into the commercially available geotechnical program FLAC3D. For further theoretical insights into the model, readers are directed to Cheng and Detournay (2021).

## P2PSand Model Calibration

The model has been numerically calibrated to the liquefaction triggering curve proposed by Idriss and Boulanger (2008) as shown in Figure 1a. The numerical calibration was based on element CDSS (cyclic direct simple shear) test simulation and the CSR (cyclic stress ratio) was calculated based on the shear stress required to reach liquefaction after 15 equivalent cycles. Liquefaction was defined as excess pore water pressure ratio reaching 98% or maximum shear strain reaching 3%. The profiles of CSR versus number of cycles to liquefaction (N) are presented in Figure 1b. Representative DSS stress-strain responses of the P2PSand model are shown in Figure 2. The results are from element CDSS tests under undrained stress-controlled loading conditions.

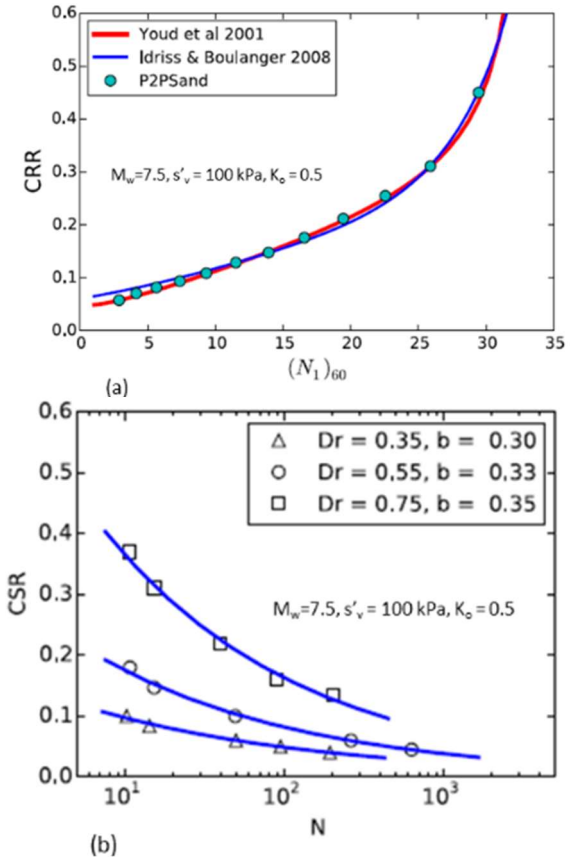


**Fig. 1**. P2PSand model numerical calibration: (a) Liquefaction triggering curve, (b) CSR – N relationship (adopted from Cheng and Detournay, 2021)

The primary input parameters of the P2PSand model are relative density (Dr) and soil densities. The small-strain shear modulus (G) is calculated using the following equation:

[1] $$G = f(D_r)P_a\left(\frac{p'_m}{P_a}\right)^2$$

where: $f(D_r)$=1.24e$^3$$(D_r + 0.01)$, $P_a$ is atmospheric pressure taken as 100 kPa, and $p'_m$ is the soil mean effective stress. The constant volume friction angle $\phi'_{cv}$ of 33 degrees and $K_o$ (the ratio of horizontal effective stress to vertical effective stress at the start of loading) of 0.5 were used. All other parameters are default or internally calibrated.

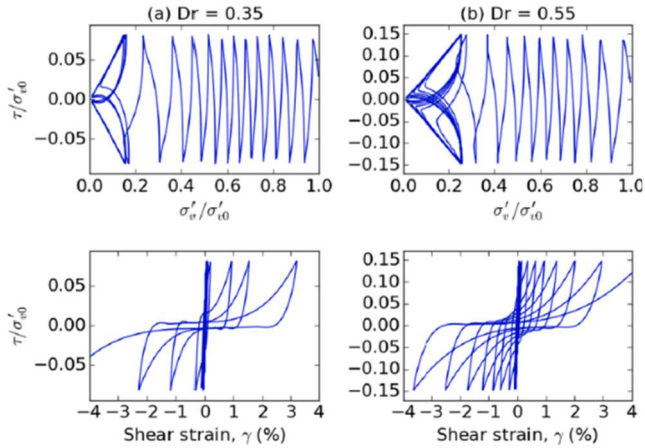


**Fig. 2**. Stress – strain relationship – P2PSand model CDSS testing (adopted from Cheng and Detournay, 2021)

# Case Study 1: Embankment Dam on Liquefiable Layer

## Embankment Model

In this case study, we employed the FLAC 3D program (v7, Itasca Consulting) to model a road embankment situated along a riverbank. The top of the embankment is at El. -15 m. A densified sand and gravel fill with a thickness of 3 m was placed beneath the embankment surface. Below the fill soils, a layer of dense sand extended to El. – 6 m was encountered, which is underlain by a loose sand layer. This loose sand layer has a thickness of 12 m and overlying a sand and gravel layer. Along the riverside, the embankment boasts a slope of 2H:1V, succeeded by a flat bench at an elevation of 0 m, spanning a width of 20 m. A 2H:1V river slope is then extended to reach the riverbed at an elevation of -6 m. A water level set at an elevation of 0 m was considered within the model. The geometrical configuration of the embankment is illustrated in Figure 3.

Particularly noteworthy is the susceptibility of the sand soils, especially the loose sand layer, to liquefaction during seismic events. To capture this behavior, the P2PSAND model was employed for modeling these soil strata. The pertinent soil parameters are detailed in Table 1.

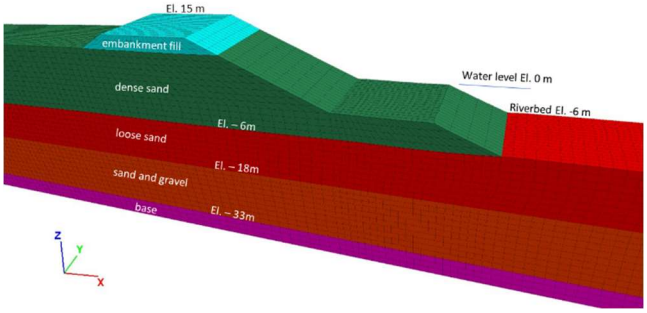


**Fig. 3.** Embankment geometry

**Table 1**. Soil parameters – case study 1

| Soil layer | Unit weight (kN/m$^3$) | Relative Density Dr | Gmax (MPa) |
|---|---|---|---|
| Embankment fill | 20 | 0.85 | Eq. (1) |
| Dense sand | 20 | 0.73 | Eq. (1) |
| Loose sand | 19 | 0.42 | Eq. (1) |
| Sand and gravel | 20 | 0.66 | Eq. (1) |

The FLAC3D model comprises more than 65,000 hexahedral (brick) elements, established through the extrusion of a 2D plane strain model by a distance of 17 m in the out-of-plane direction. Element sizes range from 1 m to 2 m. The model's lateral boundaries were assigned as free field boundaries, while a compliant base condition was implemented at the model base.

The Landers (1992) earthquake was chosen for the modeling. This seismic record was applied at the base of the model in the form of a velocity time-history. The time-history, in turn, was converted into a shear stress time-history to serve as the actual earthquake input. The earthquake's acceleration time-history and spectrum acceleration are depicted in Figure 4.

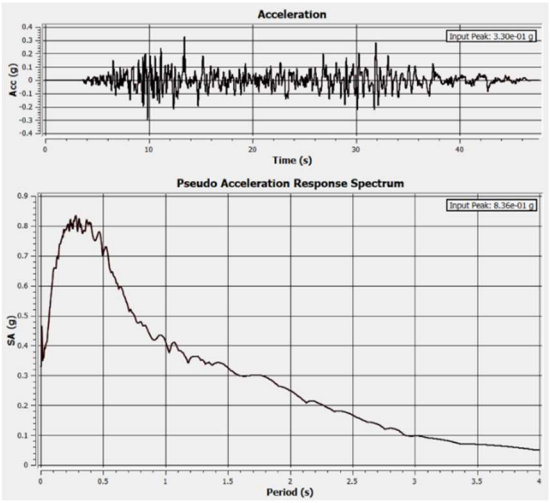


**Fig. 4**. Time-history and acceleration response spectrum of Landers (1992) earthquake

## Modeling Results

The post-seismic ground deformation is shown in Figure 5. The most substantial deformations, reaching approximately 2.4 m, were identified at the lower bench and river slope. Furthermore, lateral deformations of approximately 1 m manifested at the crest of the embankment.

The extent of soil liquefaction, expressed as the excess pore water pressure ratio Ru, is shown in Figure 6. Zones with Ru values larger than 0.9 are indicative of liquefaction. Liquefaction were primarily observed within the loose sand and sand and gravel layers.

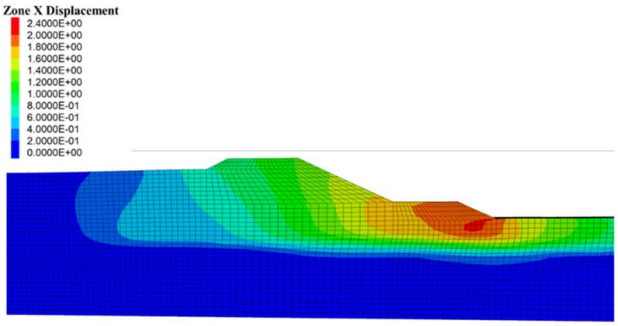


**Fig. 5**. Post seismic embankment deformation

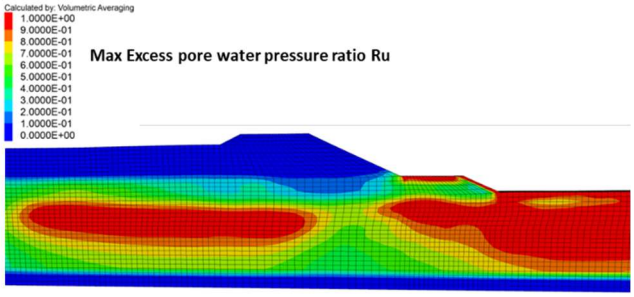


**Fig. 6**. Max excess pore pressure ratio (Ru)

## Comparison of Soil Models

The uniform geometry of the embankment model in the out-of-plane direction lends itself to a comparison of model responses between 2D plane strain and 3D scenarios. Figure 7 depicts the 2D and 3D responses of the P2PSand model, utilizing their respective 2D and 3D versions, by showcasing the time-history of horizontal deformation at the embankment crest. Impressively, the 2D and 3D P2PSand models exhibit strikingly similar outcomes.

Additionally, Figure 7 presents the response of the 2D geometry when using the PM4SAND model. Both the PM4SAND and P2PSand models share the same input parameters and undergo element test

calibration. However, it is noteworthy that the embankment deformation derived from the PM4SAND model slightly exceeds that from the P2PSand model.

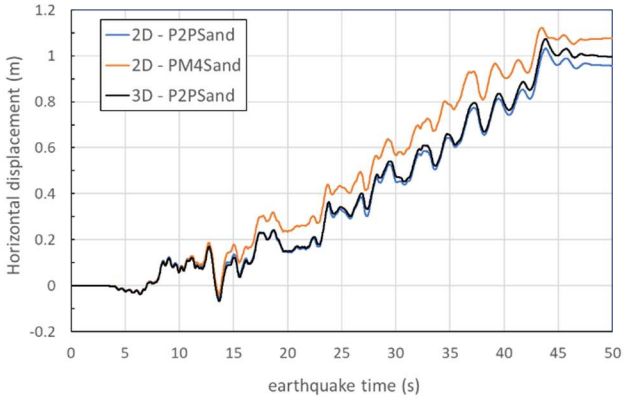


**Fig. 7**. 2D vs. 3D and PM4Sand vs. P2PSand comparisons – horizontal displacements at crest.

## Case Study 2: Anchored Quay Wall

### Geometry

To assess the seismic performance of an anchored combi-wall system, seismic soil-structure interaction analysis was conducted. The combi-wall serves to retain a soil height spanning from an elevation of 5.5 m (top of the wall) to -9 m (dredge level), totaling 14.5 m. Subsurface soil composition encompasses sand fill situated above an elevation of +1 m, underlain by a layer of loose sand, as well as a medium-dense mixture of gravel and sand. Subsequently, these are succeeded by a non-liquefiable stiff silt layer. Notably, during simulated earthquake events, the loose sand layer, and potentially portions of the gravel and sand layers, are prone to liquefaction.

For analysis of the earthquake-induced phenomena, the P2PSAND model was applied to simulate the behavior of liquefiable soils. The soil parameters and the corresponding constitutive models are consolidated in Table 2. Within the model, the water table was positioned at an elevation of +1 m. The geometric configuration of the model is shown in Figure 8.

**Table 2**. Soil parameters – case study 2

| Soil layer | Unit weight (kN/m$^3$) | Relative Density Dr | Gmax (MPa) |
|---|---|---|---|
| Compacted fill | 19 | 0.73 | Eq. (1) |
| Loose sand | 18.5 | 0.35 | Eq. (1) |
| Gravel and sand | 20 | 0.73 | Eq. (1) |
| Stiff silt | 18 | - | 150 |

The quay wall configuration comprises king piles with an outer diameter of 1422 mm and a thickness of 25 mm, constructed from steel pipe piles. These piles extend to the uppermost part of the gravel and sand layer, situated at an elevation of -25 m. Notably, the king piles are spaced with a center-to-center distance of 2.89 m.

Incorporated between the king piles are infill sheets of AZ26-700 type. These sheets extend from the top of the king piles to an elevation of -15 m.

Furthermore, the quay wall is reinforced through an anchor wall system that employs high-strength tie rods of ASDO 500 M125/115 specification. These tie rods establish connections between the king piles and the anchor wall. The anchor wall itself consists of sheet piles of AZ48-700 variety, positioned 30 m behind the quay wall. These sheet piles extend vertically from an elevation of +4 m to -4 m. The interplay of these components constitutes the overall configuration of the structures, as depicted in Figure 9a.

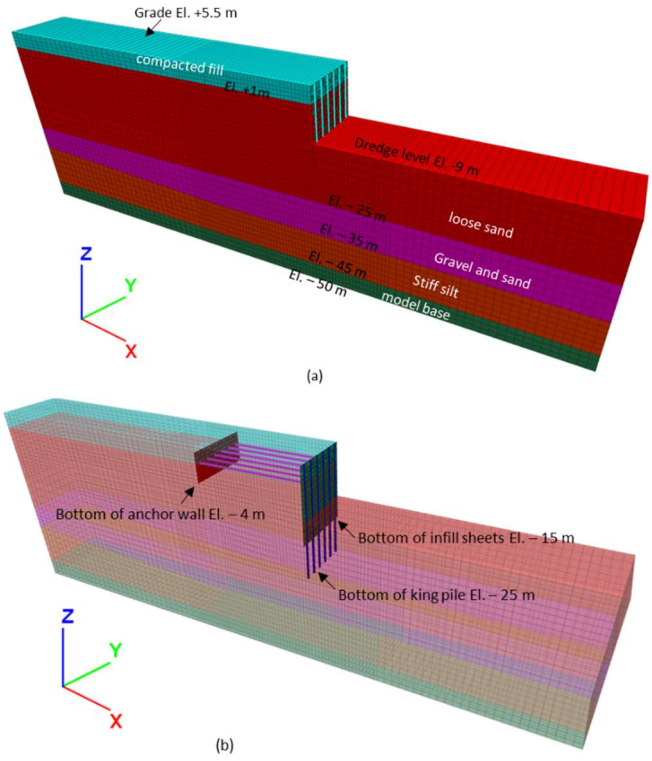


**Fig. 8**. (a) Quay wall geometry with filled zones filled, (b) Model geometry with transparent zones showing structures

## Earthquake Record

The purpose of this study is to demonstrate the capability of 3D modeling of soil-structure interaction modeling under seismic conditions and therefore, only one earthquake Tabas (Iran, 1978) was used as input time-history. The Tabas record and its response spectrum are shown in Figure 9b.

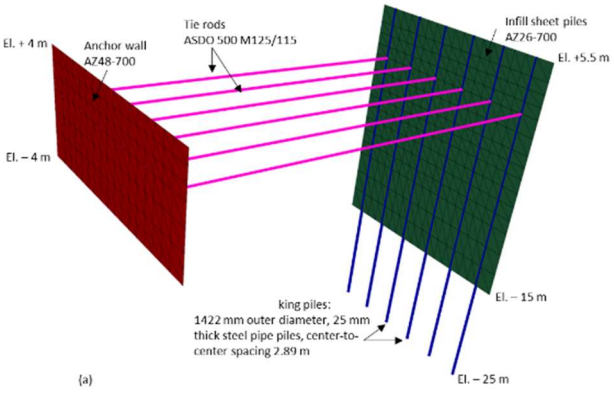


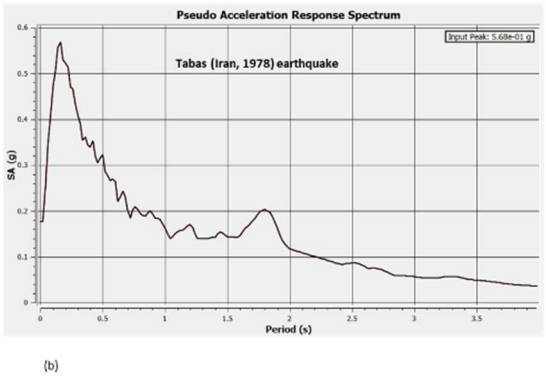


**Fig. 9**. (a) Quay wall structures, (b) Response spectrum of input earthquake record Tabas (Iran, 1978).

## Soil-Structure Interaction

The analysis encompassed coupled soil-structure interaction studies employing FLAC 3D. Hexahedral zones with a mixed discretization scheme were employed to model the soils. The quay wall's king piles were represented using pile elements, while liner elements captured the behavior of the infill sheets and anchor wall. Cable elements were used to simulate the tie rods. An interface friction angle of 17 degrees represented the interaction between soil and structure. The structures themselves were subjected to a full 3D model utilizing their actual properties.

The analysis unfolded in two distinct stages:

Stage 1: A static analysis was conducted to capture pre-earthquake conditions.

Stage 2: A dynamic analysis followed, where the model was subjected to earthquake motion. Shear stress time-histories were applied at the base of the model to replicate the earthquake's effect.

To minimize boundary-related effects, the FLAC model's lateral boundaries were extended on both sides. Lateral boundaries were defined with free-field conditions, while the model base was treated with a compliant base condition. Moreover, the simulation considered the hydrodynamic pressure exerted on the quay wall during earthquake. A surcharge of 12 kPa was applied on the ground surface behind the quay wall.

## Analysis Results - Existing Conditions

Under the existing soil conditions, the soil horizontal deformations at the end of the earthquake and maximum excess pore pressure ratio $R_u$ contours are shown in Figure 10. The results indicate largest soil displacements in the order of 1 m and soil liquefaction (Ru > 0.9) occurred behind the quay wall. The deformations of the quay wall and anchor wall are shown in Figure 11, which indicates a deflection of about 1 m at the top of the quay wall.

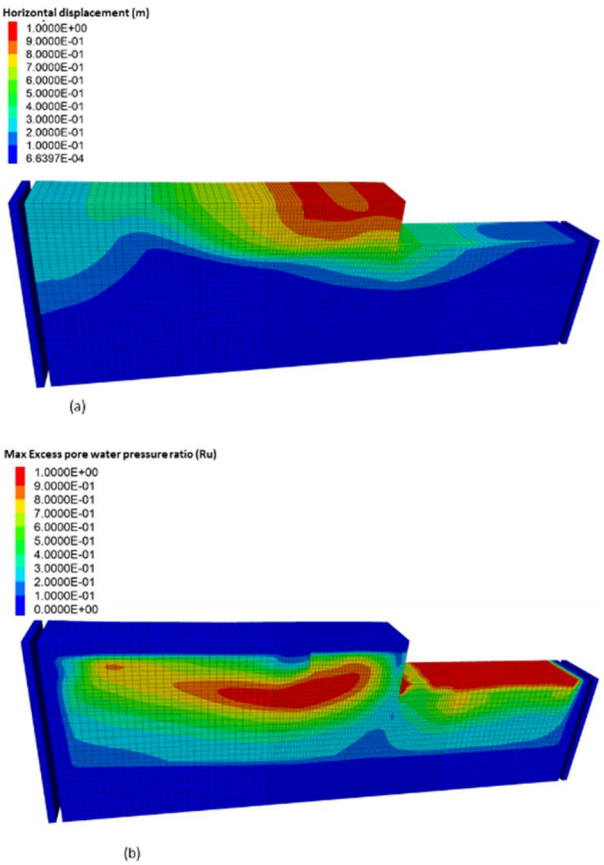


**Fig. 10**. Existing soil conditions (a) Soil horizontal displacement contours (m), (b) Max excess pore pressure ratio (Ru)

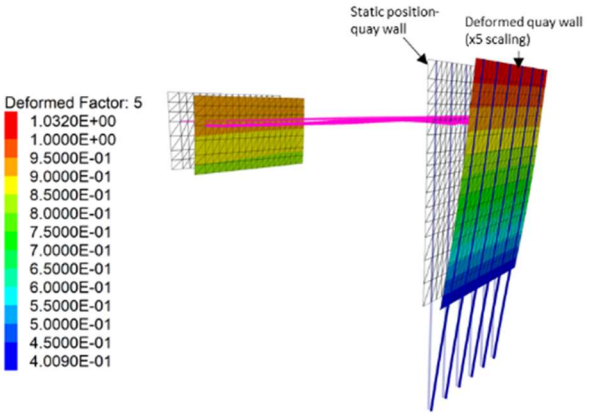


**Fig. 11**. Existing soil conditions - quay wall deformation (m),

## Effects of Earthquake Directions

The impact of earthquake directions was assessed through two distinct cases: one involving the earthquake applied in the X direction (perpendicular to the quay wall, i.e., from behind to in front of the quay wall), and the other involving the earthquake applied in the Y direction (out of the plane direction). Figure 12 provides a visualization of the horizontal displacements observed at the quay wall's top when the earthquake was induced in the X direction. Notably, the quay wall exhibited a deformation of approximately 1.05 m in the X direction, while displaying negligible deformation in the Y direction.

When the earthquake's force acted in the Y direction, the deformation of the quay wall in the Y direction mirrored the ground deformation at the model base. Consequently, the end-of-shaking Y-deformation remained relatively minor. Conversely, horizontal displacements of approximately 0.85 m manifested in the X direction. This degree of displacement is about 80% of the quay wall's deformation when subjected to an earthquake in the X direction.

The substantial quay wall deformation persisted even when the earthquake was directed out of the plane, rather than perpendicular to the quay wall. This can be attributed to the generation of excess pore water pressure within the soils, as showcased in Figure 13 for two points within the loose sand at about 20 and 55 m behind the quay wall. Notably, even when the earthquake was applied out of the plane, a smaller yet still significant pore water pressure was observed.

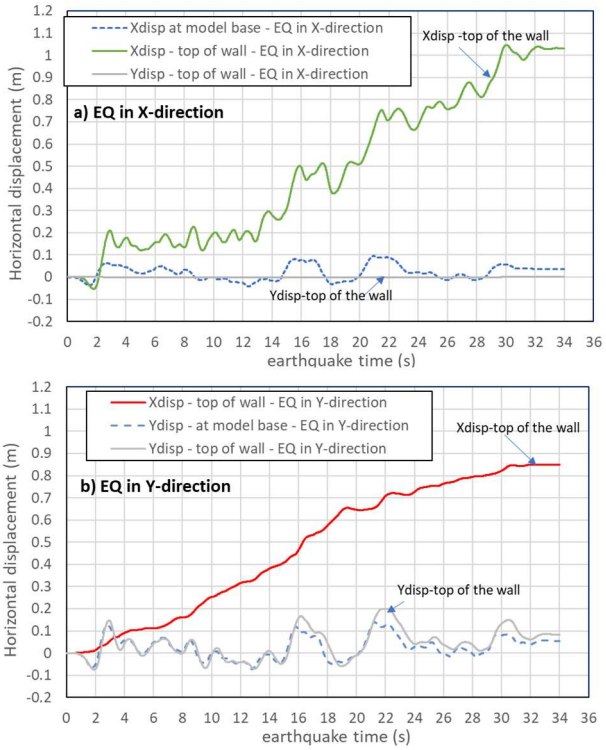


**Fig. 12**. Quay wall deformation time-histories a) Earthquake in the X-direction - onshore to offshore b) Earthquake in the Y-direction – out of plane

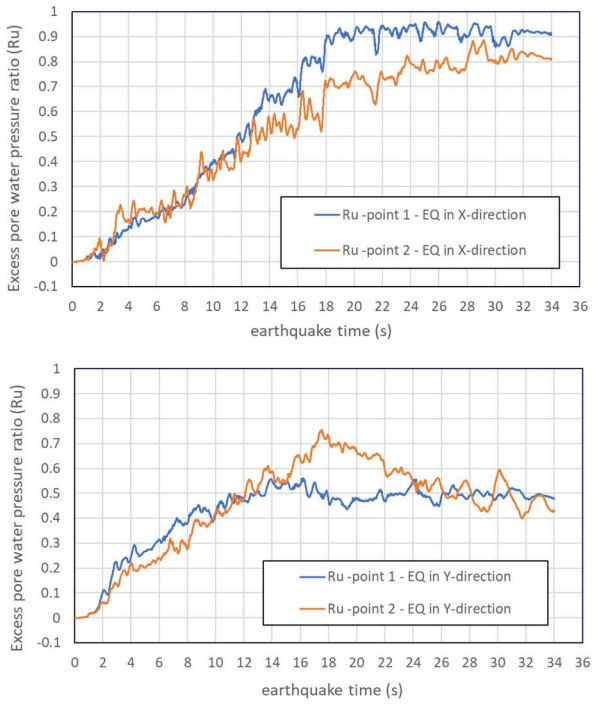


**Fig. 13**. Excess pore water pressure ratio time-histories a) Earthquake in X-direction and b) Earthquake in Y-direction

## Deep Soil Mixing Grids

Initial analyses have revealed substantial soil and structural deformation resulting from seismic activity, raising concerns about whether these deformations meet the practical project's performance-based design criteria. 3D modeling offers a notable advantage in representing real-world 3D deep soil mixing (DSM) grids. This approach contrasts with the conventional simplified 2D zones/columns, which lack the ability to capture the three-dimensional boxing effect.

Within the framework of this study, DSM grids measuring 10 m x 10 m and 7 m x 7 m square boxes were implemented both behind and in front of the quay wall. These grids were positioned beneath the compacted fill layer, situated below an elevation of +1 m in onshore areas, and below the dredge level (at an elevation of -9 m) in offshore areas. Notably, the DSM grids extended from the base of the compacted fill layer to the bottom of the loose sand layer, at an elevation of -25 m. Figure 14 presents a visual representation of the grids.

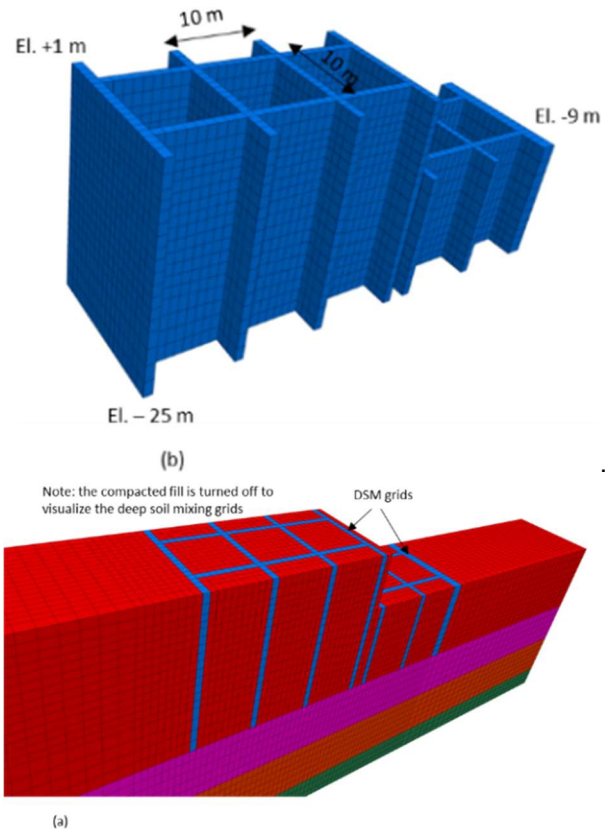


**Fig. 14**. (a) Soil reinforcement using deep soil mixing (DSM) grids, (b) DSM grids 10 m x 10 m

The modeling of these grids was undertaken using a Mohr-Coulomb model, characterized by a shear strength of 750 kPa. This value is derived from a representative unconfined shear strength $q_u$ of 1500 kPa specific to soil-cement mixing. Additionally, the secant modulus $E_{50}$ was set at $300q_u$, and the Poisson's ratio at 0.3.

Upon incorporating soil reinforcement through DSM grids of dimensions 10 m x 10 m, Figure 15 presents the outcomes in terms of soil displacements and Ru contours. Significantly reduced soil displacements, approximately 0.35 m, were projected behind the quay wall. It's noteworthy that no liquefaction was observed within the DSM boxes.

The DSM grids notably introduced a boxing effect, effectively constraining the development of excess pore pressure and soil displacement, particularly within the DSM boxes. This effect contributes to enhanced stabilization.

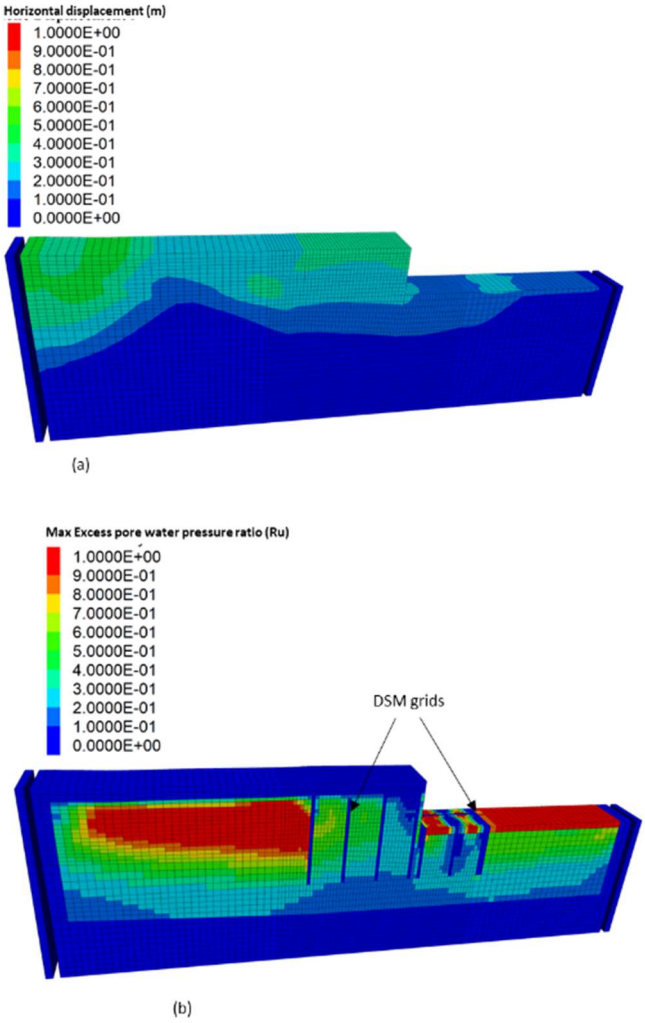


**Fig. 15**. DSM reinforcement 10 m x 10 m boxes (a) soil horizontal displacement contours (m), (b) max excess pore pressure ratio (Ru)

Comparing quay wall displacement time-histories with and without soil reinforcement, Figure 16 showcases the differential outcomes. With DSM grids measuring 10 m x 10 m, the wall displacement amounts to around 0.35 m. On the other hand, employing DSM grids measuring 7 m x 7 m yields a diminished displacement of 0.22 m. These deformations significantly undercut the 1 m estimate attained under existing soil conditions, i.e., without the integration of soil reinforcement.

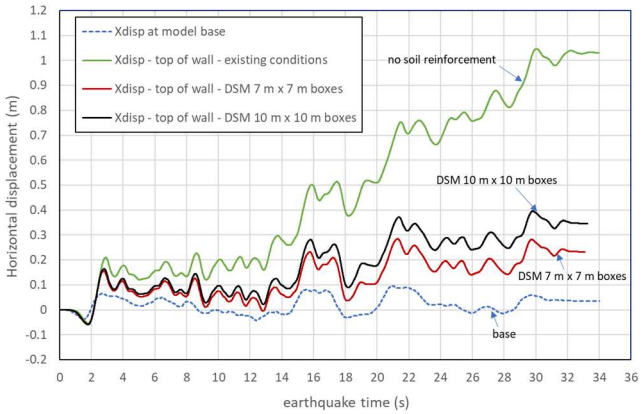


**Fig. 16**. Time-histories of quay wall displacements (top of wall) under existing soil conditions vs. DSM reinforcement conditions

## Spectral Acceleration at Ground Surface

Figure 17 illustrates the response spectra at the ground surface for both the existing conditions and those reinforced with DSM. The measurement point was positioned approximately 10 m behind the quay wall and within an existing soil column, rather than directly above the DSM grids. To provide comparison, the response spectrum of the input motion at the model's base is also incorporated in the figure.

Under the existing conditions, amplification was notably evident across various periods. This amplification extended to the peak ground acceleration (PGA), which was elevated from the input earthquake record's 0.18g to approximately 0.38g.

In contrast, the application of DSM reinforcement yielded a different scenario. For periods shorter than 0.5s, de-amplification occurred, resulting in a PGA of 0.15, slightly below that of the input earthquake record. This observed pattern suggests a reduction in shear stresses within the soil due to the heightened stiffness of the DSM shear boxes.

However, for periods exceeding 0.5s, amplification was observed. Notably, response spectra between the existing soil conditions and those fortified with DSM reinforcement exhibited similarities for periods beyond 0.5s.

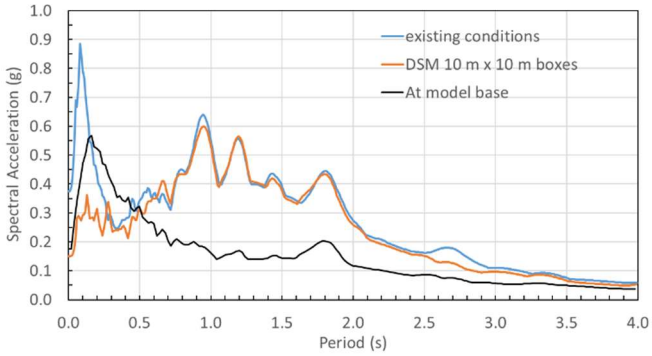


**Fig. 17**. Spectral accelerations at ground surface under existing soil conditions vs. DSM reinforcement conditions

# Case Study 3: Long Pier Structure

## Geometry

In this case study, we examined a long pier structure to assess its post-seismic deformation when subjected to substantial ground deformation along the nearshore slope due to liquefaction. The marine slope originates from the onshore area, characterized by a grade level at an elevation of +6 m. The slope extends towards the ocean, inclined at an approximately 4H:1V (horizontal to vertical) ratio. This slope has been dredged to an elevation of -11 m, positioned approximately 45 m away from the shoreline.

The subsurface soil composition encompasses compacted fill in the onshore region, followed by layers of loose to dense sand. These, in turn, are underlain by a stratum of stiff silt. Figure 18 presents the soil stratigraphy, while Table 3 provides the associated soil parameters.

The dimensions of the pier are approximately 198 m in length and 19 m in width. Notably, the deck's elevation rests at around El. 7 m. Comprising a total of 14 bents spaced 15 m apart, the pier features five bents situated on the nearshore slope. These nearshore bents are supported by a combination of vertical piles and inclined piles at a 1H:4V ratio. The remaining bents are upheld by vertical piles. All piles are steel pipe piles with an outer diameter of 1067 mm and a thickness of 19 mm. These piles extend down to an elevation of -45 m. Each bent is connected by a capping beam with dimensions measuring 1400 W x 1600 H. This beam serves to support the deck, offering an equivalent concrete thickness of 1.5 m. A visual representation of these structures is shown in Figure 18.

The Landers (1992) earthquake, same as that used in case study 1, was used as the input record for seismic soil-structure modeling.

**Table 3**. Soil parameters – case study 3

| Soil layer | Unit weight (kN/m$^3$) | Relative Density Dr | Gmax (MPa) |
|---|---|---|---|
| Compacted fill | 19 | 0.66 | Eq. (1) |
| Loose sand | 18.5 | 0.41 | Eq. (1) |
| Medium sand | 19 | 0.69 | Eq. (1) |
| Dense sand | 19 | 0.78 | Eq. (1) |
| Stiff silt | 18 | - | 150 |

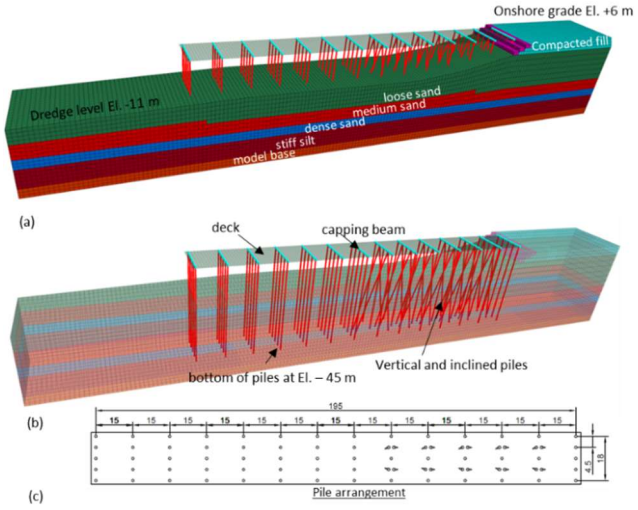


**Fig. 18**. (a) Pier geometry with filled zones filled, (b) Model geometry with transparent zones showing structures, (c) Pile arrangement

## Analysis Results

The outcomes of the analysis are demonstrated through two aspects: soil deformation at the earthquake's conclusion and maximum excess pore pressure ratio Ru contours, shown in Figure 19. Notably, Figure 19a employs a scaling factor of 5 to enhance visualization. Results indicate that the most substantial soil displacements occur along the nearshore slope, reaching magnitudes ranging from 1.5 m to 2 m. Liquefaction, denoted by Ru values exceeding 0.9, were prevalent within the sand layers (Figure 19b). Beyond the slope region, ground deformation diminishes, with values ranging between 0.2 m to 0.4 m in the flat dredged area.

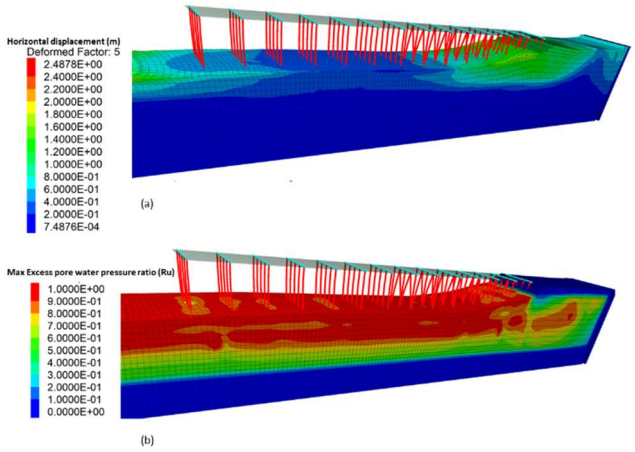


**Fig. 19**. (a) soil horizontal displacement contours (m), (b) max excess pore pressure ratio (Ru)

In Figure 20, the deformations of the structures are delineated. Closer proximity to the nearshore slope is linked to greater pile displacement, contrasting with the situation at the flat dredged area. Nevertheless, due to the interconnection of all piles with capping beams and the deck, which offer significant rigidity along the earthquake direction, pile displacements gravitated toward an intermediate range, approximating 0.5 m. This magnitude notably stands significantly lower than the most considerable soil displacements encountered along the nearshore slope.

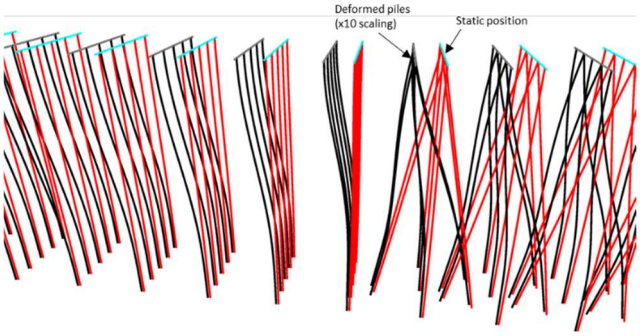


**Fig. 20**. Deformation of the piles

Displacement time-histories, both at the model's base and atop a representative pile, are presented in Figure 21. Importantly, the capping beams and the deck experienced practically identical displacements as the piles.

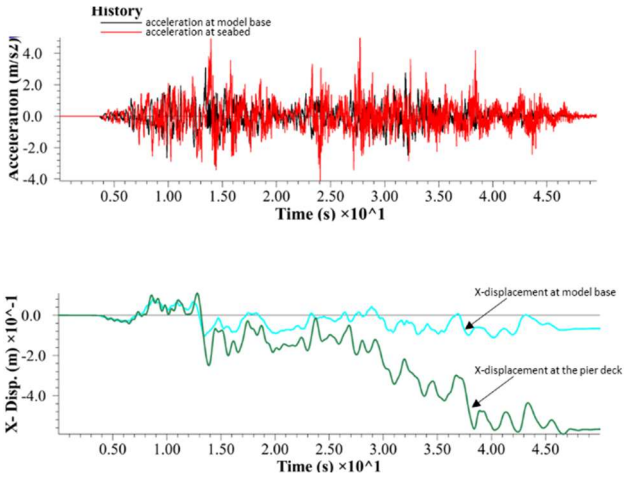


**Fig. 21**. (a) Acceleration time-histories, (b) X-displacement time-histories

## Conclusions

In this study, modeling of seismic response and soil-structure interaction for three distinct cases was conducted through advanced numerical modeling techniques. These cases encompassed an embankment dam on a liquefiable layer, an anchored quay wall system, and a long pier structure. The primary objective was to evaluate the potential impact of seismic events on these structures. The 3D modeling can simulate liquefaction patterns such as development of excess pore water pressure, liquefaction triggering, loss of strength, stiffness reduction and typical stress-strain loops using the 3D P2PSand model. The P2PSand model follows the state-of-the art theorical background and can be calibrated to widely used correlations and laboratory test results.

The application of deep soil mixing (DSM) grids, tailored to 3D geometry, demonstrated a remarkable capacity to restrain excess pore pressure and mitigate soil deformations. Notably, the de-amplification of spectral acceleration in certain periods under DSM reinforcement highlighted its efficacy in decreasing shear stresses within the soil, leading to improved seismic performance.

Furthermore, the investigation of a long pier structure emphasized the susceptibility of marine slopes to seismic events and the subsequent deformation of the structure. Here, the interplay between soil deformation and structural response showcased the interconnected nature of the two factors. The integration of inclined and vertical piles, along with capping beams, illustrated the capacity to mitigate pile displacement through a distributed structural system.

## References

Elgamal, A., Yang, Z., Parra, E., & Ragheb, A. (2003). Modeling of cyclic mobility in saturated cohesionless soils. International Journal of Plasticity, 19(6), 883-905.

Yang, Z., Elgamal, A., & Parra, E. (2003). Computational model for cyclic mobility and associated shear deformation. Journal of Geotechnical and Geoenvironmental Engineering, 129(12), 1119-1127.

Dafalias, Y. F., & Manzari, M. T. (2004). Simple plasticity sand model accounting for fabric change effects. Journal of Engineering mechanics, 130(6), 622-634.

Taiebat, M., & Dafalias, Y. F. (2008). SANISAND: Simple anisotropic sand plasticity model. International Journal for Numerical and Analytical Methods in Geomechanics, 32(8), 915-948.

Yang, M., Taiebat, M., & Dafalias, Y. F. (2022). SANISAND-MSf: a sand plasticity model with memory surface and semifluidised state. Géotechnique, 72(3), 227-246.

Papadimitriou, A. G., & Bouckovalas, G. D. (2002). Plasticity model for sand under small and large cyclic strains: a multiaxial formulation. Soil Dynamics and Earthquake Engineering, 22(3), 191-204.

Beaty, M. H., & Byrne, P. M. (2011). UBCSAND constitutive model version 904aR. Itasca UDM Web Site.

Boulanger, R. W., & Ziotopoulou, K. (2015). PM4Sand (Version 3): A sand plasticity model for earthquake engineering applications. Center for Geotechnical Modeling Report No. UCD/CGM-15/01, Department of Civil and Environmental Engineering, University of California, Davis, Calif.

Cheng, Z., & Detournay, C. (2021). Formulation, validation and application of a practice-oriented two-surface plasticity sand model. Computers and Geotechnics, 132, 103984.

Idriss, I. M., & Boulanger, R. W. (2008). Monograph MNO-12: Soil liquefaction during earthquakes. Earthquake Engineering Research Institute, Oakland, CA.